ESTIMATED DISTRIBUTED NEAR-FIELD SURFACE DISPLACEMENTS USING NASCENT MOBILE LASER SCANNING

by

Xinxiang Zhu

A Dissertation submitted to the Department of Civil and Environmental Engineering,

Cullen College of Engineering

in partial fulfillment of the requirements for the degree of

Doctor of Philosophy

in Geosensing Systems Engineering and Sciences

Chair of Committee: Craig L. Glennie

Committee Member: Benjamin A. Brooks

Committee Member: Preston J. Hartzell

Committee Member: Hyongki Lee

Committee Member: Shuhab D. Khan

University of Houston

May 2022

Acknowledgments

I am grateful to the people who have helped and encouraged me throughout my doctoral research. I would like to thank my advisor Craig, for welcoming me into his research group and giving me generous support over the past five years. He taught me how to become a good student and more importantly a good researcher and engineer for the rest of my life. I have had a great time working with him and look forward to many more years of knocking on his door.

I would also like to acknowledge other committee members. Dr. Benjamin Brooks helped me with the lidar data collection, and his insights on shallow fault mechanics inspired me with the motivation for this work. I would also thank Dr. Preston Hartzell for his endless support and for being so patient with my questions. Thanks also to Dr. Hyongki Lee and Dr. Shuhab Khan who were also the committee members for my Master thesis. Thanks for supporting me all along and for your insightful feedback.

I would like to thank my colleagues at the National Center for Airborne Laser Mapping, Andrea Albright, Cami Barlow, Sven Sorhus, Ning Cao, Ziyue Dang, and my friends, Timothy Kearns, Daniel Rusinek, Linqiang Yang, Hanlin Liu, and many others. They have helped me so much at work and in life. It was difficult for me as a foreign student during the tumultuous times as the coronavirus pandemic and the Texas winter storm. Without the support of my friends, I would not have made it this far and probably would have given up. And I would like to thank them for constantly reminding me how good I am when I lost my confidence and get frustrated in research. They are the best coworkers and will be my best friends for life.

Last but not least, I want to thank my parents for their warm and unconditional support. I feel very fortunate to have their understanding while studying abroad.

The sweet memory at the University of Houston will last forever.

Abstract

Modeling fault dynamics requires dense observations of surface displacements over time. However, it remains challenging to observe distributed fault displacements due to non-linear deformation. Observation of near-field displacements challenges the level of detection limits of modern geosensing measurements because the rate of the displacements can be as small as several mm per year with variations only within several hundreds of meters from a fault trace, i.e. in the near field. To fill this void, we introduce a mobile laser scanning (MLS)-based change detection framework that is capable of detecting distributed fault displacements in the near field with high resolution and accuracy. The approach leverages MLS's redundant point cloud representation of an object's location and models the corresponding point clouds as geometric primitives for change detection. Corresponding point clouds are extracted using PointNet, a deep neural network, and a customized random sample consensus estimator. A combined least squares adjustment is developed for primitive modeling and change detection for both bi- and multi-temporal lidar time series, and the multi-temporal analysis introduces additional temporal constraints for further accuracy improvement. Using data collected after the Mw 6.0 2014 South Napa earthquake, our results reveal centimeter-level horizontal ground deformation, the post-seismic displacement field is detected by tracking displacements of vineyard posts modeled as cylindrical primitives from which patterns of off-fault deformation are identified and show agreement at cm level with collocated alinement array observations. Using MLS data collected in 2015, 2017 and 2018 on a segment of the Hayward fault, bi- and multi-temporal fault creep displacements are detected by leveraging abundant planar primitives in the built environment. The change detection results give time series of distributed fault creep displacement and the detected off-fault displacement profile matches in situ theodolite and creepmeter observations at the subcentimeter level. The proposed framework is shown to be accurate and practical for fault displacement detection in the near field and provides geodetic observations of non-linear displacement patterns at an unprecedented scale, and the results can be used to elucidate more sophisticated models of fault dynamics.

Table of Contents

List of Tables

List of Figures

Chapter 1

Introduction

This dissertation is dedicated to exploring methods of light detection and ranging (lidar) point cloud-based change detection that can be used to measure earthquake-related fault displacements within several hundreds of meters of a fault trace. Given that limited geodetic observations and data processing methods exist that can provide distributed ground displacements recorded in the near field of a fault, we provide a way to monitor fault displacements using nascent mobile laser scanning (MLS) data. As the analysis of shallow fault mechanisms remains elusive largely due to the lack of consistent geodetic data close to an active fault [5, 6], we describe a framework of change detection using geometric model-based methods to quantify near-field nonlinear displacements.

The earliest earthquake catalog can be traced back to the Chinese earthquake catalog made in 1177 B.C. [22]. The earliest known earthquakes in the Americas was in Mexico in the late 14th century and in Peru in 1471. At the early stage of earthquake monitoring, many cultures looked for mythical ways to explain historical earthquakes. For example, in China, the Earth shakes when an imbalance of yin and yang occurs; in Japan, the Earth trembles because a great underground catfish or namazu flips; in India, the Earth is believed to be held up by four elephants that stand on the back of a turtle, and the turtle is balanced on top of a cobra. When any of these animals move, the Earth trembles and shakes. Now we know an earthquake is what happens when two blocks of the earth suddenly slip past each other. The surface where they slip is called the fault or fault plane[23]. Because of this 'unpredictable' sudden slip, an earthquake can potentially cause catastrophic damage to human and man-made structures. According to a report updated in June 2017 by FEMA, the annual building stock losses caused by earthquake hazards in the U.S. are estimated to be $6.1 billion. On the other hand, many of the Earth's natural resources including energy, minerals, and soil are concentrated near past or present plate boundaries where seismic faults are commonly generated. The utilization of these readily available resources has sustained human civilizations, both now and in the past. In order to coexist with the fault, mitigate seismic hazards and take advantage of the resources brought by the faulting process, we need to study earthquake faults.

Earthquakes shape the earth with unique and diagnostic landforms caused by the faulting process. To study this process, one of the initial observations one can acquire is measurements of fault-related land deformation. Early records of earthquakes are more descriptive but less quantitative in terms of ground deformation. To better understand the mechanism behind earthquakes, starting in the late 1800s, displacements of large earthquakes were documented by geodetic observations to provide quantitative records of fault-related land deformation. In 1892, a triangulation survey was interrupted by the Tapanuli earthquake which led to the first geodetic record of an earthquake through a triangulation network. The right-lateral slip was observed as dislocation [24]. Ever since then, triangulation and leveling surveys have been used as geodetic measurements to record fault-related ground deformation.

For around 100 years, before the implementation of Electronic Distance Meters (EDM), Very Long Baseline Interferometry (VLBI) and Global Positioning Systems (GPS), methods of geodetic observation did not change much. However, with the accumulation of repeated geodetic observations, interpretations and modeling of the observed fault displacements thrived. The concept of elastic rebound was proposed by Gilbert [25] and validated by Reid [2] with geodetic observations. The theory suggested that the outbreak of an earthquake is like a sudden break or cut of a stretched rubber band where the crust of the earth gradually stores elastic stress that is suddenly released during an earthquake [2]. Reid also found that total relative displacements of distant points on the opposite sides of the fault represented only half the average slip during the 1906 San Francisco earthquake.

This finding laid the foundation for long-term earthquake forecasting by comparing the co-seismic displacements with the measured rate of fault creep accumulation between major earthquakes [26].

With the civilian applications of the Global Positioning System (GPS), geodetic observations using GPS have been used to monitor fault displacements. For example, continuous GPS networks were used to record ground displacements over time for the 1992 Mw 7.3 Landers, California earthquake to monitor co- and post-seismic displacements [27], nation-wide GPS stations were used to record co-seismic displacement for the 1994 M_{JMA} 8.1 Hokkaido-Toho-Oki, Japan earthquake [28], and co- and post-seismic fault slip detected by GPS were used for modeling and studying the slip depth and fault geometry for the 1999 Mw 7.5 Izmit Turkey earthquake [29]. Permanent Global Navigation Satellite System (GNSS) stations are continuously monitoring aseismic fault creep: applications include, but are not limited to, the study of the Hayward fault, California [30] and the studies at the Nankai and Japan-west Kurile subduction zones [31].

In the past three decades, the temporal coverage of geodetic observations have been extended to the entire earthquake cycle such that additional post-seismic and inter-seismic faulting measurements can be analyzed. Spatial coverage and detection resolution have improved through the implementation of high-definition surveying techniques like InSAR, satellite photography, and lidar. Figure 1.1 shows the faulting processes that have been monitored by geodetic measurements. The application of high-definition surveying makes it possible to analyze ground displacement at an unprecedented spatial resolution and results in distributed ground displacements, rather than a single measurement per site (like GNSS). With distributed displacements, it is possible to examine nonlinear deformation patterns especially near the fault trace where the displacement offset is smaller than the fault slip at seismogenic depth. This slip deficit implies a potential systematic underestimation of the earthquake hazard using geodetic measurements and historical geological

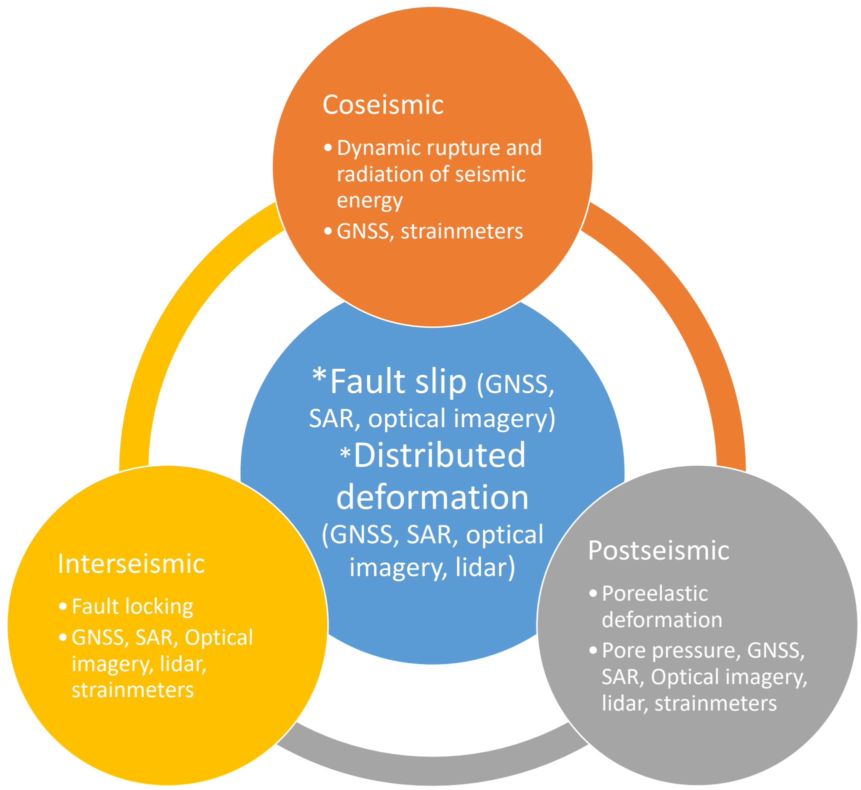

Figure 1.1 How fault deformation observation is related to co-seismic, post-seismic, and inter-seismic faulting processes. Figure adapted from Nevitt [1].

slip records [32, 33]; however, the cause of this slip deficit remains unknown. To study the slip deficit and understand how it relates to nonlinear ground deformation, we need dense near-field observations of surface displacements. This requirement for high fidelity displacement patterns necessitates new types of geodetic observations.

Inference of fault slip reduction goes back at least to the study of the 1906 Mw 7.9 San Francisco, California earthquake. As shown in Figure 1.2, the hypothesis suggests that a part of the displacement is accomplished by shearing distortion and the offset at the fault-plane will be less than that of the underlying rock. Suppose a straight line AOC in the rock has been broken at the fault and displaced onto $A'O'$ and $D'C'$, if the alluvium were brittle and with little plasticity, it might be broken and displaced in the same way, but if the alluvium were to be some extent composed of clay, a part of the displacement

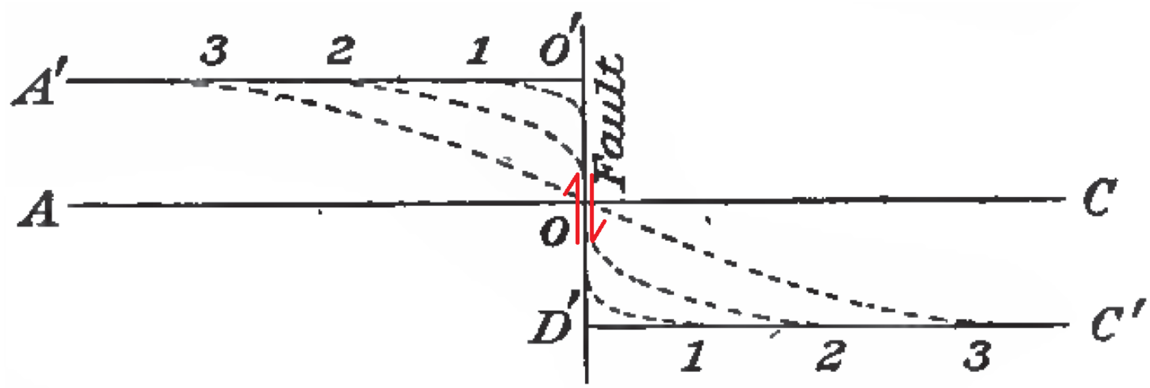

Figure 1.2 Hypothesis on shearing movements in the fault-zone. Figure from [2], page 38.

would be accomplished by shearing distortion, and the offset at the fault-plane would be less than that of the underlying rock [2]. The closer to the rock depth, the more similar the displacement pattern would behave. Dashed line 1 reflects the displacement pattern closer to the rock at depth, and dashed line 3 reflects the displacement pattern further to the rock at shallow. This hypothesis has been confirmed by geodetic observations such as the study by Ayoub et al. [34] where satellite photography was used to quantify co-seismic displacement on several profiles during the 1992 Mw 7.3 Landers, California earthquake. Although the measurements might be affected by variability and resolution of the air photos, the study indicated signs of slip reduction and reported several non-linear displacement profiles (Figure 1.3) across the fault, similar to the pattern shown in Figure 1.2.

Rather than relying on a bulk characterization of on- versus off-fault deformation, new studies focus on the mechanical details to try and explain the slip decrease towards the earth surface [4–6, 35]. The associated observations of co-seismic displacement have been extended to observations of both co- and post-seismic displacement fields. Fault displacements acquired from successive earthquake cycles help researchers inspect how the co-seismic slip deficit is accommodated throughout the earthquake cycle. Various conditions, including plastic deformation [4, 35], buried fault tip [5, 6] and pore-elastic deformation [5], contribute to shallow slip modeling and the distinctive ground signatures that can

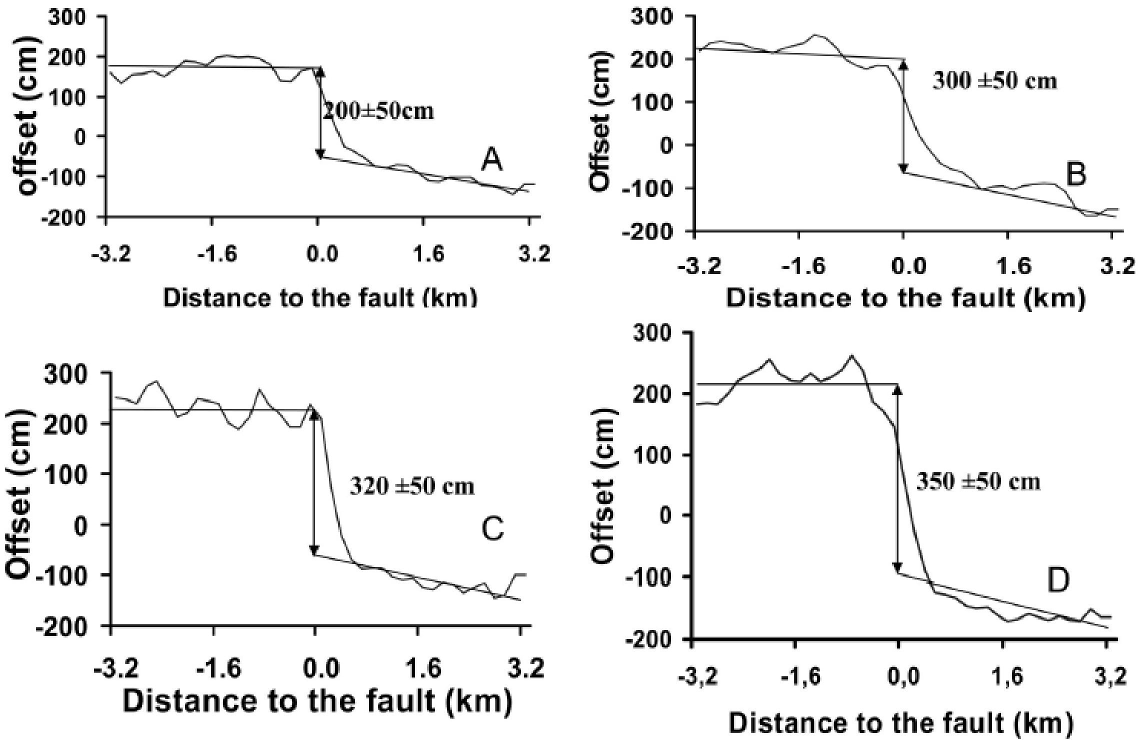

Figure 1.3 Strike-parallel surface displacements measured from satellite photography (SPOT images) during the 1992 Mw 7.3 Landers, California earthquake. Figure from Michel and Avouac [3].

be used to infer causality of different conditions is only observable within several hundreds of meters of the fault trace, i.e. in the near field of a fault.

Figure 1.4 (a) shows a schematic plot of an off-fault near-field displacement profile where the X-axis represents the perpendicular distance to the local fault trace and the Y-axis represents the offset of the ground displacements parallel to the fault. The curvature in the middle of the profile shows the ground response for various observed slip deficit cases. As the tangent of the relationship between the locking depth and ground displacement [36], the curvature of the surface displacement pattern varies the most at the fault trace, whereas the far-field displacement observations contribute more to the estimation of the slip rate while the near field displacement observations contributes more to the estimation of the locking depth [37]. Based on elastic dislocation theory [38], the estimation of

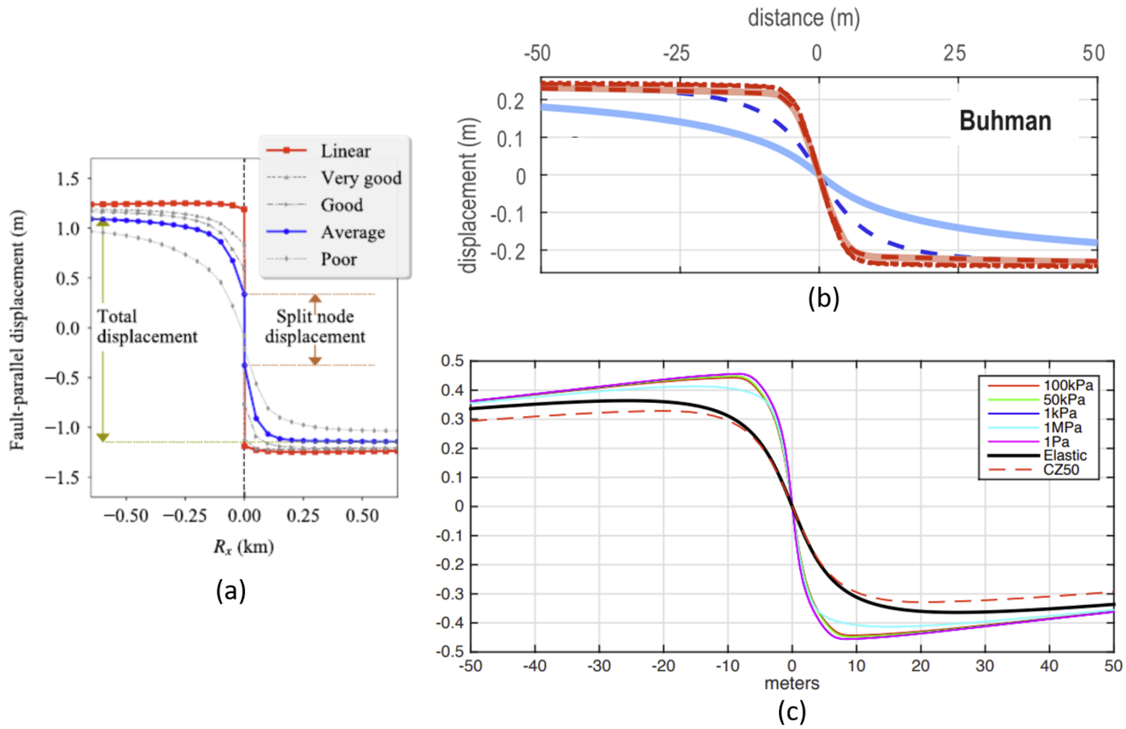

Figure 1.4 Examples of simulated off-fault near-field displacement profiles [4–6].

the fault locking depth is highly dependent upon the curvature of the ground displacement distribution. To study the form of this curvature, ground displacements are simulated given different mechanical models of a fault. Figure 1.4 shows three examples of simulations where: (a) Roten et al. [4] explores the ground response of dynamic rupture with various fault zone plasticity and (b, c) Nevitt et al. [5], Brooks et al. [6] do similar simulations with additional pre-existing buried fault tips. Nevitt et al. [5] modeled surface displacement with various mechanical properties for a fault buried 5 m below Earth's surface; the elastic model response is shown in blue and elastoplastic models in red (Figure 1.4 (b)). Brooks et al. [6] simulated surface displacement profiles from elastoplastic models with various cohesion. The simulation shows the displacement of a fault upper edge buried 5 m below Earth's surface with a prescribed uniform slip of 1 m (Figure 1.4 (c)).

Although these are still active studies relating these surface expressions to real ground motion, these simulations infer the nonlinear ground displacement patterns in the near field as a result of slip reduction and more importantly outline the potential scale and variation of nonlinear displacement pattern expected in consistent and distributed geodetic observations which have not been possible to date. One of the fundamental objectives of this dissertation is to provide measurements for these nonlinear ground displacements in the near field as a reference for future mechanical models studying the depth of the buried fault plane.

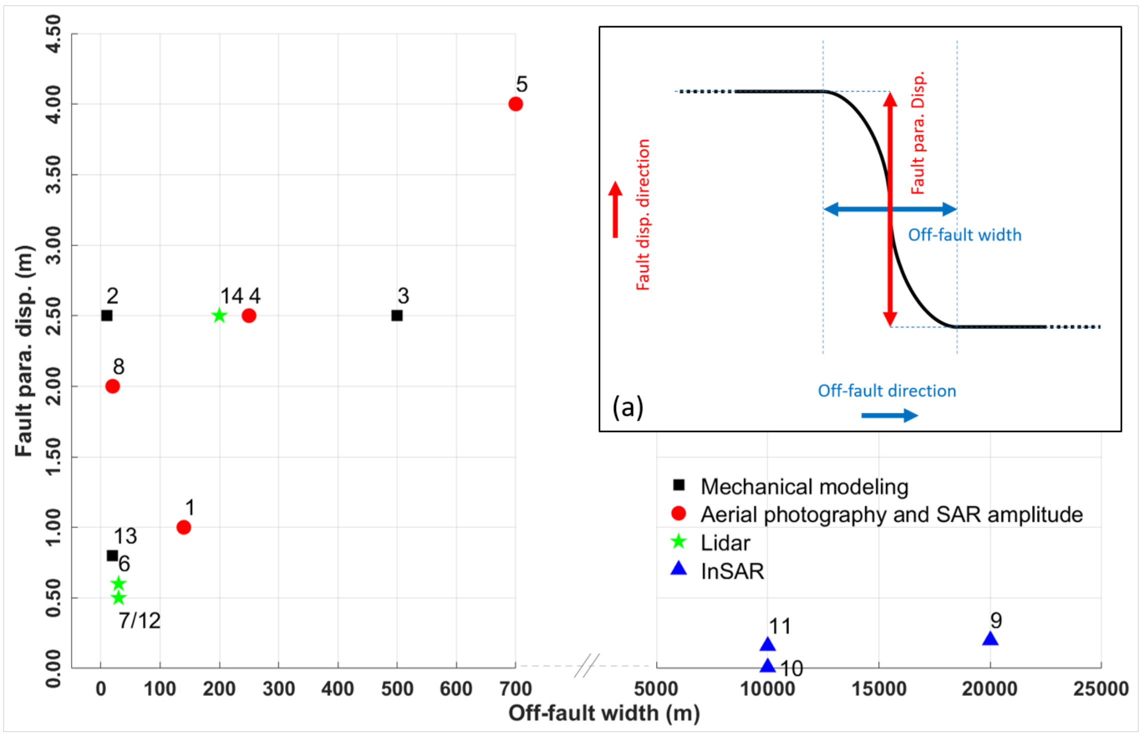

(b)

Figure 1.5 Overview of nonlinear ground displacements measured from geodetic observations and simulated by mechanical modeling. (a) Schematic plot of an off-fault displacement profile. (b) Overview of previous studied displacement profiles.

In order to choose suitable geodetic means to observe displacements in the near field, 14 previous studies were reviewed that have documented ground displacements in the near field and resolved displacement profiles like those shown in Figure 1.5. (a) shows a schematic plot of an off-fault displacement profile illustrating how fault parallel displacements vary with off-fault distances (perpendicular distances from the local fault trace). The portion of nonlinear ground displacements is outlined by the off-fault width (blue arrow)

Table 1.1 Overview of previous studies with off-fault displacement profiles. Index in the table corresponds to the numbers in Figure 1.5.

Idx	Method description	Reference
1	Satellite photography measurements on the co-seismic displacement of the 1992 Mw 7.3 Landers, California earthquake.	Michel and Avouac [3]
2	Simulated ground displacements from a linear elastic modeling on M 7.2-7.4 earthquakes	Roten et al. [4]
3	Simulated ground displacements from a nonlinear elastoplastic modeling on M 7.2-7.4 earthquakes	Roten et al. [4]
4	Satellite photography measurements on the co-seismic displacement of the 1992 Mw 7.3 Landers, California earthquake. Change detected using COSI-Corr program.	Milliner et al. [39]
5	Satellite photography measurements on the co-seismic displacement of the 1992 Mw 7.3 Landers, California earthquake. Change detected using COSI-Corr program.	Ayoub et al. [34]
6	MLS measurements on the co-seismic displacement of the 2014 Mw 6.0 South Napa, California earthquake.	Nevitt et al. [5]
7	MLS measurements on the post-seismic displacement of the 2014 Mw 6.0 South Napa, California earthquake.	Nevitt et al. [5]
8	SAR measurements on the co-seismic displacement of the 2016 Mw 7.0 Kumamoto, Japan earthquake	He et al. [40]
9	InSAR measurements on the co-seismic and early post-seismic displacement of the 1999 Mw 7.6 Izmit, Turkey earthquake	Cakir et al. [41]
10	InSAR measurements on the aseismic Hayward, California fault creep. Creep rate estimated by observations from 1992 to 1997.	Bürgmann et al. [30]
11	SAR amplitude measurements on the co-seismic displacement of the 1992 Mw 7.3 Landers, California earthquake.	Michel et al. [42]
12	MLS measurements on the post-seismic displacement of the 2014 Mw 6.0 South Napa, California earthquake.	Brooks et al. [6]
13	Simulated ground displacements from a elastic and elastoplastic modeling on the 2014 Mw 6.0 South Napa, California earthquake.	Brooks et al. [6]
14	ALS measurements on the co-seismic displacement of the 2016 Mw 7.0 Kumamoto, Japan earthquake	Scott et al. [43]

and the maximum fault parallel displacement (red arrow) in the near field. (b) shows an overview of the scale of nonlinear ground displacements documented by previously studied fault displacement profiles presented in Table 1.1. Each dot represents the off-fault width and the maximum fault parallel displacements estimated for the nonlinear portion of the displacement profile. Figure 1.5 (b) and Table 1.1 show the width of nonlinear ground displacements ranging from a few meters to kilometers and the displacement offsets ranging from centimeters to meters. In terms of the displacement scale (Y-axis), meter-level ground displacements are found in records of co-seismic displacements, cm-level displacements are detected in post-seismic displacements and mm-level displacements rates (annual rate) are detected aseismic/inter-seismic. Regarding the width of the nonlinear deformation zone (X-axis), the nonlinear deformation is in general recorded within 500 m of the fault trace except for the records from Interferometric Synthetic Aperture Radar (InSAR). InSAR provides unique far field records of ground displacements where mm to cm level displacements are recorded but only cover the area over 1 km from the fault trace. This lack of near field detection is because of phase decorrelation of the interferogram [41, 44, 45]. As shown in the displacement profiles, for example in Figure 1.2, 1.3 and 1.5, ground motions in the near field are characterized by nonlinear deformation with inflection areas accommodating most of the transitions of displacements. Ruptures or ground dislocations are commonly reported in the transition area recorded by field surveys. Interferograms tend to decorrelate with spatial change and are vulnerable to large displacements and complex textures found within the ruptured area which makes InSAR change detection only reliable in the far field.

Given the complex displacements found in the near field, Figure 1.6 compares new geodetic techniques with their precursors in terms of their spatial coverage and resolution for displacement observations. Given the scale of the off-fault deformation recorded from previous studies, ideal methods should as least have spatial coverage that matches the width of the nonlinear displacement, have a spatial resolution that provides enough

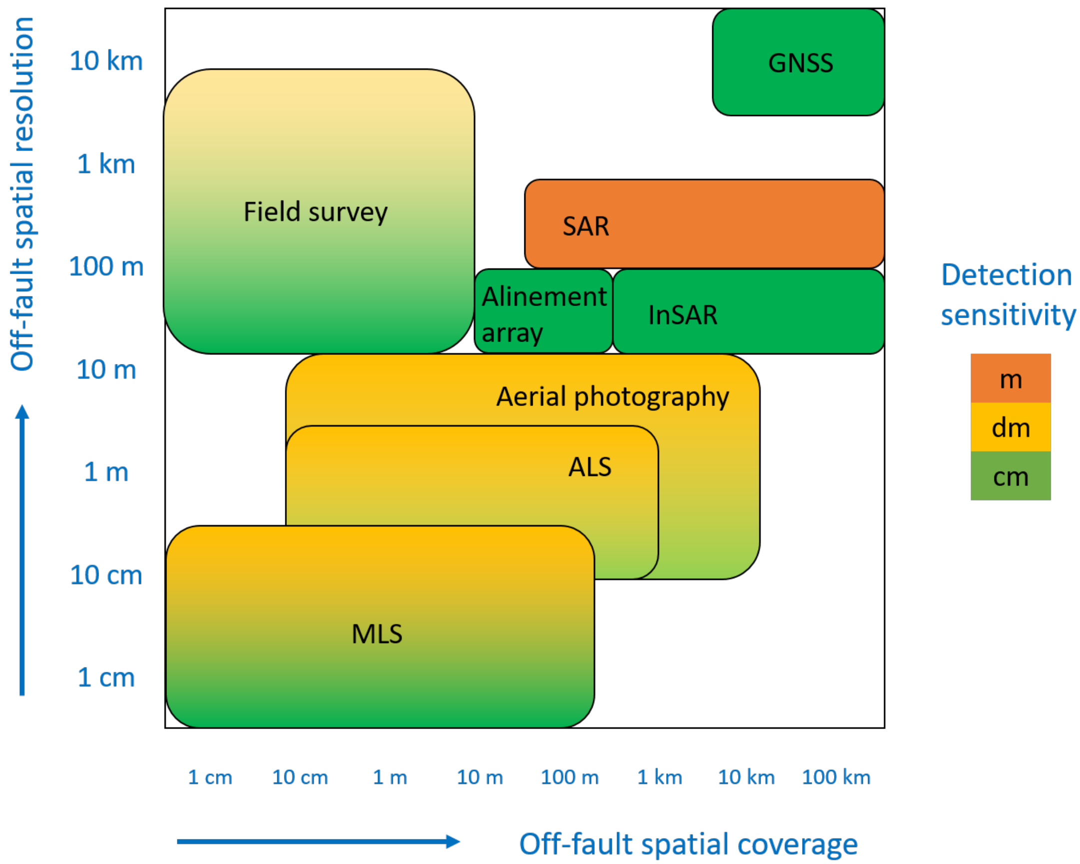

Figure 1.6 Overview of spatial coverage and resolution of geodetic observations. Figure adapted from Borsa and Minster [7] and Zhang [8].

samples to delineate nonlinear deformation and have a detection sensitivity that is at least no larger than the recorded displacement documented in previous geodetic records. As traditional methods for measuring fault displacements, field surveys, alinement array measurements, and GNSS measurements are sensitive to displacements at the cm-level but have limited spatial coverage and resolution. Observations acquired from these methods can be used for validation or as constraints for other methods, but cannot be used as stand-alone measurements to quantify distributed displacements given their limited spatial coverage. SAR and satellite photography have been used to monitor co-seismic displacements with meter-level resolution by applying image correlation-based change detection strategies, for example [3, 34, 39, 42, 44]. These methods deliver partial displacement fields, as only the horizontal displacements can be detected using pixel correlation-based detection. Change detection using these methods is in general unable to provide better than decimeter level accuracy, even with high-resolution images [12]. With improved detection sensitivity, airborne laser scanning (ALS) can be used to monitor co-seismic displacement at the sub-meter scale [43, 46–48]. However, mobile laser scanning (MLS) is the only method that has been used to detect post-seismic displacement and aseismic/inter-seismic displacement with cm-level detection sensitivity and meters scale spatial resolution [5, 6, 49, 50].

Compared with other geodetic methods, MLS has better detection sensitivity, spatial coverage and sampling resolution, making it an ideal tool to detect displacements in the near field. However, there are limited change detection strategies available for MLS data processing that leverage its unique observation geometry, high-accuracy and resolution. Processing strategies are needed that overcome the complex and irregular representation of the object space afforded by an MLS point cloud. The increased complexity makes the state-of-the-art change detection strategies less effective given that it is hard to identify unique correspondence between objects in the point clouds to provide stable geometry for estimating change.

1.1 Contributions

As limited geodetic observations and associated change detection strategies are available, new MLS change detection strategies are proposed and developed that apply to estimating fault displacement in the near field with high accuracy and high spatial resolution. The primary contribution of this dissertation is providing high-fidelity nonlinear displacement fields detected in the near field which have not been possible to date by other geodetic measurements. Compared with previous change detection algorithms, the proposed method is capable of revealing displacements with better than centimeter-level accuracy and enabling applications for both post-seismic and aseismic near-field fault displacement detection.

First, we propose an automated change detection strategy using geometric primitives generated using a deep neural network, random sample consensus and a least squares adjustment. Using mobile laser scanning point clouds of vineyards acquired after the magnitude 6.0 2014 South Napa earthquake, our results reveal centimeter-level horizontal ground deformation over three kilometers along the West Napa Fault. A fault trace is detected from rows of vineyards modeled as planar primitives from the accumulated co-seismic response, and the post-seismic surface displacement field is revealed by tracking displacements of vineyard posts modeled as cylindrical primitives. We summarize distributions of deformation versus off-fault distances and find evidence of off-fault deformation from the estimated displacements. The proposed framework using geometric primitives is shown to be accurate and practical for detection of near-field off-fault deformation.

Second, an improved change detection framework is adapted from the initial model that is capable of detecting distributed fields of centimeter-level displacements located in the near field within approximately 150 m of the fault trace. The methodology leverages the use of man-made features in the built environment as geodetic markers that can be temporally tracked. The proposed framework consists of a RANSAC-based corresponding plane detector and a combined least squares displacement estimator. Using repeat mobile laser scanning data collected in 2015 and 2017 on one segment of the Hayward fault, near-field fault creep displacement and non-linear creep deformation are estimated. The detection results reveal 2.5 ± 1.5 cm accumulated fault parallel creep displacement in the far-field. The laser scanning estimates of displacement match collocated alinement array observations at the 4 mm level in the near field. The proposed change detection framework is shown to be accurate and practical for fault creep displacement detection in the near field and the detected non-linear creep displacement patterns can be used to elucidate more sophisticated models of fault creep dynamics.

Third, a lidar time series change detection framework is built from the existing bi-temporal detection framework. Leveraging persistent planar surfaces in the lidar point clouds, the new framework resolves ground displacement fields by tracking augmented planar primitives. Compared to bi-temporal change detection, the proposed framework estimates time and space consistent multi-temporal changes simultaneously taking advantage of additional temporal and geometric constraints. With a synthetic test and a case study validation, the proposed framework shows robust change detection on the lidar time series. Results reveal $15 \pm 5.2\,mm$, $7.7 \pm 8.7\,mm$ and $21.1 \pm 9.7\,mm$ fault parallel displacements detected at 44 m from the Hayward fault trace detected in periods of 2015-2017, 2017-2018 and 2015-2018 respectively, and validation with a collocated alinement array station shows sub-centimeter agreement.

1.2 Dissertation outline

In Chapter 2, we provide an overview of fault displacement estimation using various geodetic methods shown in Figure 1.6. This chapter reviews applications of fault displacement detection and analyzes the pros and cons of implementing certain geodetic methods in the near field.

Chapter 3 provides an overview of lidar point clouds-based change detection algorithms with a focus on exploring the suitability of the methods for estimating near-field fault displacement.

Chapter 4 is the first peer-reviewed publication on Automated Near-field Deformation Detection from Mobile Laser Scanning for the 2014 Mw 6.0 South Napa Earthquake. This paper lays the foundation for primitive-based change detection as we use planar and cylindrical primitives to detect co- and post-seismic displacement for the 2014 Mw 6.0 South Napa Earthquake. The paper concludes that geometric primitive-based change detection is a practical and accurate way to reveal fault displacements in the near field.

Chapter 5 is the second peer-reviewed publication on Monitoring Aseismic Fault Creeps using Combined Corresponding Planar Primitives Generated from Mobile Laser Scanning. This paper demonstrates an improved change detection method adapted from the proposed geometric primitive-based change detection. Corresponding planar primitives are detected and augmented for change detection that comes with improved detection accuracy and sensitivity. The method is shown to be practical to capture centimeter-level fault creep displacement in the near field with mm-level accuracy validated by alinement array measurements.

Chapter 6 is the third peer-reviewed publication on multi-temporal change detection for a lidar time series. This paper described an extension of our bi-temporal change detection framework and directly works on processing lidar time series collected in multiple epochs. The method leverages additional constraints on the temporally spaced corresponding planar primitives and results in time and space consistent multi-temporal change detection results.

Chapter 7 summarizes the research findings and outlines several recommendations for future research.

Chapter 2

Methods of detecting fault displacement in the near field

As one of the major applications of remotely-sensed data, change detection is the process of identifying differences in the state of an object or phenomenon by observing it at different times [51]. In the case of fault displacement detection, the 'state' is ground motions in the faulting area, and the 'time' depends on the observed earthquake cycle. The term 'near field' posts an extra restriction for the survey as the detection is conducted near the fault trace where a fault intersects the ground surface. According to these definitions, results of near-field fault displacement are measurements of space and time, and ideal change detection should have the following characteristics: (1) quantify changes at the spatial dimension of interest, ideally in 3D, (2) resolve changes at the spatial resolution according to the scale of the seismic event, (3) quantify changes over the temporal span of the earthquake cycle, and (4) capable of doing (1), (2) and (3) in the near field. Each characteristic serves as a guideline for selecting or comparing geodetic methods for change detection in the near field.

According to elastic-rebound theory [2], the entire seismic 'cycle' can be divided into three periods. A simplified representation of the dynamics of fault slip can be found in Figure 2.1. A seismic cycle is arranged according to the stages of the frictional forces within the earth crust that counterbalance the strain accumulated in the faulting area. Depending on the dynamics of the faulting process, inter-seismic slip refers to steady state where elastic strain accumulates slowly and simultaneously with friction within the rocks that locks the fault slip, co-seismic slip refers to the sudden rupture as the locking fails and triggers an earthquake and post-seismic slip refers to fault slip transitioning back to the static inter-seismic stage. The term 'slip' refers to fault deformation at depth and is quantified by strain (as relative internal change) whereas the term 'displacement' is reserved for representing the ground surface deformation induced by fault slip at depth and is quantified by the initial and end locations of the ground surface. Therefore, displacements should be vectors that represent the differences between the final and initial ground surface locations in a three-dimensional Euclidean space. With the criteria for choosing proper change detection methods and the metrics for quantifying fault displacement, this chapter reviews common change detection methods and their applications for estimating fault displacement.

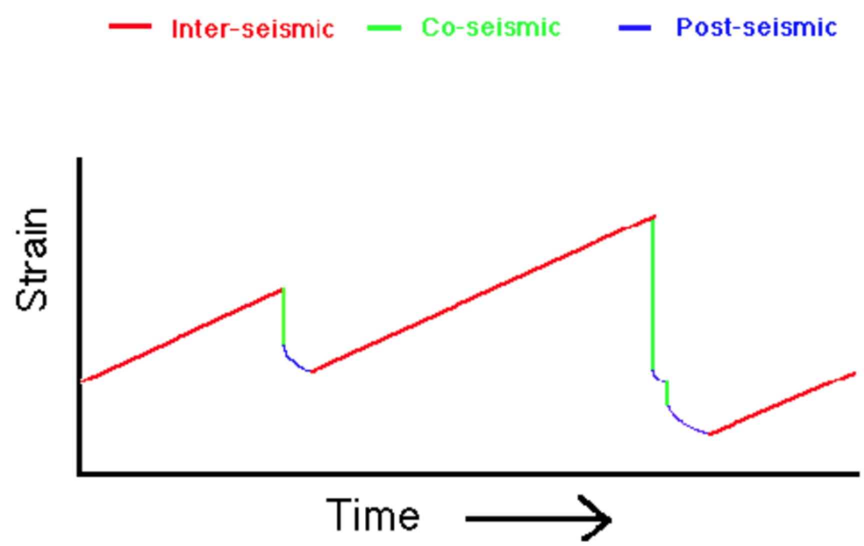

Figure 2.1 Earthquake cycles shown as a history of strain accumulation and release along a single fault patch. Figure from DeMets [9].

2.1 Sparse geodetic observations of fault displacement

Sparse geodetic observations refer to geodetic measurements that have limited spatial coverage. Common observations include measurements acquired by field reconnaissance, GNSS, alinement arrays, creepmeters (strainmeters, tiltmeters) that directly record the strain underground, Very Long Baseline Interferometry (VLBI) that record the earth deformation at the continental scale and the Rupture and Fault Zone Observatory (RuFZO) [52]. RuFZO is infrastructure under construction for monitoring fault dynamics in the near field. The infrastructure consists of linear arrays of seismic sensors every 20-30 km to provide unprecedented in situ recording of dynamics fields within rupture zones. Field surveys, GNSS, and alinement arrays are discussed in more detail below because they offer direct measurements of displacement that are more relevant to the near field and can be used as validations for other geodetic observations.

2.1.1 Field survey

As the most common observations, field reconnaissance is routinely conducted after major earthquakes. Investigations usually focus on recording infrastructure damage due to ground surface rupture and mapping of surface fault expression and the affected fault traces. For instance, the Geotechnical Extreme Events Reconnaissance Association (GEER) reported field reconnaissance for the 2014 Mw 6.0 West Napa Earthquake by documenting surface displacements via (1) detailed mapping of surface fault rupture on the affected fault trace, (2) recording infrastructure damage due to ground surface rupture, and (3) measuring ground deformation in the very near-fault region [53]. According to GEER, features are tape measured for deformation; most ruptures were located by driving roads across the area and looking for disrupted or offset cultural features. Photos are taken in addition to the tape measurements and serve as important reference data for interpretation. Shown in Figure 2.2, (a) and (b) were taken from the field survey for the 2014 Mw. 6.0 South Napa earthquake showing the surface expression of faulting. (c) and (d) were taken during the MLS survey of the Napa fault [6] illustrating ground ruptures reported by the GEER field reconnaissance of the Napa earthquake [53].

Field reconnaissance provides accurate local displacement measurements which serve as a reliable reference for other geodetic observations. The displacement measurements are usually accompanied with additional descriptive information which helps determine the cause and evolution of deformation. Despite the benefits, a field survey is labor-intensive and time-consuming which prevents the method being applied to broader areas. An earthquake and its induced geo-hazards may limit the access to enigmatic zones of deformation

Figure 2.2 Sample photos from a field survey.

over the surface faulting [54, 55], and important displacement signatures could be missed if the displacement is not associated with significant cultural feature damage. In situ surveys rely on road networks and telecommunication systems that could be damaged during the earthquake. Furthermore, field surveys normally measure the apparent ground deformation which needs to be post processed (e.g. projecting apparent ground displacement along and across the fault trace) to estimate fault-related ground displacements. In summary, field reconnaissance provides detailed but inconsistent local measurements of apparent fault displacement which serve as a good reference on site. However, the measurements are not generalized over the ruptured zone and the method cannot be used to estimate distributed ground deformation.

2.1.2 GNSS

GNSS is commonly used for far-field fault displacement monitoring. The method provides point measurements of surface displacement which are consistent in time but sparse in space. The spatial resolution depends on the density of the receiver network. The method can be used to reveal displacement fields at the continental scale (e.g. Bettinelli et al. [56], Kreemer et al. [57], Prawirodirdjo and Bock [58]) but suffers from limited spatial resolution at the sub-continental scale. As a result, the method has limited capability for detecting near-field fault displacement [19].

Despite the sparse observation network, GNSS provides a continuous and persistent time series of ground displacement which is ideal for monitoring the earthquake cycle over time. The constant temporal resolution of GNSS data enables a regression of displacement rate at a few mm level over years of GNSS observations (e.g. [59]). GNSS provides sparse but reliable estimates of fault displacement over its observation network. The stable GNSS observations in the far-field are an ideal absolute reference for the relative displacements detected by InSAR, therefore, they are commonly combined (e.g. Scott et al. [46], Lienkaemper et al. [59], Simons et al. [60]).

2.1.3 Alinement arrays

Alinement arrays are another method of measuring fault displacement. Measurements are collected from a theodolite survey at alinement stations located along the fault trace. Figure 2.3 shows a typical setup of an alinement array station: every station consists of three permanent survey monuments shown as IS, ES and OS. The IS-ES connection spans the fault trace perpendicularly where the angular change of θ is measured by repeated theodolite surveys such that dextral displacement of ES relative to IS and OS can be captured following the formula

$$u = (IS - ES)\tan(\theta_1 - \theta_2). \tag{2.1}$$

The angular accuracy of the theodolite measurements are up to ±0.5 arcseconds which is equivalent to 0.5 mm assuming a 100 m IS-ES baseline. Taking in to account total instrumental and target setup errors, the method can confidently detect any movement greater than 1-2 mm between successive surveys [10]. Compared with GNSS, alinement arrays can reveal fault dextral displacement at a similar or better significance level (at mm-level). The temporal resolution of alinement array observations depends on the frequency of the theodolite surveys.

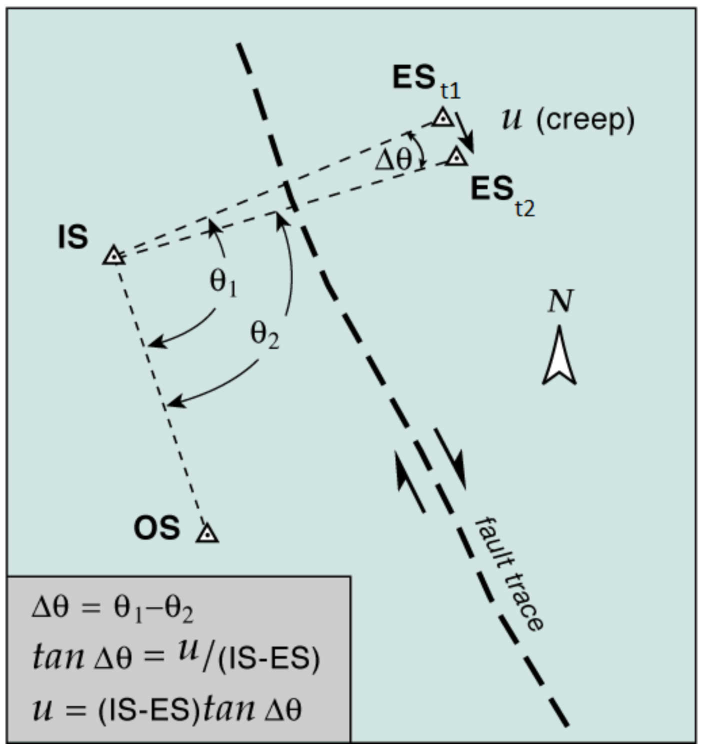

Figure 2.3 Standard alinement array setup. Figure from Galehouse et al. [10].

Given the mm-level accuracy, alinement arrays can be used to monitor subtle fault parallel displacements and changes of displacement during post- and inter-seismic ground deformation. For example, alinement arrays on the San Francisco Bay Region Faults, California (Figure 2.4) successfully revealed the post-seismic fault displacement associated

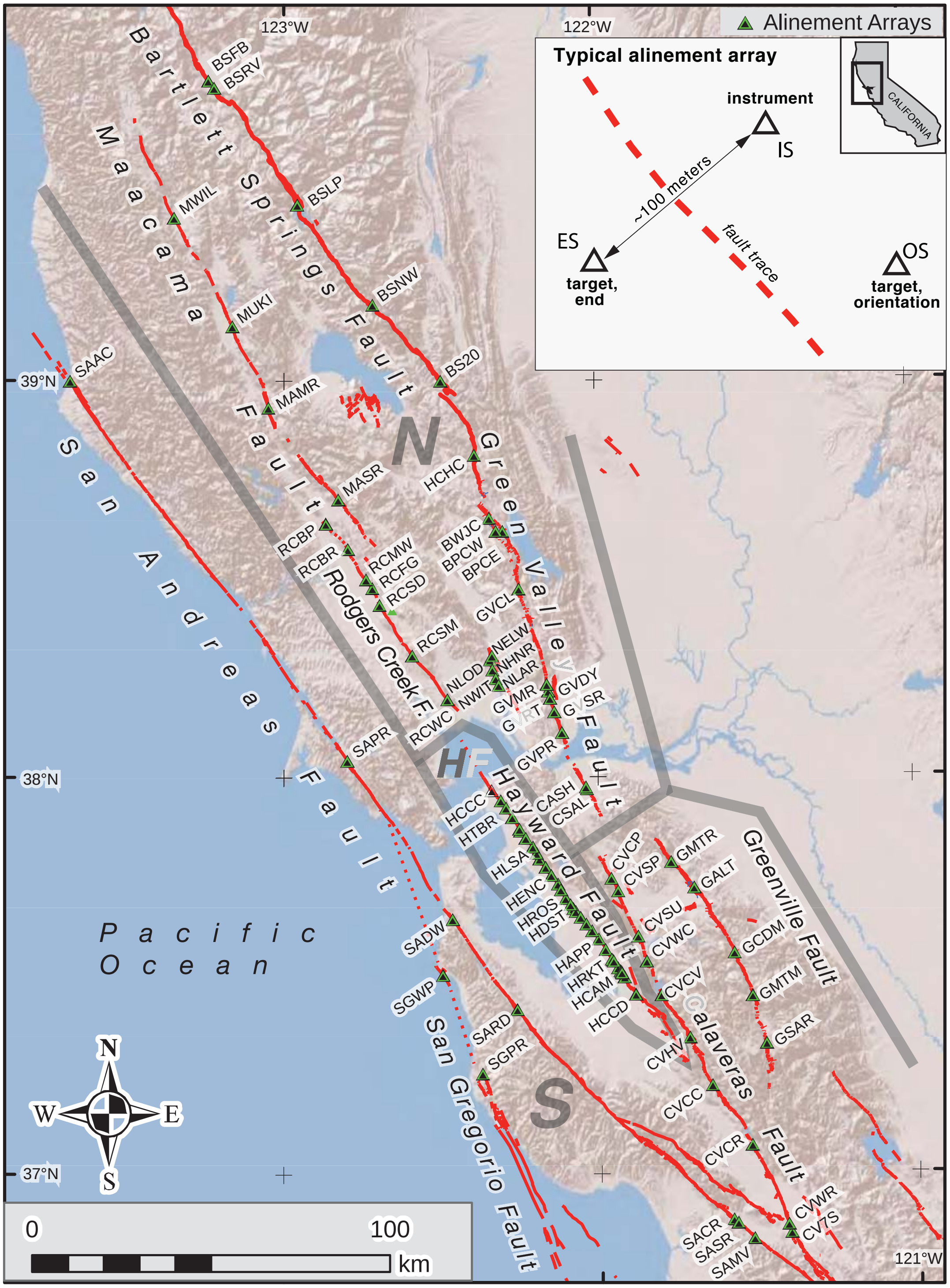

Figure 2.4 Locations of alinement arrays in the San Francisco Bay region. Alinement array stations are shown as triangles and active faults are shown as red lines. Figure from McFarland et al. [11].

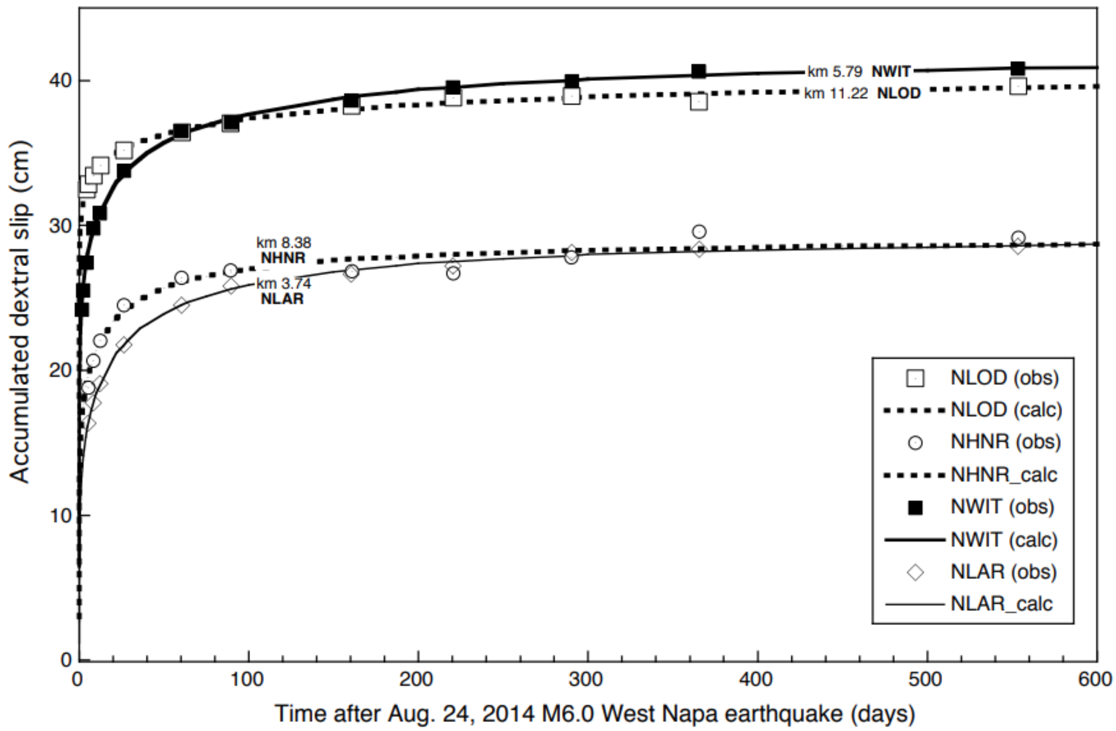

Figure 2.5 Alinement array observations across the West Napa Fault rupture associated with the 2014 Mw 6.0 South Napa earthquake. Figure from McFarland et al. [11].

with the 2014 Mw 6.0 South Napa earthquake as shown in Figure 2.5 [59, 61]. Details of this event are also analyzed in Chapter 4 where the post-seismic displacements observed at station NHNR are used to validate the change detection results. Observations from alinement array stations HCAM, HPIN, HPMD and HSGR (Figure 2.4 and 5.1) are used to validate the results of change detection for the inter-seismic ground displacement for a segment of the Hayward fault (Chapter 5 and 6).

In summary, sparse geodetic measurements from field surveys, GNSS and alinement arrays have limited spatial coverage, and their temporal resolution varies based on observation type. The sparse observations alone are inadequate for revealing patterns of deformation nor can they estimate the off-fault deformation, but the observations can be used to validate distributed fault deformation estimates in the near field.

2.2 High-definition surveying of fault displacement

High-definition surveying of fault displacements refers to the application of photogrammetry and remote sensing techniques for fault dynamics detection. The surveys result in 2D or 3D digital representations of topography. Common high-definition surveying methods that have been used to detect fault displacement include optical imagery, synthetic aperture radar (SAR), Interferometric Synthetic Aperture Radar (InSAR) and light detection and ranging (lidar). When compared with the sparse measurements in the previous section, these techniques for estimating change have improved spatial resolution which allows spatial variation of fault displacement to be captured.

2.2.1 Optical imagery

Optical imagery is a remote sensing tool that can be applied to detect fault displacement. Change detection using optical imagery detects displacement or change of content associated with spectral variations. Fault displacement detection is a subcategory of the prior case as the detection is focused on quantifying deformation of the ground from aerial images.

Almost all imagery-based methods use cross-correlation to detect displacements. In signal processing, cross-correlation is the measure of similarity of two series as a function of the displacement of one relative to the other [62]. Cross-correlation can be used to detect displacement as optimal similarity is achieved when temporally spaced signals correlate with themselves in space. Standard 2D imagery cross-correlation takes the form

$$r_{ij} = \frac{\sum_m \sum_n [f(m+i,n+j) - \overline{f}][g(m,n) - \overline{g}]}{\sqrt{\sum_m \sum_n [f(m,n) - \overline{f}]^2 \sum_m \sum_n [g(m,n) - \overline{g}]^2}}, \tag{2.2}$$

where $f(m,n)$ and $g(m,n)$ are the pixel values at point (m,n) of the reference and secondary image collected pre- and post deformation, and $\overline{f}$ and $\overline{g}$ are the mean values of all the queried pixels of f and g respectively. The displacement (dx,dy) is detected as the indexes of the maximum cross-correlation r, and the solution is normally computed using the fast Fourier transformation for speed [62, 63].

Variants of the cross-correlation method can be described as: (1) replacing the estimate of rigid translation (i, j) with non-linear deformation parameters [64], (2) estimating translation parameters at the sub-pixel scale [65, 66], (3) applying the correlation on multi- or hyperspectral images, and (4) using different strategies [67] to solve the optimization equation

$$(dx, dy) = \arg\max_{i,j} r. \tag{2.3}$$

Applications of optical imagery can be found in the detection of co-seismic fault displacement where meter-level co-seismic fault offsets can be identified [3, 34, 39, 68, 69]. Given that the cross-correlation methods infer displacements by a matching process, the accuracy depends on the quality of the match which, in turn, is determined by any noise within the images. The methods are vulnerable to nonlinear ground deformation and any non-seismic ground feature variation (e.g. seasonal growth of vegetation). Overall, these methods provide at best decimeter-level uncertainty [12]. For aerial photographs, where the look angle is normally close to nadir, they are less sensitive to vertical displacements and the detection is vulnerable to terrain features and texture such as cliffs or vegetated terrain [39].

Figure 2.6 demonstrates the influence of vegetation on optical image correlation for the 2014 Mw 6.0 South Napa, California earthquake. Change detection results using optical imagery are compared with coincident ALS which is known for resistance to vegetation morphology. Shown in (a), optical imagery correlation is compared with ALS differencing for change detection and the residuals are color-coded. (b) shows a digitized mask of vegetated areas. There is a clear spatial correlation between larger differences in the residual map in (a) and the vegetated areas in (b) which suggests compromised detection results for

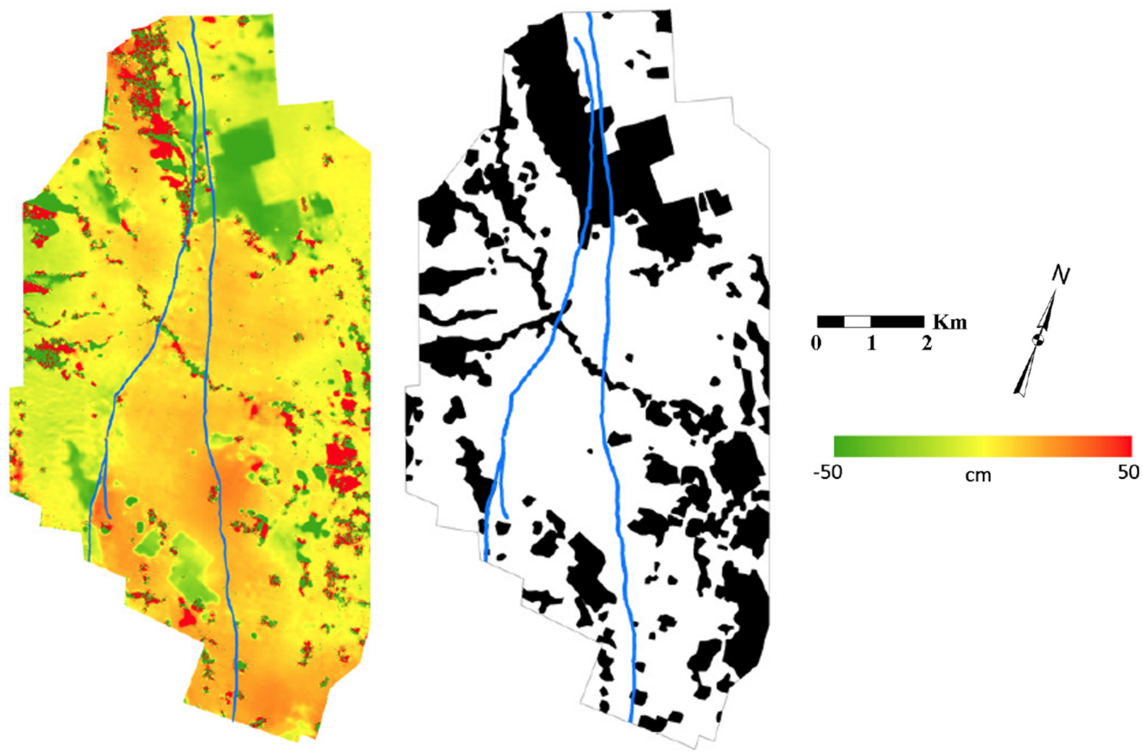

Figure 2.6 The effect of vegetation on the optical imagery change detection results for the 2014 Mw 6.0 South Napa, California earthquake. Figure adapted from Ekhtari and Glennie [12].

the vegetated areas [12].

2.2.2 SAR

Spaceborne SAR can be used to detect earthquake-related surface change in the far field. The method is known for its cost efficiency and spatial coverage. SAR detects synthetic measurements of ground deformation using either amplitude or phase information. Deformation resolved using SAR amplitude is calculated from a cross-correlation scheme similar to what has been described for optical imagery. As an active remote sensing method, it is independent of sun illumination and relatively insensitive to atmospheric interference [70]. However, the change detection results suffer from speckle noise and the resolution is limited by the window size used for pixel cross-correlation [44, 71]. The method offers decimeter-level change detection uncertainty as shown in works by Michel et al. [42, 44].

2.2.3 InSAR

Deformation can also be resolved from phase differences between SAR images through interferometry, i.e. via Interferometric Synthetic Aperture Radar (InSAR). An interferogram can resolve change very accurately (at sub-cm level) but the method has a limited dynamic range of detection. The interferogram will decorrelate if the dynamic range of deformation exceeds the phase unwrapping half-cycle, therefore, the method is vulnerable to large displacements and complex textures (e.g. vegetation) which are commonly found within the near field [40, 44, 45].

InSAR also only detects Line of Sight (LoS) displacement which needs to be projected to reveal 3D displacements. Therefore, the transformation process could induce more uncertainties into the change detection results. The observation geometry of SAR leads to slant range distortion and relief displacement which are more significant if observed at close range [72, 73]. Almost all spaceborne satellites fly at near-polar orbits (i.e. parallel to the NS direction) where the line of sight-projected deformation is less sensitive to the north-south components of ground displacement. Multi-look or multi-orbit LoS data need to be grouped in order to recover three-dimensional (3D) deformation [74, 75].

Nissen et al. [13] compared InSAR-derived and lidar-derived change detection results for the 2011 Mw 7.1 Fukushima-Hamadori Japan earthquake by projecting the lidar-derived displacements onto the InSAR LoS direction. Figure 2.7 (a) shows the lidar-derived change detection results that are transformed into the InSAR LoS format, (b) shows the InSAR dereived LoS displacements, and (c) shows the cross-fault swath profiles for both measurements. The results show that InSAR and lidar-derived changes complement each other as InSAR provides better coverage and consistent measurement in the far field and lidar provides robust records of fault displacement in the near field. Note in Figure 2.7

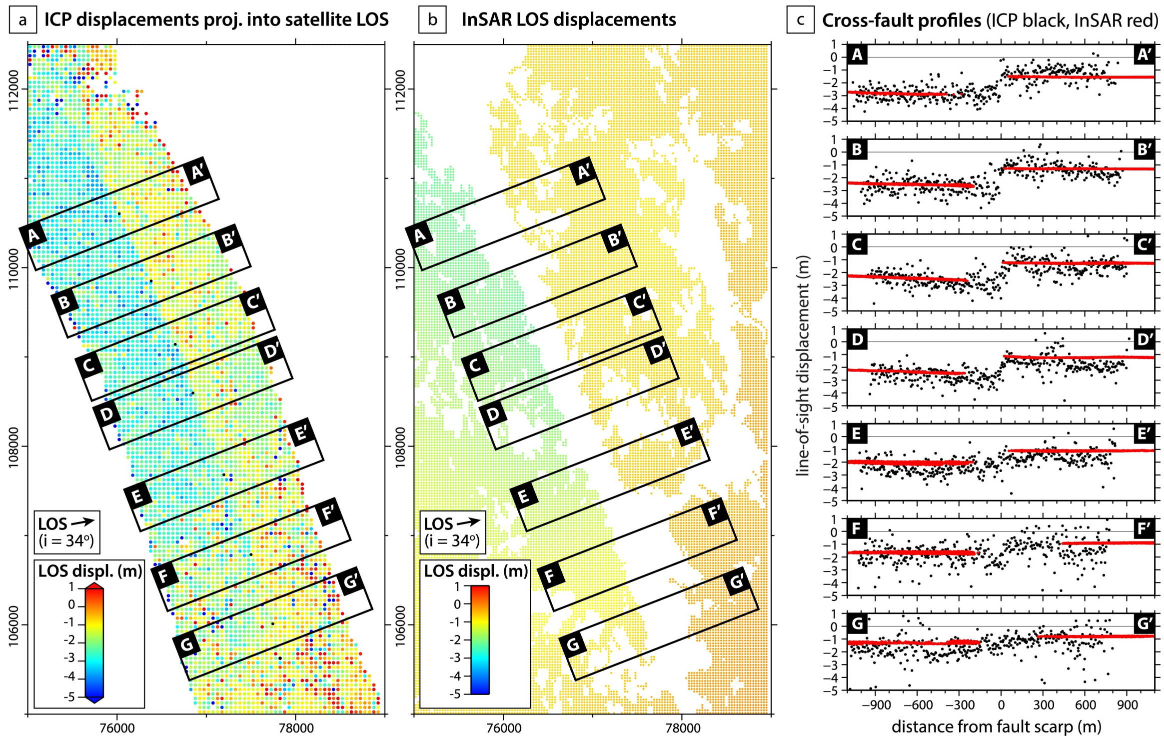

Figure 2.7 Comparison of lidar-derived (a) and InSAR-derived (b) change detection results for the 2011 Mw 7.1 Fukushima-Hamadori Japan earthquake. (c) Cross-fault swath profiles of both measurements. Figure from Nissen et al. [13].

(b) that there are no InSAR estimates of displacement in the near field, the phase unwrapping was not successful because of fault related decorrelation. A similar conclusion can be found in the study by Scott et al. [46].

2.2.4 Lidar

Unlike sparse geodetic observations, lidar and other high definition surveying methods offer dense measurements of fault displacement making it possible to map irregular displacement patterns. Compared with optical imagery and SAR, lidar provides digital measurements of topography at a finer scale due to its significantly higher measurement density; it also has the flexibility to resolve texture in 3D given that lidar pulses can penetrate vegetation using multiple returns [76, 77]. The higher density of lidar records allows topography to be analyzed at various scales and resolution, and the multiple returns enable an expanded line-of-sight dimension to more completely characterize geodetic markers, which are crucial to the recovery of fault displacement [78]. Figure 2.8 demonstrates how object geometry defined by multiple lidar returns is digitized from a return ALS waveform. With multiple returns, lidar can detect the locations of several objects within the laser footprint, making it possible to resolve both ground and above-ground features even with occlusions due to vegetation. Lidar has been gradually adopted as the primary technique to generate Digital Elevation Models (DEMs). To respond to the growing needs for high-quality elevation data, a 3D Elevation Program (3DEP) was established by the U.S. Geological Survey (USGS) where the goal of the project is to acquire nationwide lidar data and provide consistent high-resolution DEMs [79]. As an active remote sensing technique, lidar surveys are also independent of solar illumination, and data collection is flexible given that lidar can be mounted on various platforms including aircraft, vehicles or static tripods. With these benefits, among the commonly used geodetic surveying techniques, lidar can detect distributed displacement and has the advantage of resolving deformation in the near field.

Glennie et al. [77] and Okyay et al. [80] provide overviews of airborne lidar and demonstrate its applications in the study of earthquake, landslide and volcano monitoring, bathymetric mapping, snow depth estimation and archaeological applications. Among various platforms that can carry a lidar, airborne lidar (ALS) is characterized by its large scan swath and nadir looking angle: the platform is operated from a flight height ranging from 50 to 3000 m (50-750 m for helicopter and 600-3000 m for fixed-wing), and the general point density can range from 2-100 pts/m^2. Mounted on an aircraft platform, ALS is the ideal tool to survey topography for a broad area.

Given a constant range of sensing and fixed aperture size, the size of an ideal laser footprint (without considering incidence angle and terrain slope) is determined by the beam divergence of a laser pulse. This beam divergence gives rise to lidar point noise where the actual location of a laser return can be located anywhere within the projected beam footprint

(Figure 2.8). Typically, beam divergence ranges from 0.2 to 1 milliradian (mrad) which is equivalent to 2 to 10 cm at 100 m from the scanner.

Compared with ALS, mobile and terrestrial lidar (MLS and TLS) are collected at shorter target range which leads to a proportional decrease of the laser footprint (and hence point location uncertainty). Compared with MLS, TLS is easier to set up and the georeferencing process does not rely on inertial measurement units (IMU) given the stationary platform, however, MLS is more portable and easier to cover larger areas [81]. DeLong et al. [82] demonstrate an application of earthquake surface deformation detection using a combination of TLS and ALS where 300 fence posts are manually extracted from TLS data to monitor fault displacement for the 2014 Mw 6.0 South Napa earthquake. Compared with their work, shown in Chapter 4, we demonstrate an application of MLS where 2600 posts are extracted automatically and analyzed. In this case, MLS is the more effective method and shows its potential to map the subtle and high-resolution changes in the near field.

In the next chapter, we provide a brief review of current lidar change detection methods that have been applied to detect earthquake-related ground displacement and suggest the potential improvements that led to the proposed change detection framework described by this dissertation.

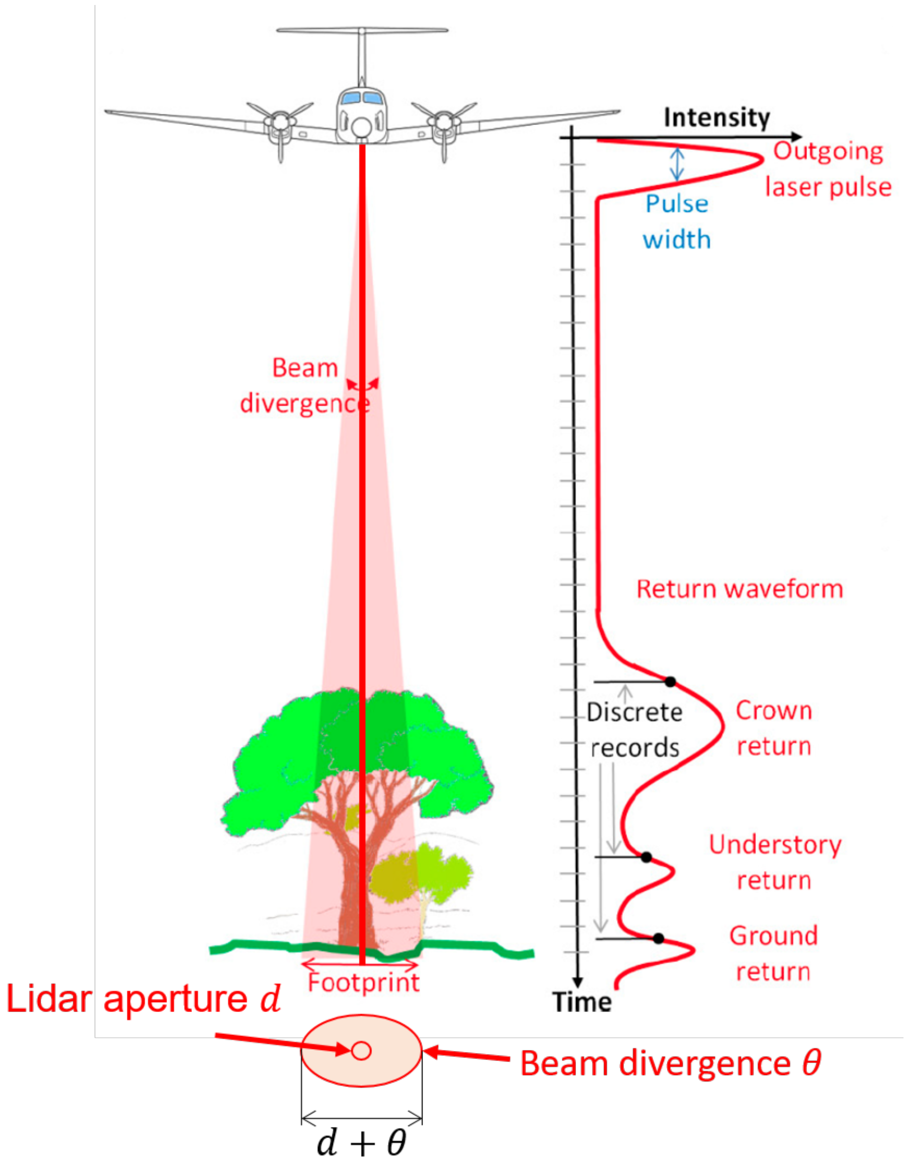

Figure 2.8 Illustration of lidar beam divergence and a waveform of multiple return signals. Figure adapted from Fernandez-Diaz et al. [14].

Chapter 3

Lidar change detection algorithms

Lidar is an acronym for 'light detection and ranging' which is an active remote sensing method for determining ranges to an object with laser measurements. The ranging measurements are recorded as location triplets (X, Y, Z) along with additional attributes describing the laser interactions with the target. With very dense point measurements, lidar represents the 3D geometry of an object with a format referred to as a point cloud.

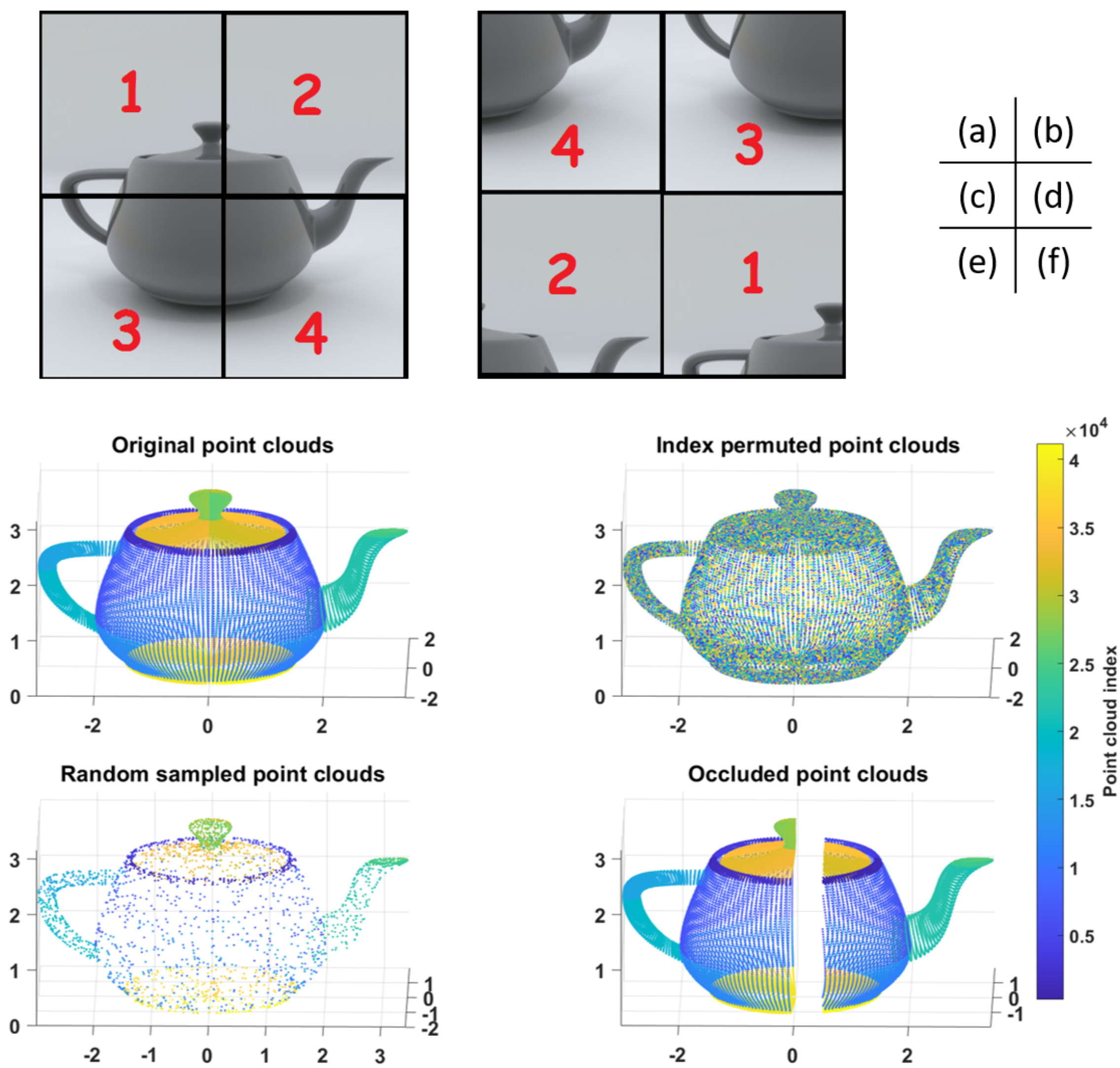

Figure 3.1 Comparison of image (a, b) and point clouds (c-f) format of a Utah teapot [15].

Point clouds are the closest representation of raw 3D scanner sensor data and the representation is very simple - just a collection of points. Dense lidar point clouds carry enough information to represent the 3D geometry of an object independently. However, with improved representation power comes the complex and irregular format of point clouds that makes it hard to process with traditional algorithms. Figure 3.1 demonstrates the irregular format of point clouds by comparing it with the more common image representation. (a) shows an imagery representation of the Utah teapot where pixels are indexed by the displayed number. A permuted-indexed representation of the imagery teapot is shown in (b). (c) shows a point cloud version of the teapot, and the sequence of point clouds is color-coded. (d-f) show randomly permuted, randomly sampled and occluded point cloud representations of the teapot respectively.

One characteristic of the point cloud format is that it is permutation-free. As shown in Figure 3.1(a, b), the content of an image is affected by the rendering sequence of the pixels. However, the point cloud representation is unchanged even when the rendering sequence is randomly permuted (c, d). Such invariance to input permutation makes it ambiguous to process point clouds in a sequenced manner which suggests that point cloud indexes cannot be used like the imagery (row, column) indexes in change detection. For example, metrics that describe neighborhood points are defined by the mutual distance between the points rather than point indexes, unlike the image kernel that is commonly implemented as convolution by row and column. Equation 2.3 would fail if applied to point clouds given that there is not a stable correspondence between the sequence and the content stored within a point cloud.

The other characteristic of the point cloud format is that the representation is redundant and irregular. Point clouds still preserve the geometry of an object even when the point clouds are randomly downsampled or occluded as shown in (e, f). As a redundant representation, the location (e.g. centroid) of the teapot is insensitive to the redundant point records even if part of the point cloud is occluded (f). These characteristics make point clouds an ideal format to map the complex deformation of ground rupture found in the near field but also introduce additional complexity to process point cloud-based change detection results. Just as computational algorithms depend on data structures (lists, trees, graphs, etc.), different applications of change detection have their own preferences for regularizing the point cloud format and detecting change. Change detection using lidar data is the process of identifying the event-induced differences within the point clouds while resisting the data-driven differences caused by the irregular point cloud format.

3.1 DEM-based change detection

Image-based cross-correlation change detection strategies were well-developed before the appearance of lidar techniques. Therefore, early applications first converted point clouds into image-like formats such as high-resolution digital elevation models (DEMs) or digital surface models (DSMs). The conversion compresses the 3D point clouds into a '2.5D' raster where each pixel value stores a single elevation number estimated from the point cloud records. Once the point clouds are converted to DEMs or DSMs, most image-based processing methods are applicable and displacements can be detected by comparing DEMs collected from different epochs. Such methods include DEMs of difference (DoDs), sloped-based change detection, and particle imaging velocimetry (PIV).

3.1.1 DEMs of Difference (DoDs)

DEMs of differences (DoDs) calculates direct elevation differences between two DEMs resulting in volumetric change for the survey area. Examples of DoDs applications includes change detection of glacier surface elevation, stream channel deposits, and landslides. Williams [83] provides a comprehensive overview of geoscience applications using the DoDs method. The method does not require object classification and the detection results can be post-classified by different sources of deformation. The method fails when the displacement is not limited to the vertical direction, and the detection requires accurate registration of DEMs prior to the differencing process [83, 84]. The method is rarely used on earthquake-related deformation given that it is insensitive to horizontal motion.

3.1.2 Slope-based change detection

Slope-based change detection is a successor to DoDs where elevation differences in a sloped area can be interpreted as a combination of horizontal and vertical offset [16]. As shown in Figure 3.2, given local slope measurements m_X and elevation differences ΔZ, systematic horizontal and vertical offsets (X_{offset}, Z_{offset}) can be solved through a linear regression.

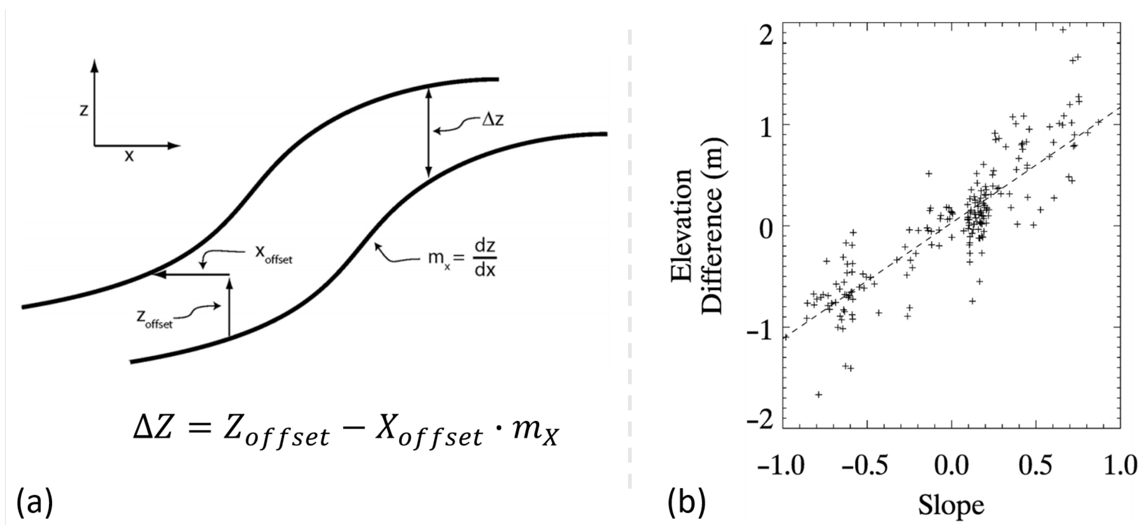

Figure 3.2 (a) Profiles of terrain under systematic horizontal and vertical offsets. (b) Scatterplot of the elevation difference versus local slope for profiles in (a). The dashed line shows the linear trend. Figure adapted from Streutker et al. [16].

However the correlation shown in Figure 3.2(b) is unstable and vulnerable to discrete topography and nonlinear deformation. If the local topography is rugged, the correlation will be neither strong or linear. As shown in Figure 3.3, a simulated displacement ($X_{offset} = 10m, Z_{offset} = 0.2m,$) has been applied to terrain with different terrain ruggedness (a-c). The correlations between the elevation difference versus local slope are shown in (d-f). As terrain ruggedness increases, the elevation-slope scatter plots (d-f) shows a weaker and nonlinear correlation. Therefore, the method only works at regional scales where stable

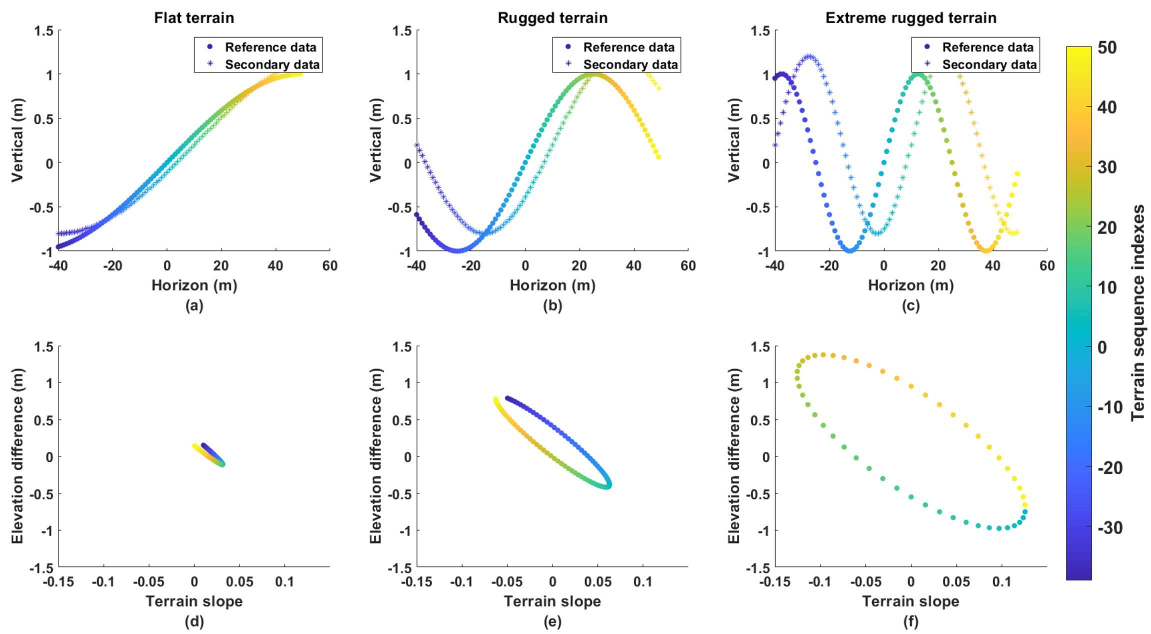

Figure 3.3 Synthetic change detection using the slope-based method. A simulated displacement is applied to terrain with different ruggedness (a-c). Scatter plots (d-f) show the correlation between the elevation difference versus local slope.

correlations exist, it does not scale with increased variation. The method has a limited application for change detection of natural surfaces where the topography is rugged or the deformation is nonlinear.

3.1.3 Particle Image Velocimetry (PIV)

PIV was originally developed to trace the velocity of fluid flows seeded with particles from time series photography [85, 86]. The method is similar to image change detection as cross-correlation schemes are applied to DEMs and features extracted from DEMs. Applications of PIV in geoscience include, but are not limited to, detection of landslides [87], earthquake surface displacements [88], and glacier movement [89].

As a cross-correlation-based method, various image-based morphological kernels and filters of various sizes are applied to the DEMs to extract and enhance features that contribute to cross-correlation. As a result of the filtering, the fidelity of PIV change detection is compromised because the elevation information is altered by the filters. For example, a larger window filter will tend to smooth the high frequency changes in the DEM. Also, as a method using the image cross-correlation, PIV only estimates horizontal changes.

3.2 Point cloud based change detection

Despite the convenience of applying well-developed image-based change detection algorithms, all of the DEM-based methods suffer from information loss due to transforming 3D point clouds to 2.5D DEM rasters. The interpolation process to prepare DEMs smooths the representation of the topography and degrades the resolution and sensitivity of change detection. The compression and smoothing of the vertical component reduces the number of distinctive features that can be used to trace the deformation, especially in the lateral direction. Therefore, the quality of the change detection can be improved by directly working on the 3D representations of topography without reducing the valuable geometric information.

Although properly geo-referenced DEMs can provide information about surface dynamics, 3D representations of topography are preferred to predict ground surface kinematics for applications like tectonic studies, and landscape evolution[77]. As a simple 3D format, point clouds represent the geometry of an object in 3D, and change detection can be implemented directly on point clouds and on point-cloud-derived 3D models.

3.2.1 Iterative closest point (ICP)

Iterative closest point (ICP) is a method originally used to match and register two point clouds. It was first proposed by Besl and McKay [90]. The method detects displacement as the transformation needed to align the corresponding point clouds. The method uses a least squares adjustment that iteratively matches the corresponding point clouds by minimizing the sum of the distances between the corresponding closet points. A flowchart of ICP is given in Figure 3.4.

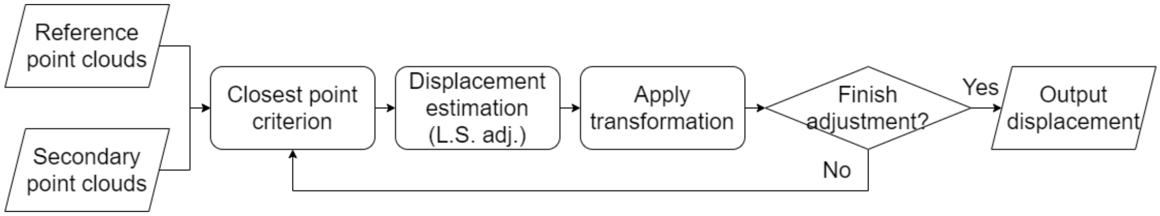

Figure 3.4 Standard flowchart of ICP (L.S. adj. is the acronym for least squares adjustment).

ICP is the first 3D change detection method that has been efficiently applied to earthquake-related change detection. Studies like Zhang et al. [48] and Scott et al. [43] show that ICP has the potential to detect displacement at the dm level. However, the method is incapable of resolving cm-level changes [12]. This is because the matching strategy for the closest point criterion tends to diverge when changes are at levels that are close to or smaller than the size of a laser footprint (Figure 2.8). The point-to-point correspondence assigned by the closest point criterion suffers from a matching uncertainty in addition to the point cloud uncertainties. Such deficiencies limit the power of detecting subtle changes, and therefore ICP change detection results suffer from increased estimated uncertainties in the near field of a fault [8, 48].

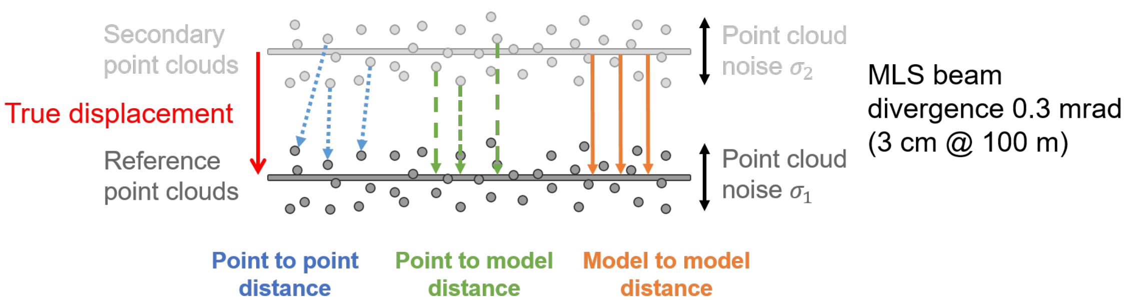

Figure 3.5 Illustration of point-to-point distance (dot blue arrows), point-to-model distance (dash green arrows) and model-to-model distance (solid orange arrows).

Figure 3.5 illustrates the different strategies for matching corresponding point clouds using point-to-point (p2p) distances [91], point-to-model (p2m) distances [92] and model-to-model (m2m) distances [93]. The true displacement vector, shown in red, represents the ideal change detection result between the secondary point cloud and the reference point cloud, and point cloud noise (laser footprint) due to laser beam divergence is marked by σ_i. In general, m2m distances are the most consistent and closest estimate of the true displacement while p2m and p2p distances show increasing variation respectively. Standard ICP normally uses the closest point criterion calculated from the p2p distances which is less efficient for corresponding point clouds. Therefore, substituting p2p distances with p2m generally improves the ICP performance especially if the two point clouds are sparse or at different resolutions [91, 93]. Other possible improvements to ICP include: (1) performing ICP with a moving window detector such that sub-window resolution is possible, (2) incorporating anisotropic point uncertainties such that robust matching results can be achieved [48], and (3) substituting the p2p distances with Hausdorff distances [94, 95].

3.2.2 Model-based methods

Unlike point cloud representations of 3D geometry, model-based methods represent an object geometry by compact models. In computer vision, a geometric model that can be described by an equation with a number of free parameters is called a geometric primitive [96]. Compared with the redundant point cloud representation, locations of geometric primitives can be described by only a few free parameters, therefore, giving high degrees of freedom. Compared with irregular and incomplete point cloud formats, a geometric primitive representation is less vulnerable to point noise and scan occlusion [97]. Therefore it may be optimal to identify objects and detect displacement by tracing the changes in geometric primitive parameters. When modeled with redundancy, geometric primitives can be positioned with higher accuracy than the individual lidar point noise and potentially determine change detection at higher accuracy.

Figure 3.6 is an experiment to compare the detection capability using ICP-p2p, ICP-p2m and model-based change detection methods. The point clouds are randomly generated from a sphere of 1 m $\pm$ 3 cm (1σ) radius. Synthetic random displacement vectors ($Disp.(m) \sim N(0,1)$), represented by the red arrow, were generated for the spherical point

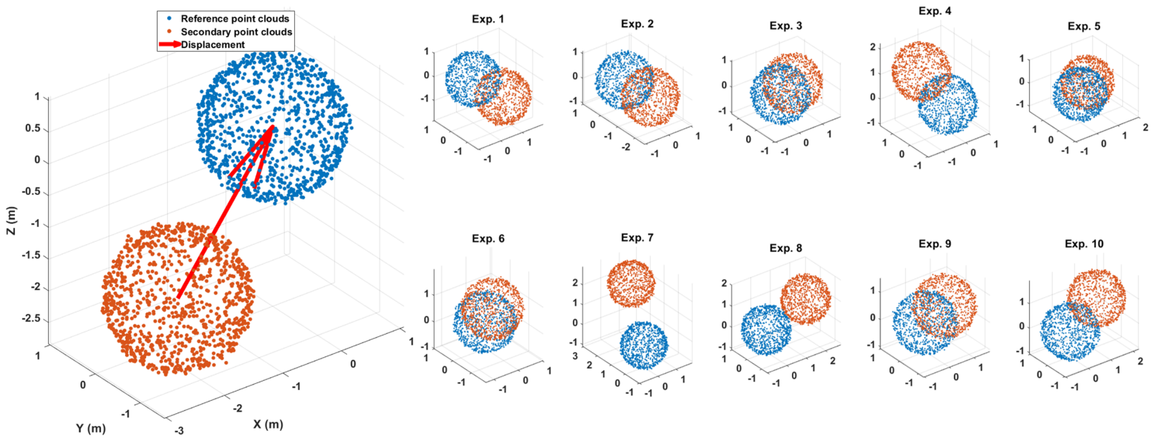

(a) (b)

Figure 3.6 Synthetic displacement data. (a) A demo of synthetic spherical point clouds undergoing a rigid transformation. (b) Ten samples of simulated displaced point clouds.

clouds, and the point clouds are simulated from a sphere of 1 m radius with 3 cm digitizing uncertainties, that simulates a lidar beam divergence of 0.3 mrad (i.e. beam diameter of 3 cm at 100 m scan range). Given 100 simulated datasets, the three methods are applied to recover the simulated displacement, and the quality of the detection is reflected by the residuals, i.e. the difference between the detected and simulated displacement. The difference between the detected and simulated displacement is calculated as

$$\begin{bmatrix} dX \\ dY \\ dZ \end{bmatrix}_i = \begin{bmatrix} X_{detected} \\ Y_{detected} \\ Z_{detected} \end{bmatrix}_i - \begin{bmatrix} X_{simulated} \\ Y_{simulated} \\ Z_{simulated} \end{bmatrix}_i, (i = 1, 2, ..., 100), \tag{3.1}$$

and the results are shown in Table 3.1. This experiment shows that ICP-p2p, ICP-p2m and model-based change detection methods misidentify the simulated change by 13 mm, 7 mm and 4 mm respectively. Model-based method shows the most reliable results among the three.

Table 3.1 Comparison of three change detection methods: ICP-p2p, ICP-p2m, and model-based.

Method	Mean of res.			Var. of res.			Mean of res.	Var. of res.
Unit(mm)	$\overline{dX}$	$\overline{dY}$	$\overline{dZ}$	$\sigma(dX)$	$\sigma(dY)$	$\sigma(dZ)$	$\overline{\sqrt{X^2+Y^2+Z^2}}$	$\sigma(\sqrt{X^2+Y^2+Z^2})$
ICP-p2p	-0.93	-0.44	0.29	9.13	8.32	8.74	13.49	0.047
ICP-p2m	-0.27	-0.38	-0.07	4.40	3.82	4.22	6.71	0.007
M-based	-0.12	-0.11	-0.04	2.28	2.52	2.61	3.96	0.003

Besides higher change detection sensitivity, model-based change detection is also robust to scan occlusions (e.g. Figure 3.7) which are commonly found in side-looking MLS surveys. Despite these benefits, there are limited change detection strategies that incorporate a modeling process, and they have not been applied to detect fault displacements in the near field. Therefore, we have developed a framework for model-based change detection and applied it to the detection of co-, post- (Chapter 4) and inter-seismic (Chapter 5 and 6) fault displacement, with emphasis on describing the non-linear deformation in the near field.

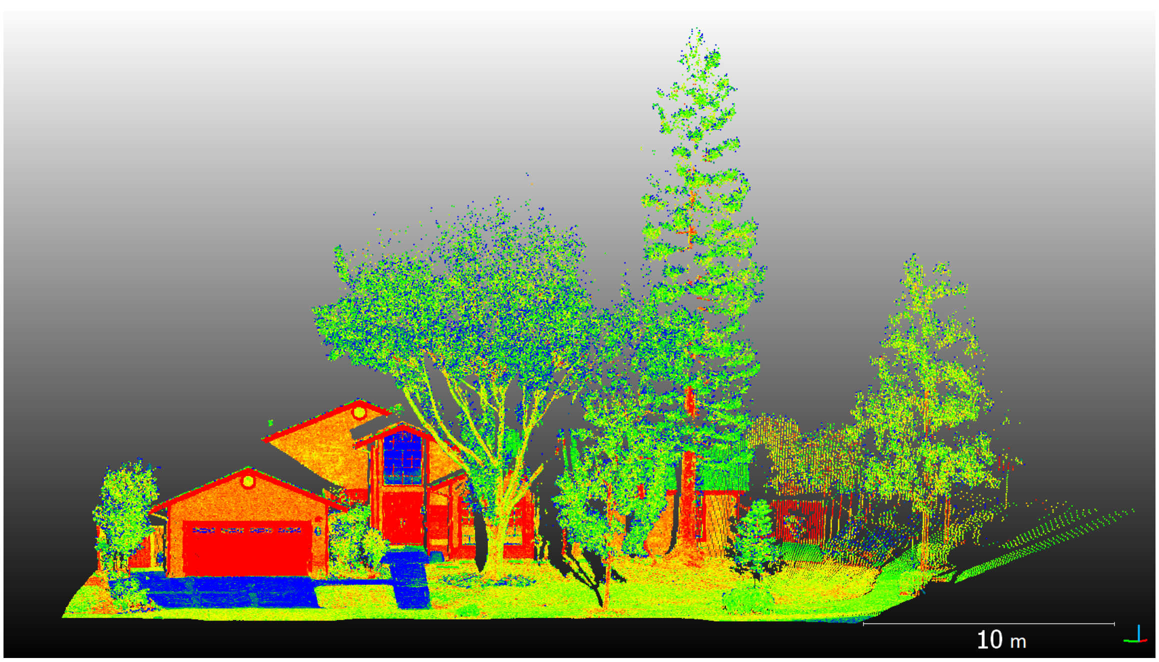

Figure 3.7 Scan occlusion patterns in a sample point cloud. Point clouds are randomly colored, and scan occlusions can be found on the roof of the house and on the wall behind the tree trunks, for example.

Chapter 4

Automated Near-field Deformation Detection from Mobile Laser Scanning for the 2014 Mw 6.0 South Napa Earthquake

This chapter is a modified version of the following peer reviewed journal paper: Xinxiang Zhu, Craig L Glennie, and Benjamin A Brooks. Automated near-field deformation detection from mobile laser scanning for the 2014 Mw 6.0 South Napa earthquake. *Journal of Applied Geodesy*, 16(1):65–79, 2022.

4.1 Introduction

High-resolution mapping of surface deformation caused by earthquakes is important for both earthquake hazard mitigation and increased understanding of earthquake fault dynamics [98]. Various geodetic observations and strategies for estimating change have been developed to capture earthquake ground deformation. However, few current techniques have the ability to deliver accurate (cm-level) and high resolution (decimeter level spacing) fields of distributed displacements for an earthquake in the near field (i.e. closer than 200 m to the fault trace). Global navigation satellite system (GNSS) data is able to estimate static [99] and dynamic [19, 100] seismic displacement with subcentimeter precision. However, the spatial coverage of GNSS data is restricted by the spatial distribution of the GNSS receivers which are generally too sparse to monitor near-field fault deformation. Interferometric synthetic-aperture radar (InSAR) is also capable of delineating far-field earthquake deformation over a broad area with centimeter-level precision[101]. However, interferograms tend to decorrelate with spatial change and are vulnerable to large displacements and complex textures (such as vegetation) on the ground. Earthquake ruptures are characterized by complex deformation patterns, and a dislocated ground surface makes InSAR phase unwrapping near the surface deformation difficult [44, 45]. Optical imagery datasets can also be used for deformation detection [102], but only provide horizontal motion, and in general are unable to provide better than decimeter level accuracy, even with high-resolution images [12]. Therefore, although all these geodetic observations serve as important products for post-earthquake analysis [103], none of them are currently capable of capturing high accuracy and high-resolution rupture deformation in the near field.

Two of the most commonly used strategies for near field earthquake deformation detection are correlation-based and registration-based change detection using either optical imagery or lidar. For example, Milliner et al., (2015) used an image correlation-based method to quantify the horizontal displacement of the 1992 M_w 7.3 Landers, California earthquake [39]. The method produced decimeter accuracy horizontally but does not provide vertical motion. The resolution of the correlation-based algorithm is also affected by the required size of the correlation search window. Larger window sizes are required for improved correlation but makes the technique insensitive to subtle local changes. Smaller window sizes will be more sensitive to subtle changes but in general lead to noisier correlation results. 3D-based earthquake deformation using the iterative closest point algorithm (ICP) has been implemented using both lidar and structure from motion (SfM) point clouds, [43, 47, 48, 104], for example. Zhang et al., (2015) used ICP to estimate earthquake deformation for the 2010 M_w 7.2 EI Mayor-Cucapah earthquake [48], Scott et al., (2018) estimated deformation for the M_w 7 2016 Kumamoto, Japan earthquake [43], and Scott et al., (2020) used ICP to estimate the long term creep rate for a section of the Central San Andreas and Calaveras faults [47]. The ICP method using airborne laser scanning (ALS) observations works well when expected displacements are larger than the decimeter-level uncertainty [12]. The spatial resolution of ICP is also limited by the size of the correlation window which is generally 20 to 100 meters [13, 43, 47, 48, 105–107]. ICP assumes uniform deformation within the correlation windows (e.g. [108]) and therefore the method may artificially smooth near-field deformation estimates. Both image-based correlation and ICP implicitly assume that spatial features within the search window are rigidly transformed and not deformed during the earthquake. The search window size has to be chosen wisely to balance detection resolution (using a smaller window size) and robustness (using a larger window size). It is challenging to keep this balance in the near field due to the complex geometry of the topography, the nonlinearity of the deformation pattern, and possible incomplete representation of the scene due to data occlusions.

Compared with ICP and image correlation, geometric model-based change detection removes the constraint of rigid deformation within a search window. Geometric model-based methods interpret the point clouds using models with simple geometry, i.e. geometric primitives. Changes are derived by tracking primitive movement between epochs. Kusari et al., (2015) showed that sub-centimeter level changes can be estimated by matching geometric models of building walls and roofs which are estimated from point clouds captured on planar surfaces [109]. Their method shows the potential for high-accuracy change detection using a sparse and redundant representation of the point clouds with simple geometric primitives. However, this method cannot estimate fault displacement from a single planar geometric primitive because it is only sensitive to motion along the plane normal; therefore several surfaces need to be amalgamated to estimate 3D displacement. In contrast, DeLong et al., (2015) used manually identified fence-posts and a cylindrical model to directly show centimeter-level changes from the 2014 M_w 6.0 South Napa earthquake [82]. The difference in pre- and post-event 3D cylinder locations was able to directly provide estimates of surface displacement for each post. Although these initial results were promising, the fence posts had to be manually identified and modeled. We propose an automated method of geometric primitive identification, matching, and displacement estimation to provide a more widely distributed model of earthquake deformation.

Using mobile laser scanning (MLS), we acquired 3D point clouds representing the geometry of fault-related surface displacements with sub-centimeter accuracy for the 2014

M_w 6.0 South Napa earthquake [5, 6]. Minimal co-seismic offset, including co-seismic and early post-seismic displacements 7 days after the earthquake [1], is detected by monitoring deformation of planar primitives representing the geometry of vineyard rows which were straight prior to the earthquake. Cylindrical primitives are generated with a workflow relying on PointNet [18], RANdom SAmple Consensus (RANSAC) [110], and least squares fitting. post-seismic surface displacements are detected by tracking the cylindrical primitives between epochs of MLS data collected 7 and 34 days after the earthquake, and it is shown that this method has the ability to detect centimeter-level ground displacement in the near field at sub-centimeter level precision. The detection results provide new observations of fault-related surface displacements with high-resolution and accuracy. Distributed ground displacements detected near the fault trace are important for the study of rupture mechanisms for active faults. The proposed semantic primitives can be implemented in automated point cloud-based change detection and automatic point cloud segmentation.

The rest of this paper is organized as follows: The MLS datasets from the 2014 M_w 6.0 South Napa earthquake are briefly described. The change detection strategy is demonstrated in the methodology section. Change detection results are presented for co-seismic response, fault trace estimation, and post-seismic deformation detection. Continuity of the rupture zone is interpreted and discussed followed by analyses of off-fault deformation distribution and uncertainties within the detection results.

4.2 MLS survey and dataset for the 2014 Mw 6.0 South Napa earthquake

The M_w 6.0 South Napa earthquake of 24 August 2014 was the largest earthquake in over 25 years for the San Francisco Bay Area, causing over half a billion dollars of

[1] For simplicity, we refer to the detected co-seismic and early post-seismic displacements 7 days after the earthquake as co-seismic offset for the rest of the paper.

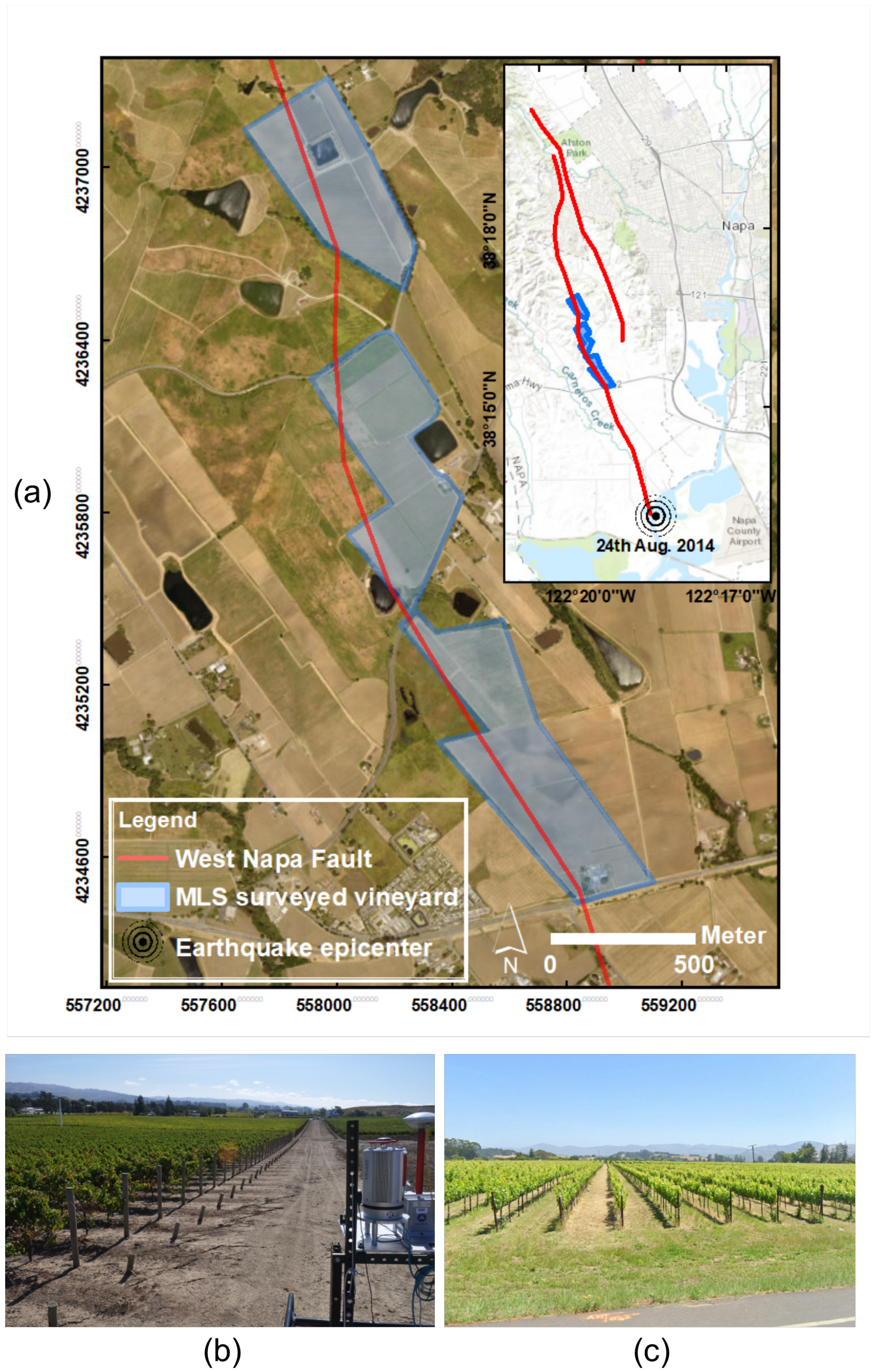

Figure 4.1 Overview of MLS survey area (a). Mobile laser scanner and images of vineyard rows (b, c).

economic damage. The earthquake was nucleated on the active West Napa Fault, a right-lateral strike-slip fault. In situ measurements were made documenting the co-seismic surface displacements ranging from 5-50 cm largely confined to the Great Valley Group – bedrock resulting from Mesozoic forearc basin sedimentation – in the northern part of the rupture, whereas shallow afterslip occurred within a Quaternary alluvial basin to the south [53], [111]. Two MLS surveys [6] were conducted to document earthquake deformation using a RIEGL VZ-400 scanner; the first survey was on September 1 and 2, 2014 and the second on September 28-30, 2014. Laser point density was approximately 280 points per square meter at a distance of 50 m from the scanner.

Our study area is a subset of the MLS survey and comprises several vineyards where the fault trace crossed the vineyard rows approximately perpendicularly. Figure 4.1 shows the study area and representative pictures of vineyard rows. The average vine row length is approximately 250 m with anchor posts at two ends spanning each row. The average interval between rows is approximately 2.3 m. Vineyard rows were originally constructed to be straight lines with constant intervals between plants to maximize sunshine, therefore, any curvature, dislocation of tiles and posts can be confidently attributed to the 2014 South Napa earthquake [6]. Minimal co-seismic offset is estimated in the first MLS survey; post-seismic surface displacements are monitored between the two MLS surveys. Because of the primarily dextral nature of the Napa earthquake, we focus our method to examine only the horizontal components of deformation.

4.3 Change detection Methodology

The key concept of the proposed change detection strategy is to represent MLS point clouds with geometric primitives and derive changes by tracking these primitives between temporally spaced datasets. Geometric primitive is a term from computer vision referring to simple geometry of an object that can be described by an equation with a number of free parameters [96]. In this case, geometric data are unordered lists of MLS point returns in three-dimensional Cartesian space and simple geometries are planar and cylindrical primitives representing outlines of objects scanned by the lidar scanner. With augmentation by additional semantics, planar vineyard row primitives and cylindrical fence post primitives are generated from MLS point clouds. As sparse and redundant representations of point clouds, geometric primitives are highly effective geodetic markers that can be temporally tracked to reveal ground displacement.

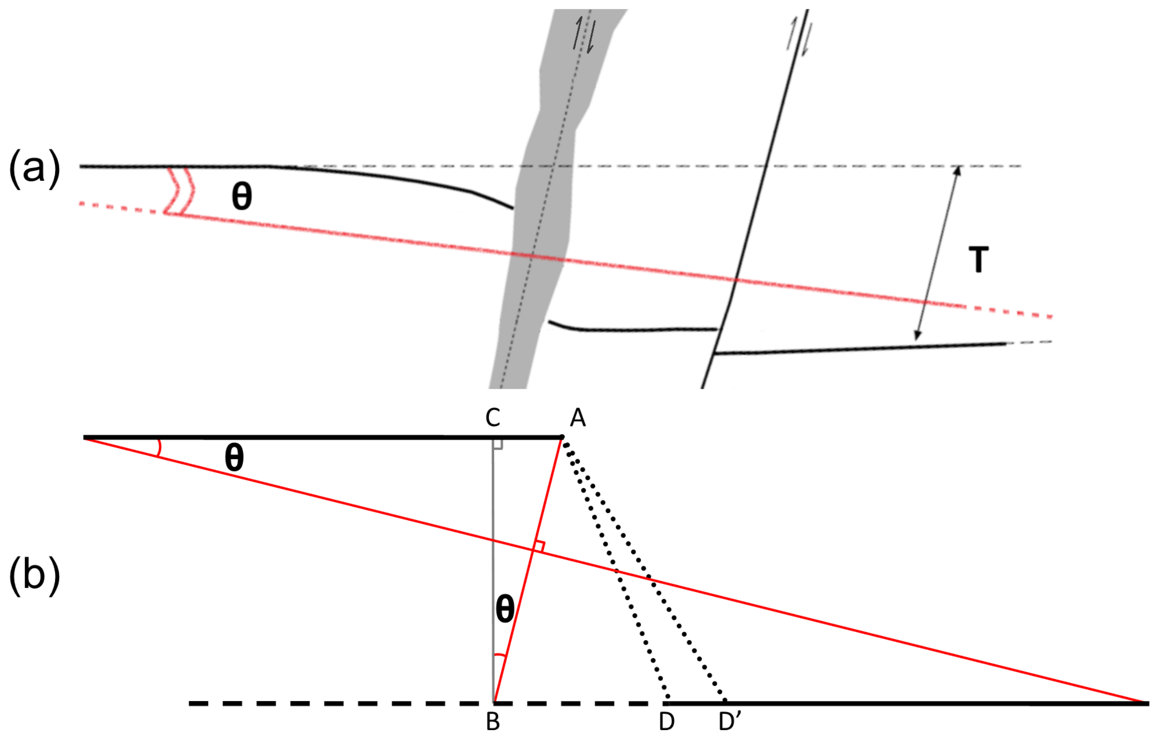

Figure 4.2 Schematic (a) and geometric (b) drawing of planar features crossing the surface rupture (grey zone). Figure (a) adapted from a graphic given in [17].

The total near-field displacement consists of on-fault brittle deformation in the principal and secondary fault zone, and off-fault deformation [17, 39]. Figure 4.2 shows a schematic drawing (a) and a geometric drawing (b) of planar features crossing the synthetic surface ruptures of an earthquake. Total near-field displacement is labeled as T. Given that the row length (about 250 m) is about 500 time larger than the displacement (about 50 cm) the angle θ is small enough ($1 - \cos\theta \approx 2 \times 10^{-6}$) that the deviation from the reconstructed plane (**AB**) serves as a good approximation of the minimum co-seismic offset (**BC**). Note that the offset does not reflect the true estimates of accumulated deformation (**AD** or **AD'**) as surface rupture was expressed as en echelon fractures. Referring to these setup, the objectives of the proposed change detection are to:

- Delineate fault trace locations.
- Quantify near-field displacements within approximately 200 m of the fault trace.
- Summarize displacement distributions versus off-fault distance.

Table 4.1 shows the basic change detection strategies with detailed descriptions of the methodology given in the following sub-sections.

Table 4.1 MLS change detection strategies

Process	Change detection for minimal co-seismic offsets	Change detection for post-seismic surface displacements
Input data	Point clouds of the top of vine rows	Point clouds representing vineyard posts
Primitive type	Planar primitives defined by vinerow end posts	Cylindrical primitives extracted using PointNet [18], filtered using RANSAC and modeled using a least squares adjustment
Detection methods	Measure point to plane distances	Cylindrical primitive locations observed at two epochs
Output instances	Total deformation of 1300 vine rows 7 days post earthquake, and estimation of the fault trace	Displacements of 2600 posts between 7 and 34 days post earthquake

4.3.1 Change detection using planar primitives for co-seismic response

co-seismic response is approximated using offsets from planar primitives modeled from the top part of the scanned vine row. Each vine row is cropped using a bounding box with a width of 3 m and defined by the posts located at the ends of each row, where post locations are manually digitized from the MLS data. The top 20 cm portion of each row is automatically extracted and analyzed using a moving window. Due to scanner occlusions for the lower part of the vines, only the top part of the vine point clouds are extracted to ensure complete spatial coverage. A 2D plane is constructed spanning the post locations with the planar normal parallel to the ground. Deviations from this plane estimate vine row dislocation due to the Napa earthquake, and normal distances from this plane are calculated which approximate total co-seismic offsets.

With raw MLS data as input, point clouds within the moving window are filtered to remove outliers based on distances to nearest neighbors [112], and offsets from planar primitives are calculated as averaged point-to-plane normal distances within a 1 m window. Turning points are detected where the offsets change signs. A series of consistent turning points are used for an estimation of a digital fault trace. Given that the row length (about 250 m) is about 500 times larger than the displacement amount (about 50 cm), the angle (θ in Figure 4.2) between the plane normal and dislocation direction is small enough ($1-\cos\theta \approx 2\times10^{-6}$) that deviation from the reconstructed plane (detected as minimal co-seismic offset) serves as a good approximation of the co-seismic response. Repeating this process over all the extracted rows, distributed horizontal displacements are derived estimating the minimum co-seismic offset along the fault trace. Note that we cannot guarantee that both (a) the vine rows were completely straight before the earthquake and (b) the posts' locations selected as end points accurately depict the optimal plane location. Therefore, the offsets from the planar primitive should not be evaluated as true estimates of accumulated deformation (Figure 4.2 (b) **AD**) but rather the minimum co-seismic offset (Figure 4.2 (b) **BC**) approximated by the planar residuals as (Figure 4.2 (b) **AB**). However, these deviations from the plane do enable an accurate estimation of the fault line location and also allow the examination of displacement curvature near the fault.

4.3.2 Change detection using cylindrical primitives for post-seismic surface displacement estimation

post-seismic surface displacement is estimated using the displacement of cylindrical primitives between two temporally spaced MLS surveys. To model the cylindrical primitives, which represent scanned posts at the end of each vine row (figure 4.3), the point

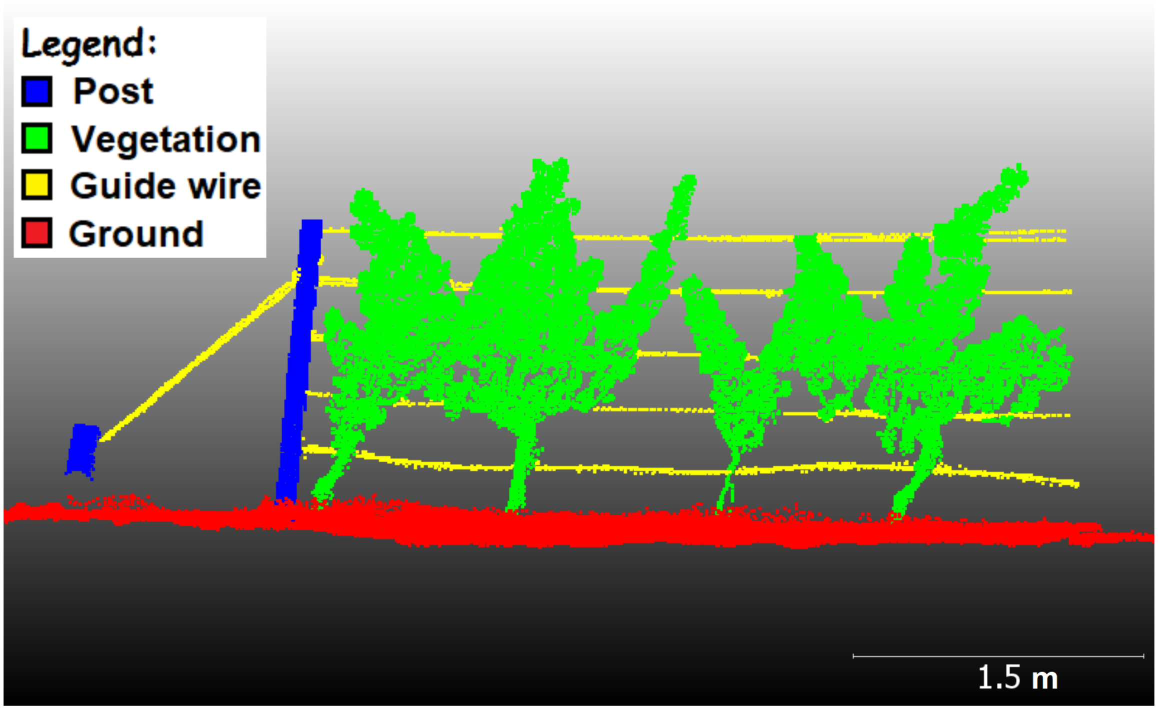

Figure 4.3 Segmentation example for a portion of a single vine row. MLS point clouds were automatically segmented into four categories using PointNet.

clouds first need to be segmented. In previous work, the segmentation was manually performed [82]. To automate this process, we implement a deep neural network - PointNet [18] to automatically segment the MLS point clouds. The segmented datasets are later filtered using RANSAC [110] and modeled as primitives using a least squares adjustment. Displacements are derived by tracking the relative motion of the cylindrical primitives between the two epochs of MLS data.

4.3.2.1 PointNet: automated point cloud segmentation

PointNet, proposed by [18] is a unique deep neural network that directly works on 3D point clouds. The method and its variants have been applied as a common strategy for lidar point cloud semantic segmentation (e.g. [113–116]). The network learns a set of optimization functions selecting informative points and aggregates the optimization results as global descriptors. Fully connected layers and symmetric max-pooling functions are implemented to handle the irregular format of point clouds. Figure 4.4 shows the basic

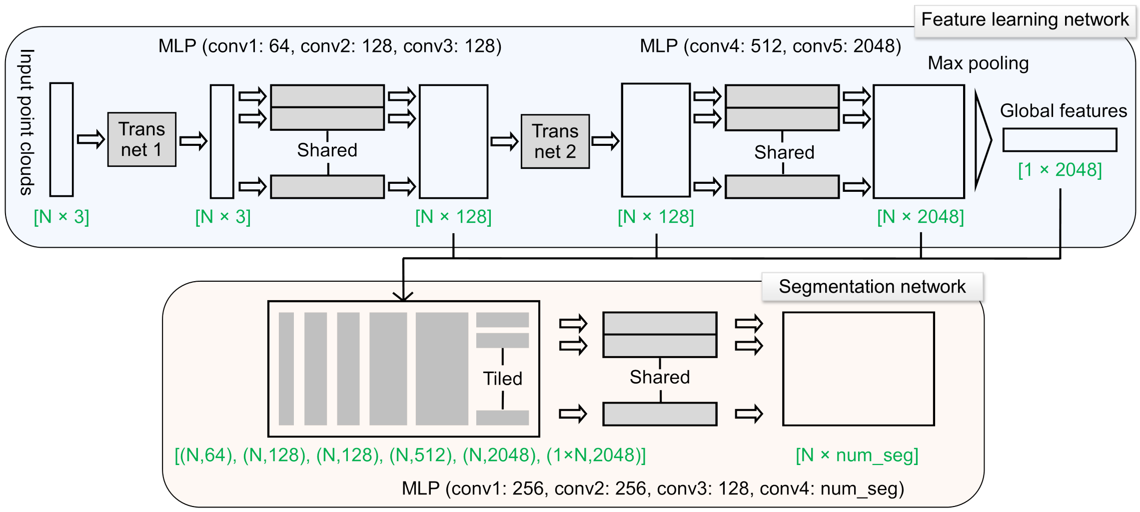

Figure 4.4 Schematic Structure of PointNet [18]. Feature learning network on top, and segmentation network on bottom.

structure of PointNet for point cloud segmentation. The network consists of two major parts: a feature learning network that learns with fully connected layer structures ended with a max-pooling layer and a segmentation network that augments learned local and global features and outputs per point labels as segmentation results.

For supervised learning on point clouds, we set up a vine row training set where 120 scanned vineyard row point clouds are manually labeled, consisting of 9 million total labeled points. Every point within this set falls into one of four categories – (1) posts, (2) vegetation, (3) guide wire and (4) ground. Random sampling from this training set generates over 40 thousand training samples, where each sample consists of 2048 points in a single vine row. The train-validation-test split is 7:1:2. Figure 4.3 shows a segmentation example where point clouds were automatically segmented into the four categories. After training, the network is capable of processing all 2600 scanned sections of vineyard posts, which consist of over 300 million MLS laser returns. The point clouds were automatically segmented into the four categories and the posts were then extracted for cylindrical primitives modeling. Herein, only the end posts are analyzed because the middle posts were often occluded by the vine row vegetation.

4.3.2.2 Cylindrical primitives modeling

The segmented posts were modeled as cylindrical primitives and then pre- and post-deformation primitives were clustered by their locations. A Gauss-Helmert model [117] is used for least squares fitting of the cylindrical primitives as

$$g(l+e,p) = X^2 + Y^2 - r^2 = 0, \tag{4.1}$$

$$\text{where} \begin{bmatrix} X \\ Y \\ Z \end{bmatrix} = R_2(\phi)R_1(\omega) \begin{bmatrix} x_{obs.} \\ y_{obs.} \\ z_{obs.} - \overline{z_{obs.}} \end{bmatrix}, \tag{4.2}$$

$$R_1(\omega) = \begin{bmatrix} 1 & 0 & 0 \\ 0 & \cos\omega & \sin\omega \\ 0 & -\sin\omega & \cos\omega \end{bmatrix}, \tag{4.3}$$

$$\text{and} R_2(\phi) = \begin{bmatrix} \cos\phi & 0 & -\sin\phi \\ 0 & 1 & 0 \\ \sin\phi & 0 & \cos\phi \end{bmatrix}, \tag{4.4}$$

where the inputs are MLS laser returns for a single post $[x_{obs.}, y_{obs.}, z_{obs.}]^T$ with measurement uncertainties e. The point clouds are shifted and rotated so that a cylinder can be estimated at the center of each cloud with a vertical axis. The estimated parameters p are shift components (X,Y), and rotation angles (ω,ϕ) for the x- and y-axis. The radius r of the cylinder is fixed at 5 inches (12.7 cm) for the observed anchor posts.

The top face of a scanned post is usually missing or occluded by vegetation due to the sideways field of view of the mobile scanner. As a consequence, the height of each

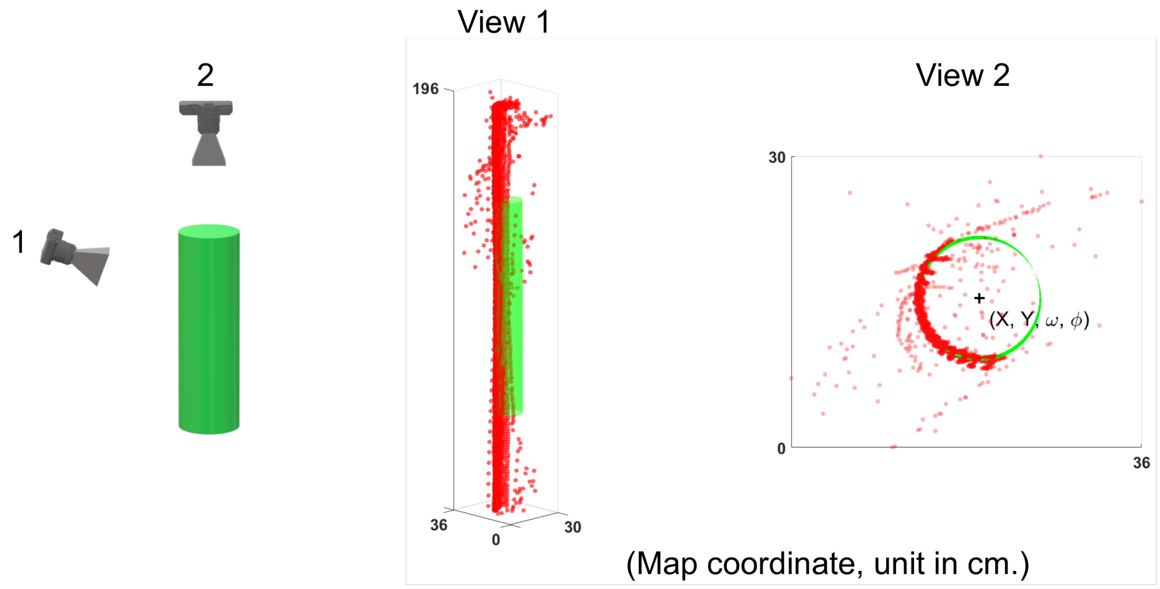

Figure 4.5 Example of a cylinder primitive. Red dots are segmented MLS points, and the green cylinder shows the optimal fit modeled primitive.

cylinder (shift component Z) is left as a free parameter and the horizontal location of the model is estimated at the mean height of every point cloud to reduce shift-rotation correlations. Because of uncertainties in the lidar measurements and mis-segmented points from PointNet, we embed a RANSAC algorithm to improve the robustness of the least squares fitting. The RANSAC function is initialized with mean and principal directions of the point clouds for shift and rotational components. Final modeling results are estimated through a least squares adjustment using the optimum RANSAC parameters and estimated inlier points. Figure 4.5 shows an example of the adjustment results.

Results from RANSAC and the least squares adjustments are cylindrical primitives of the fence posts with geometry characterized by the posts central locations and orientations. Propagation along the cylinder axis gives intersections of the posts with the ground. Using ground points segmented from PointNet, intersections are extracted. Corresponding intersections before and after the deformation are clustered and differenced to estimate ground displacement between the two MLS surveys.

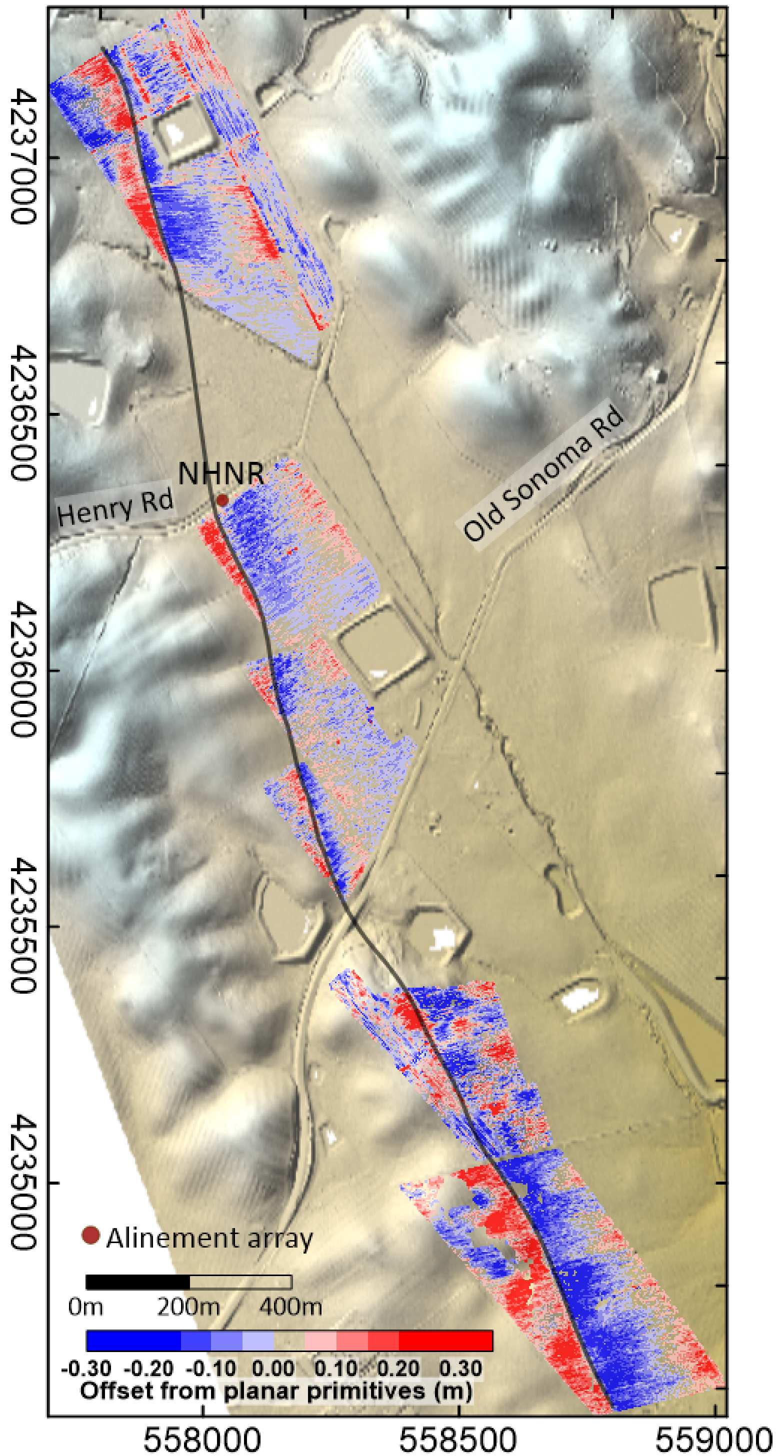

Figure 4.6 Minimal co-seismic offsets approximated by the deviations from planar primitives. Relief base map is generated from airborne laser scanning (ALS) data [19].

4.4 Detection of earthquake-related surface displacements

Using the planar and cylindrical primitives, the surface displacement field of the fault is determined. Minimal co-seismic offset is estimated by quantifying the vine row deformation from the first MLS survey by calculating deviations from a planar primitive. post-seismic deformation is estimated by tracking cylindrical primitives and their ground intersections between the two MLS surveys.

4.4.1 co-seismic response detection

Figure 4.6 displays minimal co-seismic offset detected using planar primitives. Dextral displacement magnitude is color-coded as the deviation from each planar primitive. Right-lateral motion of the fault is characterized by the consistent red to blue color change across the fault. The fault trace is estimated by mapping the transition from red to blue for every planar primitive where a consistent strike, expanding north-south, can be modeled by connecting adjacent transitions throughout the surveyed area. This fault trace approximates the surface projection of the fault. Given the intersections where the fault trace traverses planar primitives, a digital fault trace (black line in Figure 4.6) is estimated using robust local linear regression (LOWESS) [118]. This fault trace is piecewise linear due to the regression model. Employing this derived digital fault trace, statistics for off-fault directions can be calculated. Field measurements of co-seismic displacements are available at the fault crossing of Henry Road [119, 120], and alignment array measurements of post-seismic surface displacements are available at station NHNR [11] for validation of the change detection results.

Modeling the digital fault trace serves as a good supplement for field reconnaissance of the fault ground rupture given that (a) on site surveys of ground ruptures can be localized and inconsistent over kilometer scales. An earthquake and its induced geo-hazards

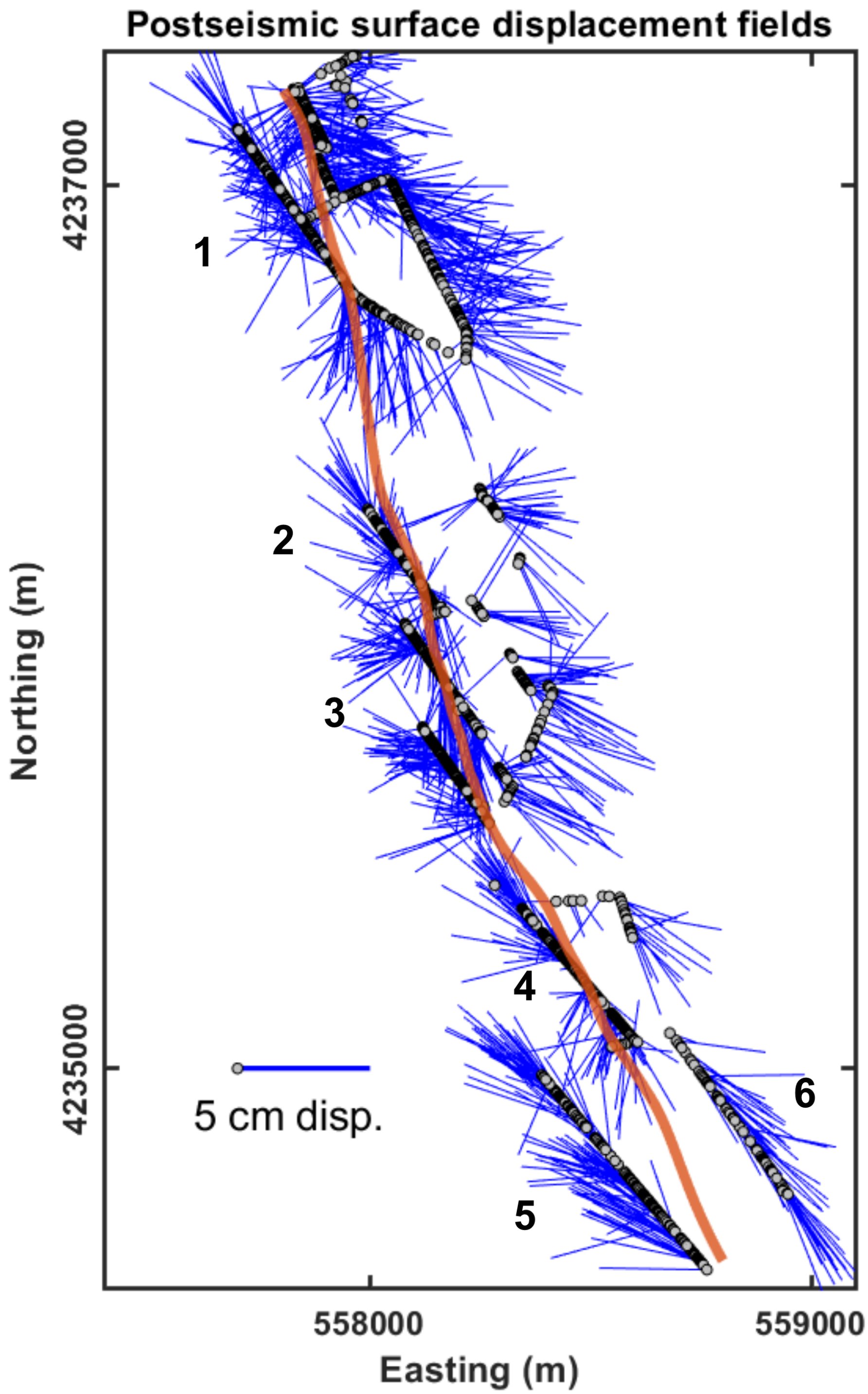

Figure 4.7 Post-seismic surface displacement fields detected using cylindrical primitives. Orange solid line shows the fault trace. Surveyed area is subdivided with numbers indicating areas of study for upcoming analyses.

may limit the access to zones of deformation along the surface faulting, and important displacement signatures could be missed by a field survey if the displacement is not associated with significant cultural feature damage [54, 55, 120]. (b) the slip front of the fault can be buried without reaching the surface and expressed by insignificant ground displacement or scattered ground cracks instead of obvious ground ruptures [5, 6]. This method estimates the fault trace from redundant primitive measurements throughout the area; therefore, the estimated fault trace is less vulnerable to local anomalies and more consistent spatially. The automated process also has the potential for delivering a ground rupture map in a timely manner post earthquake.

4.4.2 post-seismic surface displacement detection

Figure 4.7 shows the horizontal displacement of cylindrical primitives in between the two MLS surveys. Each line on the map represents the path of displacement for a single post tracked at its ground intersection. Tracking more than 2600 cylindrical primitives' displacements, post-seismic surface displacement fields in the near field are revealed. The pin arrowhead depicts the location of detection where the length and orientation of each arrow represents the amount and direction of post-seismic surface displacement. The detected displacement field quantifies the surface displacement between Sep 1st and Sep 30th, 2014 which are 7 and 34 days after the mainshock. Local shear patterns are found where the fault trace crosses between successive posts (Figure 4.8, Figure 4.9 a-d).

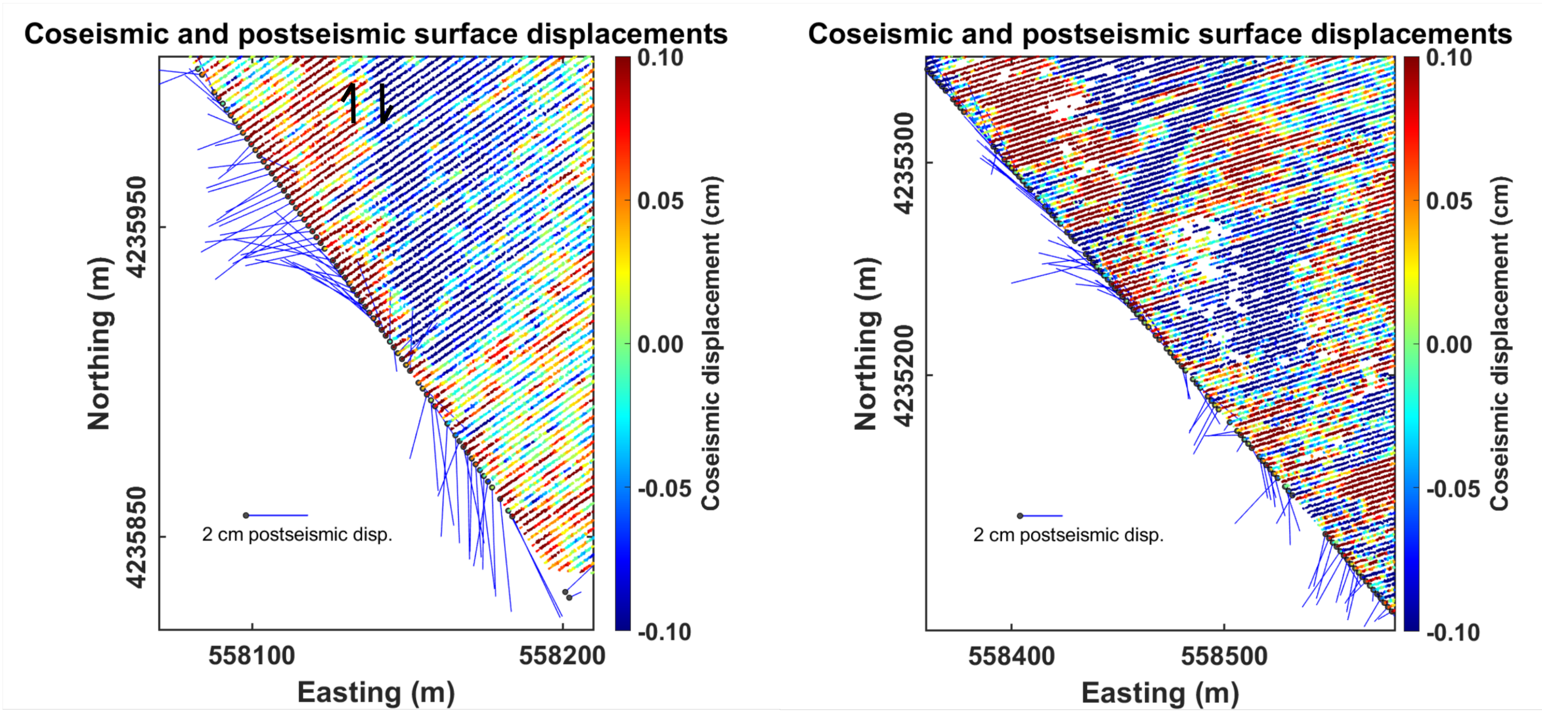

(a) (b)

Figure 4.8 Overlap of planar residuals and post-seismic change detection results (a, b) for study areas 3 and 4 in Figure 4.7.

Collocated with the planar residual approximation to co-seismic response, Figure 4.8 shows the consistency of the detection results using two kinds of geometric primitives. Planar primitives tracking co-seismic response and cylindrical primitives estimating post-seismic surface displacements are collocated at the fault trace, which validates the location of the ground rupture. Planar residuals are color-coded by magnitude of minimal co-seismic offsets; the symbol of strike-slip indicates the location of the fault trace. The pin arrows depict the post-seismic displacements detected using cylindrical primitives where the length and orientation of each arrow represents the amount and direction of post-seismic surface displacement. (a) The red-blue margin delineates the co-seismic fault trace; the distributed arrows localize the post-seismic fault crossing. Inflection points from the detected minimal co-seismic offset are collocated with the change in arrow directions where adjacent arrows change direction dramatically. This confirms the consistency of the change detection results as the transition in both co-seismic and post-seismic displacements are collocated. While the planar primitives can only provide 1D displacement as deviations from straight vine rows, the cylindrical primitives provide 2D displacement vectors showing local deformation in the near field.

Subtle post-seismic surface displacement fields are revealed from changes detected using cylindrical primitives. Figure 4.9 shows six local displacement patterns. Subplots a-d show local shear patterns where the fault trace crosses a line of successive posts. The lines represent vine row post displacements from Sep 1st to Sep 30th. To track how linear features on the ground are deformed by the fault, adjacent posts are connected by local regression lines. Each node of the line represents a post's location at that epoch and the curvature of the line represents nonlinear local deformation induced by shear. Local shear patterns are found in those cases characterized by the transition of surface displacement directions and entangled pre- and post-deformation regression lines. Spinning patterns are found where the fault trace traverses lines of posts.

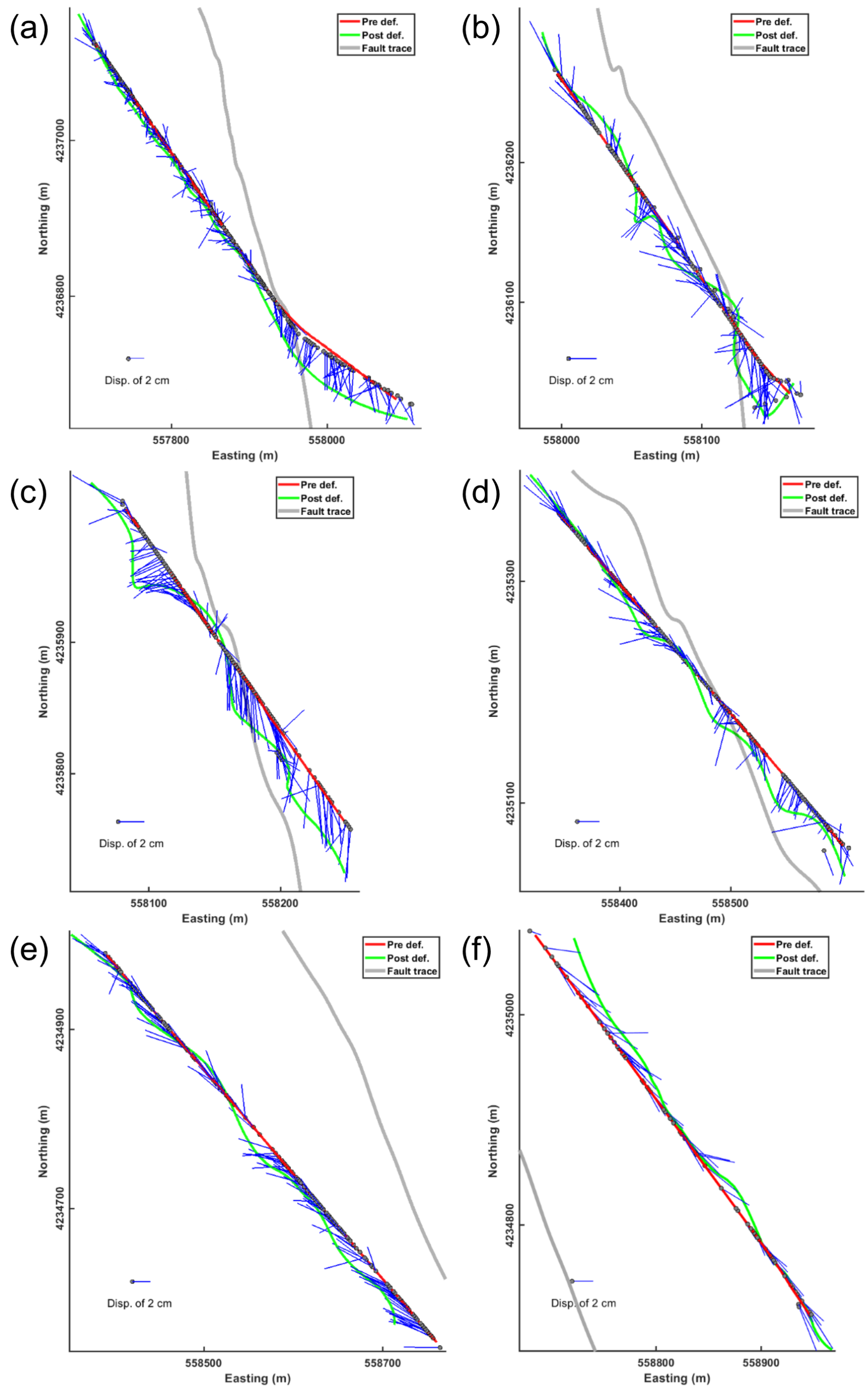

Figure 4.9 Post-seismic surface displacement patterns for the six study areas numbered in Figure 4.7 (1-6 as a-f). Red and green lines represent regression lines of vineyard post locations captured by MLS surveys 7 and 34 days after the earthquake.

Constant strike-slip displacements are observed at posts located on either side of the fault, shown in cases 5 and 6 in Figure 4.9 e and f. The displacements show little variation in direction and scale. The isotropic displacement patterns for cases 5 and 6 indicate little or no off-fault deformation at these locations.

4.5 Interpretations and discussion

Compared with previous geodetic change detection results, the proposed strategy successfully reveals the 2D near field horizontal deformation for the 2014 South Napa earthquake. Though focused on sensing horizontal components, cylindrical primitive-based change detection can also reveal 3D deformation where vertical components are derived by differencing the intersections of the primitives with the ground. However, the estimated vertical component does not benefit from the redundancy of the cylindrical model, and thus the uncertainty of the vertical component directly depends upon the vertical point cloud accuracy. It is challenging to model the top and bottom face of a cylindrical post given poor data coverage from the sideways field of view of a mobile platform. Considering the dextral displacement pattern, we only provided horizontal components of our change detection results.

4.5.1 Continuity analysis of the rupture zone

Continuous vine row curvature over the region indicates that the principle rupture remains buried under the ground, whereas a constant dislocation discontinuity at the surface would indicate that either the fault front reached the ground surface or a secondary fault zone exists. Figure 4.10 shows a zoomed-in map of the planar expression of co-seismic response with color-coded planar residual magnitude. The color at the fault trace changes smoothly, indicating no discrete fault patches exist. Such a continuous displacement pattern is found throughout the surveyed area and is consistent with the analyses that the fault rupture remained buried. The smooth intersection reflects the characteristics of a fault trace where surface displacements are comprised of en echelon sheared extensional fractures

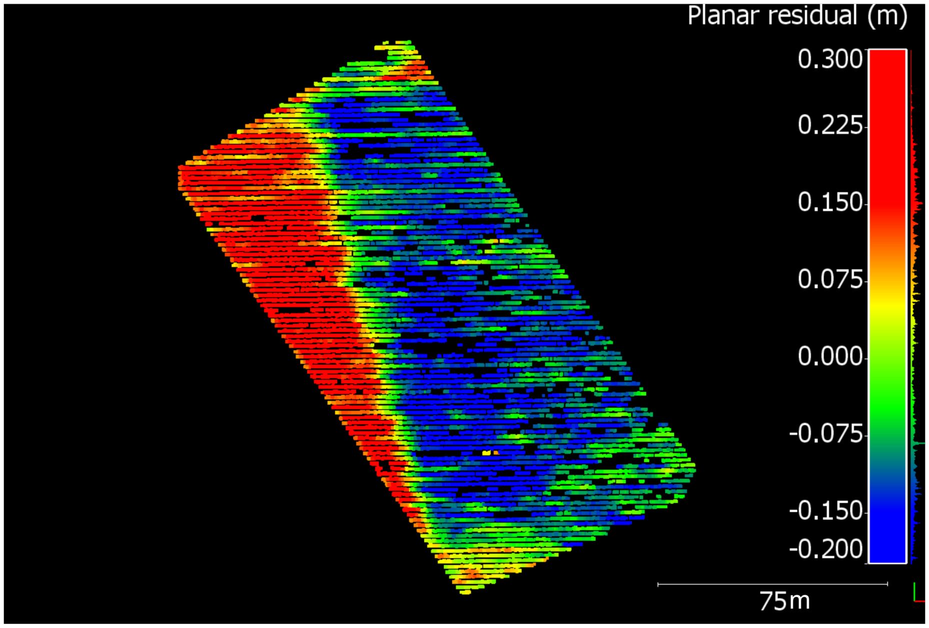

Figure 4.10 Zoomed-in plot of planar residuals which approximate minimal co-seismic offset at the fault trace. Color changes smoothly over the fault trace.

and linear 'mole tracks'. This pattern is consistent with in situ measurements from [53], and [111], and shallow fault slip modeling presented in [6] and [5].

4.5.2 Distributions of deformation versus off-fault distance

post-seismic surface displacement distribution versus off-fault distance provides evidence highlighting non-brittle deformation within the detected changes. The metric for off-fault distance is calculated as the perpendicular distance from observation locations to the closest linear fault trace segment estimated using the planar primitives. Because the posts are anchored at various distances from the fault trace, off-fault distances are spread out uniformly across the rupture zone. post-seismic surface displacements are projected along the fault trace direction as fault parallel displacements. Off-fault deformation is expressed as the profile of fault parallel displacements.

Figure 4.11 shows the results where fault parallel displacements and post-seismic displacement directions are distributed over a range of off-fault distances. The fault parallel component is determined from the strike of the nearest fault section using the fault trace

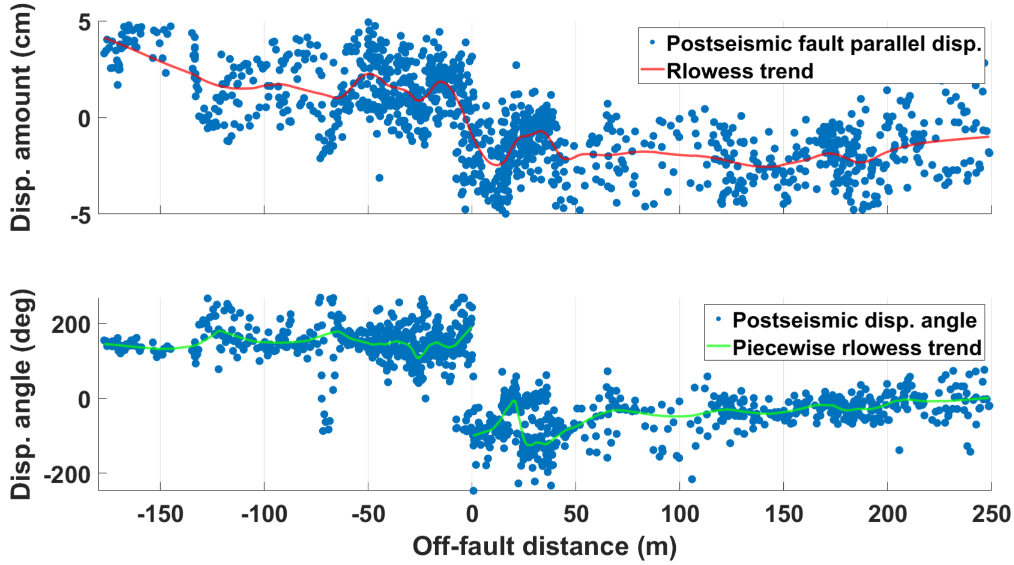

Figure 4.11 Off-fault distributions of post-seismic surface displacements. Components of post-seismic fault parallel displacements (a) and displacement directions (b) are plotted versus off-fault distance.

shown in Figure 4.6. Non-parametric robust local linear regression trends was used to highlight the displacement distribution pattern without introducing assumptions for local fault mechanics. The dextral pattern is obvious in the displacement angle plot where two dominant sliding directions are identified as $-51.33°$ and $145.51°$ from the East. Angular variances are larger close to the estimated fault trace and smaller further away. The dextral pattern is also confirmed by the displacement magnitude transition at the fault trace.

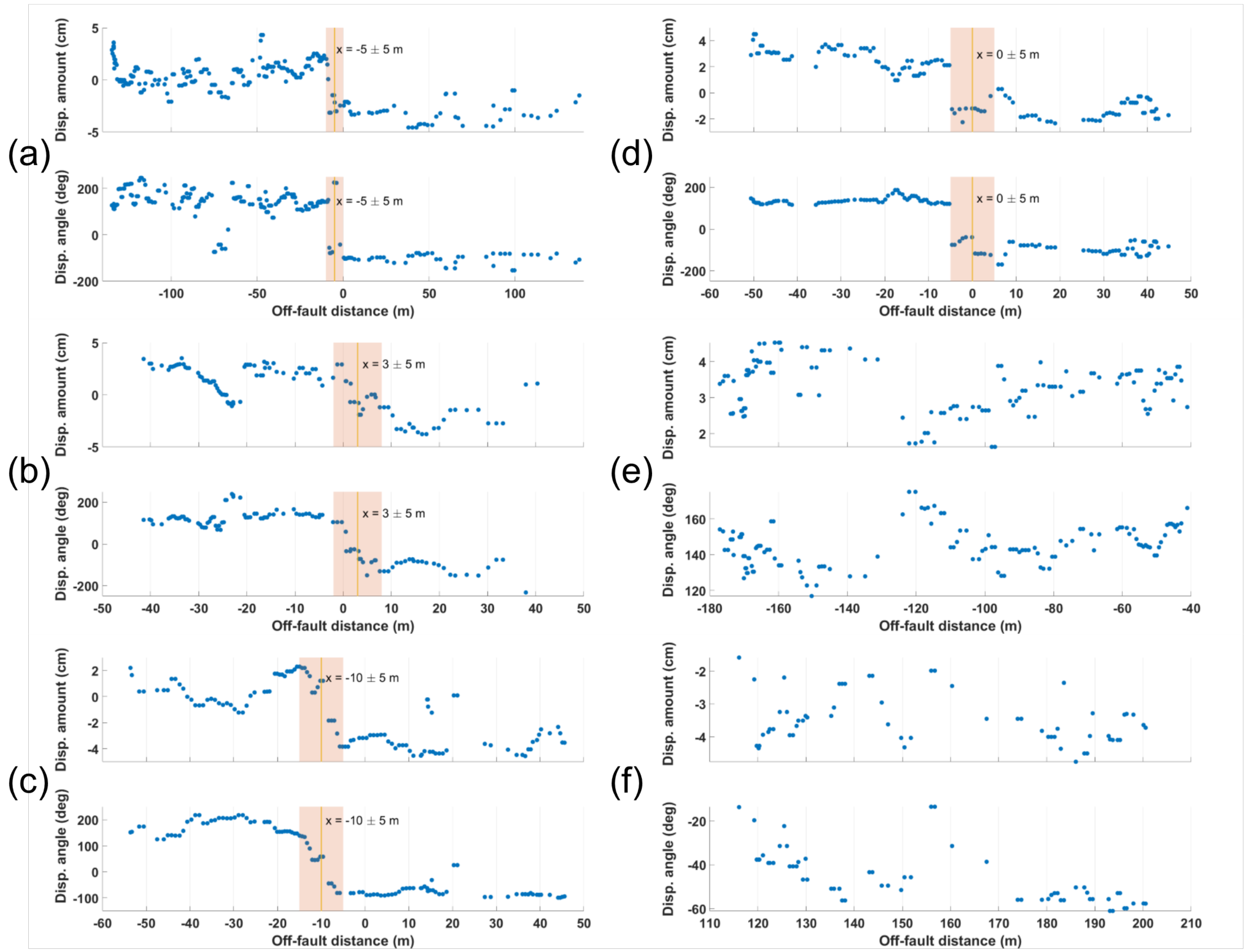

Figure 4.12 Off-fault distributions of post-seismic displacements for the six study areas in Figure 4.7 (case 1-6 as a-f).

Figure 4.12 shows the same off-fault displacement plots for the six study areas corresponding to Figure 4.7. For each case, two distributions are provided: distribution of fault parallel displacements (top) and displacement angle (bottom) plotted versus off-fault distances. The fault parallel component is determined from the strike of the nearest fault section. An $\approx$10 m transition zone is estimated visually at the fault crossing for areas 1-4.

Areas 1-4 (Figure 4.12 a-d) show about 3 cm of off-fault deformation within approximately 10 m of the fault trace. This 10 m transition zone is estimated visually and highlighted in the figure for the area 1-4 fault crossings. The corresponding angular profiles show transition of displacement angles as a result of crossing the fault. Cases 5 and 6 (Figure 4.12 e, f) show no sign of off-fault deformation as these profiles do not cross the fault trace and show little variation in displacement magnitude and angle compared with cases 1-4. Table 4.2 shows the corresponding post-seismic fault parallel displacement for each side of the fault outside the transition zone.

Table 4.2 Average post-seismic fault parallel displacements for the six study areas in Figure 4.9, in centimeters (standard deviation in brackets). Displacements for each side of fault do not include 10 m transition zone.

Study area	West of fault	East of fault	Difference
1	0.79 (1.27)	-3.09 (1.00)	3.88 (1.62)
2	1.71 (1.27)	-2.32 (1.34)	4.03 (1.84)
3	0.51 (1.06)	-3.29 (1.22)	3.79 (1.61)
4	2.65 (0.83)	-1.28 (0.74)	3.93 (1.11)
5	- (-)	- (-)	3.29 (0.70)
6	- (-)	- (-)	-3.47 (0.76)

4.5.3 Potential errors within the change detection results

Because both co-seismic and post-seismic surface displacements are calculated as relative changes, the majority of residual systematic errors for the MLS and any geodetic datum biases will not affect the calculated relative deformation. Given that co-seismic and post-seismic surface displacements are resolved from unique data collections after the earthquake, there are no repeat observations of the same event for estimating uncertainty. However, the accuracy of the detection results can be evaluated by (a) comparing co-seismic and post-seismic surface displacements with field observed co-seismic ground displacements and measurements of post-seismic surface displacements at alignment array stations, and (b) by checking the internal consistency of displacements in areas that are believed to share similar deformation patterns. For example, spatially close vineyard rows crossing the fault at a similar angle should show coherent co-seismic displacements distributed off fault; areas far away from the fault trace should show regional dextral post-seismic displacements that are uniform for either side of the fault.

4.5.3.1 Validation with field observations and alignment array measurements

We can validate the accuracy of the detection results with field and alignment array observations collected near the fault crossing at Henry Road (Figure 4.6). Brocher et al., (2015) [119] recorded 40 cm right-lateral offset, rounded to the nearest centimeter, in the field north of Henry Road within two days after the earthquake. The field rupture was observed as a zone of en echelon left-stepping fractures, and approximate uncertainties for measured offsets are around 5 cm. Ponti et al., (2019) [120] recorded 40.9–46 cm strike-slip displacements at the same location using an estimated fault azimuth. They also point out that most of the surface rupture was expressed as disconnected left-stepping en echelon fractures several meters or more in length with measurable dextral displacements. Hudnut et al., (2014) [19], using alignment array post-seismic displacement measurements and AFTER models inferred a 14 cm co-seismic displacement at alignment array station NHNR. Our estimate of the minimal co-seismic offset from the planar primitives is about 25 cm shown in Figure 4.13 which agrees with field measurements at the decimeter level. Our estimation is smaller than [119, 120] because (a) the detected minimal offset could underestimate the true accumulated displacement as explained in Section 4.3.1 (Figure 4.2), (b) estimating fault azimuth in the field might lead to an overestimate of the surface displacement, and (c) we are comparing localized in situ measurements near the fault crossing at Henry Road with a regional average estimated from all vine rows; the field measurement captures the most obvious displacements that can be accessed by an observer, but they are sparse and discontinuous and do not span the MLS survey area. The average may lead to smaller estimates of displacements from the MLS survey compared with localized field measurements which highlight expressions of displacement at single points.

After the earthquake, alignment arrays were installed to monitor the afterslip [11]. We validated our estimated post-seismic surface displacement by comparing the to alignment array station NHNR located on Henry Road (Figure 4.6). Observed accumulated displacement at NHNR was 18.7 ± 0.22 mm on September 1; 57.1 ± 0.26 mm on September 19 and 76.1 mm on October 23 (error not available). Alignment array station NHNR is bounded by study areas 1 and 2 shown in Figure 4.7. Referring to Table 4.2, we estimated 3.88 ± 1.62 cm and 4.03 ± 1.84 cm post-seismic surface accumulated displacement between September 1 and September 28. For the same time span, the estimated displacement at NHNR is 4.39 cm using alignment array observations and the AFTER program [121–123], which agrees at the level of 4-5 mm with our MLS estimate.

4.5.3.2 Change detection precision

The precision of the change detection results is determined by checking the internal consistency of the estimates. Minimal co-seismic offset was estimated by modeling vine rows as planar primitives. The consistency of the planar deviations can be estimated by checking the coherence of the off-fault distributed deformation pattern. Given that the vine rows cross the fault trace at a similar angle, co-seismic deformation from each vine row should show similar patterns distributed off fault forming a coherent deformation pattern across all vine rows. Figure 4.13 shows the minimal co-seismic offset averaged over 1300 vine rows. The error bars represent the variation of the displacement magnitude within

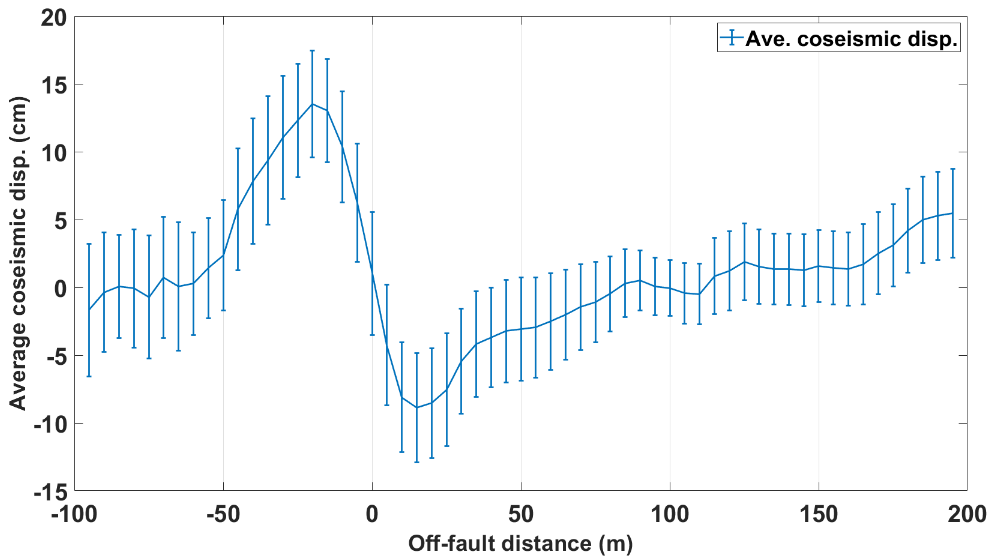

Figure 4.13 Planar residual estimate of minimal co-seismic offset averaged over 1300 vine rows. Error bar indicates local displacement variation within 10 meter bins of off-fault distance.

10 meter windows. The overall scale of the error bar is relatively uniform and slightly decreases off the fault center which indicates a consistent pattern exists across all vine rows and complex deformation patterns exist near the fault trace. The error bars vary in size from 2 to 5 cm across the region. Note that variation of this pattern across different vine rows could also be due to partial occlusions in the lidar point clouds. The uneven vegetation growth along each vine row may bias the planar primitives and the occlusions of a lidar scan may result in incomplete planar primitives extracted from point clouds. Therefore, further field reconnaissance measurements would be helpful to determine probable sources of this variation and better quantify the accuracy of the co-seismic offsets from MLS.

The uncertainties in the estimated post-seismic surface displacements are evaluated by checking the consistency of observations located off the fault trace. Given the assumption that displacements further from the trace should be smoother and more locally coherent, the variation of the displacement detected in the far-field can serve as a good estimate of consistency. Referring to Figure 4.9 e and f and Table 4.2, detected displacements for areas

5 and 6, with vine row posts on only one side of the fault, show a standard deviation of about 7 mm. Given that the methodology is consistent for all posts, we expect a similar level of precision (subcentimeter) for changes detected using cylinder primitives. The other cases (area 1-4) have larger displacement variation due to more complex deformation patterns captured near field, but still only show 10 to 15 mm of variation.

co-seismic and post-seismic surface displacement detection results using planar and cylindrical primitives show internal consistency. Their off-fault displacement distribution also indicates a consistent ground deformation zone. Although the observed minimal co-seismic offset has a larger magnitude in comparison with post-seismic displacements observed between 7 and 34 days after the earthquake, they both show a maximum displacement approximately 25 m off the estimated fault trace (Figure 4.13 and Figure 4.11 a). These coherent detection results confirm the consistency of the deformation estimates after the earthquake.

4.6 Conclusion and future work

In this paper, we developed a method of using automatically extracted geometric primitives to detect changes in the near field of an earthquake. Geometric primitives are shown to be an efficient representation of MLS point clouds for subtle change detection. A change detection workflow was developed relying on PointNet, RANSAC, and least squares cylinder fitting for geometric primitives modeling.

The methodology described successfully recovers the dextral deformation field of the 2014 M_w 6.0 South Napa earthquake. 25 cm co-seismic offsets and 3-4 cm post-seismic displacements are revealed with decimeter and centimeter level precision respectively over a study site three kilometers long. The fault trace is revealed using planar primitives, and local shear patterns are found from the post-seismic displacement distribution detected using the cylindrical primitives. Dextral deformation distributions versus off-fault distances are summarized and off-fault deformation is detected. Results are validated comparing to field and alignment array observations, which show decimeter level agreement with field observations of co-seismic offset, and sub-centimeter level agreement with post-seismic displacement at an alignment array station.

The proposed primitive-based change detection strategy can be generalized as a framework for geological change detection. A project on aseismic fault creep detection using persistent urban geodeteic markers is in progress. For future work, we plan to augment our change detection strategy using more generic geometric primitives and consider the addition of other high definition surveying observations into the methodological framework.

Chapter 5

Monitoring aseismic fault creep using persistent urban geodetic markers generated from mobile laser scanning

This chapter is a modified version of the following peer reviewed journal paper: Xinxiang Zhu, Craig L Glennie, Benjamin A Brooks, and Todd L Ericksen. Monitoring aseismic fault creep using persistent urban geodetic markers generated from mobile laser scanning. *ISPRS Open Journal of Photogrammetry and Remote Sensing*, 2:100009, 2021.

5.1 Introduction

Monitoring of aseismic fault creep is important for seismic hazard assessment. Measurements of fault creep displacements can be used to infer locked sections of a fault system which is thought to correspond to the moment magnitude of a seismic event [32, 59]. Given the slow-moving characteristics of creep events, surface fault creep monitoring requires the detection of small deformations of the ground surface. Measurements such as creepmeters and static GPS observations over time are commonly used as they can resolve centimeter-level creep rates over temporally spaced observations [124]. However, the spatial coverage of these measurements is limited due to the sparse observation network, and the resulting inadequate number of geodetic observations preclude the use of geomechanical models to accurately infer subsurface fault slip and deformation near the Earth's surface (e.g. at infrastructure depths) [5, 6]. Mechanically-based modeling of fault creep requires dense near-field observations of surface displacements with broad spatial coverage and high accuracy.

New high-definition photogrammetric and remote sensing surveying techniques like light detection and ranging (lidar), interferometric synthetic aperture radar (InSAR) and uninhabited aerial vehicle synthetic aperture radar (UAVSAR) have recently made it possible to estimate densely distributed ground displacements for the detection of fault dynamics. However, with increased resolution comes complex and irregular formats and measurements with varying accuracy that bring new challenges for change detection, especially in the near field. As a common method of measuring far-field fault displacement, InSAR provides displacement observations with millimeter to centimeter-level accuracy in the far field of the fault ($>$ 1 km distance) [40, 41, 44, 45, 101, 125]. Phase interferometry is highly efficient for observing temporally spaced estimates of deformation in the phase domain, and thus changes can be detected at the millimeter level. However, interferograms tend to decorrelate with spatial change larger than the carrier wavelength and are therefore vulnerable to large displacements and complex textures (e.g. vegetation) found within the near field. This makes InSAR change detection reliable only in the far field [13, 40, 44].

Compared with InSAR, lidar has observational flexibility in the near field even in urban or vegetated areas [13, 46]. Many applications use the iterative closest point method (ICP) and its variants as change detection strategies to reveal fault-related ground displacements [43, 47, 48, 104]. However, ICP is incapable of resolving gradual centimeter-level changes [12] and suffers from higher estimate uncertainties near the fault trace due to the assumption of localized rigid movement [48]. These methods cannot be used for estimating fault creep, unless the time horizon between the temporal datasets is large enough to overcome the decimeter-level noise (e.g. Scott et al. [47]).

There is a paucity of techniques that can provide distributed high accuracy near-field observations over shorter time scales. At the Hayward fault, for example, the slowly creeping characteristics of the fault (a few millimeters per year [124]) have been recorded by alinement array stations and reported annually for decades, but it has not been captured with high spatial resolution. For InSAR, the complex displacement leads to decorrelation that limits the ability to estimate temporally spaced deformation in the phase domain. For lidar, even with high point density, the irregular format of point clouds makes it hard to identify and associate corresponding points that provide consistent estimates of displacement at the point cloud level. Unlike persistent scatterers within an interferogram [126, 127], point cloud based change detection has the flexibility of sensing near-field deformation but the method does not ensure a stable tracking of corresponding features between epochs, and as a result, the application suffers from a matching uncertainty in addition to the errors in the point observations. Therefore, it would be advantageous to develop new methodology for point clouds which include the identification and tracking of geometric features analogous to InSAR persistent scatterers such that reliable geodetic markers can be identified from point clouds and used for change detection in the near field.

In this paper, we propose a change detection strategy using mobile laser scanning (MLS) point clouds that takes advantage of both the steady and gradual movement patterns of the fault creep and the presence of geodetic markers in an urban environment. The method is able to detect distributed fault creep in the near field within approximately 300 m of the fault trace. Fault creep is detected with meter-level resolution and sub-centimeter level accuracy. The proposed method consists of two major parts: (1) a random sample consensus (RANSAC)-based corresponding plane detector, and (2) a combined least squares displacement estimator. The proposed RANSAC-based corresponding plane detector is designed to seek corresponding planar primitives as stable geodetic markers from repeated and temporally spaced MLS scans such that the point clouds representing the same planar objects are segmented together in each epoch of the MLS scan. The nature of the slowly creeping deformation is leveraged for the detector to assign robust correspondence of planar primitives in each MLS dataset. The method is designed to compensate for the incomplete geometrical representation of point clouds due to scan occlusions [97], and multiple model fitting problems [128] within point cloud-based change detection.

A combined least squares-based displacement estimator is implemented using the temporally spaced groups of corresponding planar primitives. The adjustment is inspired by the airborne laser scanning (ALS) bore-sight self-calibration model proposed by Skaloud and Lichti [129]. Our previous study [130] shows that geometric primitive-based change detection using MLS data has the ability to capture centimeter-scale deformation in the fault near field. This work highlights the potential and advantages of augmenting MLS point clouds as geometric primitives for accurate change detection. Point clouds modeled as primitives provide a localization accuracy that is better than the individual lidar point noise [130]. A similar combined least squares adjustment was also implemented by Kusari et al. [49] where they showed the method works on large blocks of lidar data. However, the method they proposed is not flexible and robust enough to recover subtle deformation at a resolution finer than the block scale; this makes it insensitive to near-field nonlinear shear displacement patterns (e.g. Chinnery [131]). In this paper, the use of planar primitives (as geodetic markers) captured from temporally spaced MLS surveys is presented to estimate high accuracy and resolution near-field deformation. Compared with previous work, rather than estimating primitive geometry and ground change separately, the proposed least squares adjustment combines the estimates of displacements with the estimates of primitive geometry, leveraging the additional geometric constraints for estimation of the displacements. The method is able to accurately capture centimeter-level ground deformation and simultaneously estimate primitive geometry thanks to the high degrees of freedom created using planar primitives. The methods are tested on MLS data collected along a 2 km segment of the Hayward fault in 2015 and 2017. The accuracy of the results are validated by the collocated alinement array measurements and fault creep patterns are revealed as displacement fields in the near field of the fault.

The rest of this paper is organized as follows: first the MLS surveys conducted at the Hayward fault are described; then the two-module change detection method is introduced and how the method takes advantage of the characteristics of slow-moving fault creep is demonstrated. Change detection results are then shown and validated with theodolite surveys on collocated alinement arrays. The strength of the regression solutions is then discussed followed by assessments of the change detection strategy.

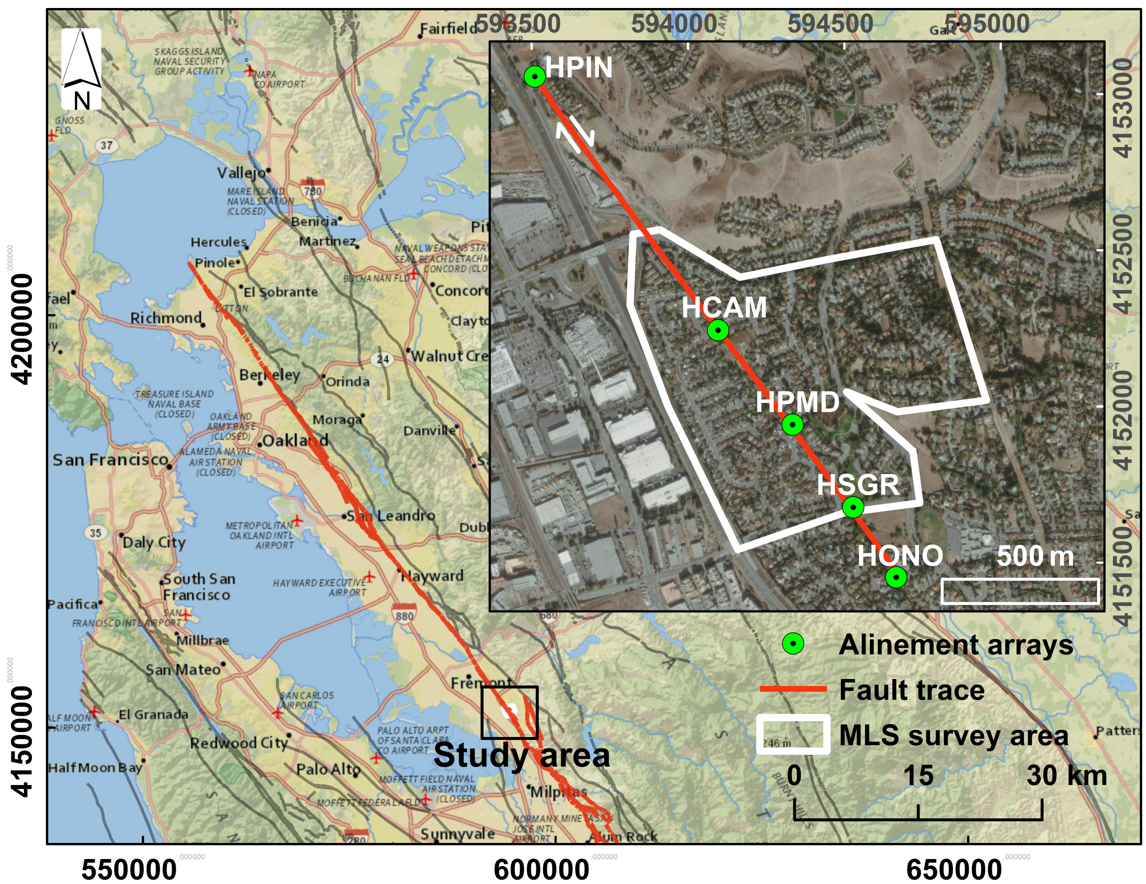

Figure 5.1 Maps of the study area. The white polygon outlines the MLS survey extents. The Hayward fault trace is highlighted by the red line and the green dots indicates the alinement stations.

5.2 MLS data collection and the Hayward fault

The Hayward fault is known for its active aseismic surface creep and long-timescale geodetic records. Long-term creep rates have been recorded using theodolite surveys since 2001 by the USGS in collaboration with the Geosciences department at SFSU [10]. According to their report [124], steady creep rates have been recorded within the MLS surveyed area (Figure 5.1). The creep rate at alinement array station HCAM located at Camellia Drive has averaged $\sim$7 mm per year over the past 10 years. Similar creep rates have been recorded at adjacent stations HPMD, HSGR, HONO and HPIN (380 m, 720 m, 980 m and 1000 m from HCAM respectively). Although HPIN and HONO are located outside the survey area, they provide a reliable bound of the creep rates for the MLS survey area. These alinement array measurements outline a steady and gradual dextral slip pattern for the monitored fault creep. Figure 5.2 shows accumulated creep observed since 2010 as dextral displacement at these alinement array stations.

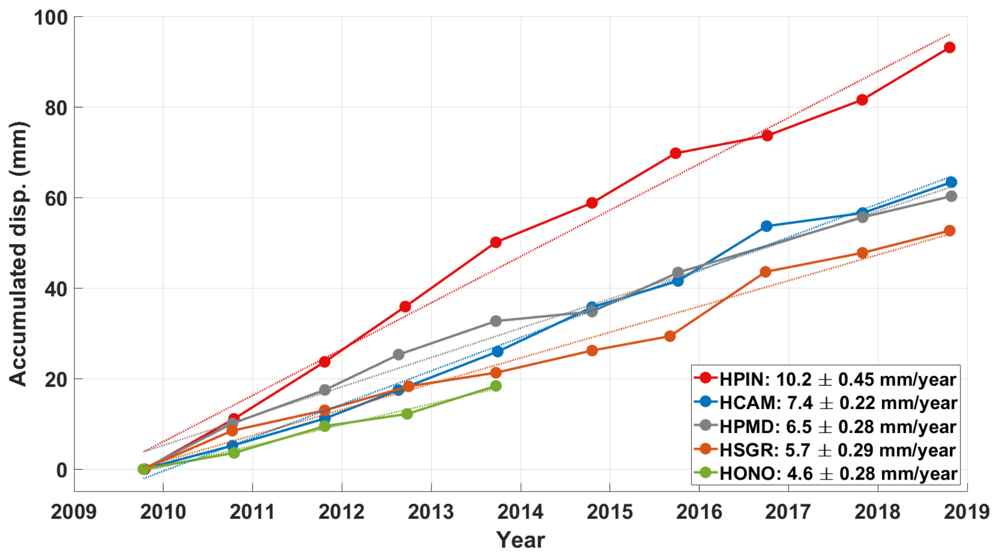

Figure 5.2 Accumulated displacement at alinement array stations since 2010.

The MLS surveys were conducted in July of 2015 and again in June of 2017 near Fremont, CA, along a 2 km segment of the Hayward fault. The survey area is shown in Figure 5.1. Two RIEGL VZ-1000 scanners mounted on a pickup truck were used to collect the MLS data with a point density of approximately 300 points/m^2 at a distance of 20 m from the scanner. Multiple Global Navigation Satellite System (GNSS) base stations were used for data acquisition and all GNSS, Inertial Navigation System (INS) and laser scanning data was time-tagged and recorded for post-mission analysis with the same survey platform described in Brooks et al. [6]. GNSS/INS data was post processed using Grafnav software in tightly coupled mode. The survey area was primarily devoid of significant vegetation and therefore there was minimal loss of GNSS lock and a comparison of independent forward and reverse GNSS solutions agreed at the centimeter level. Each roadway in the survey area was driven multiple times to minimize occlusions, enable precise boresighting of the laser scanners and provide an internal consistency check for the MLS point clouds. The boresighting was undertaken using a methodology similar to that presented in Skaloud and Lichti [129]. Planar residuals from the boresighting process were examined to ensure that there were no systematic errors present in the MLS trajectory – in general the RMSE for all planes after boresight adjustment were less than 10 mm. Finally, after boresight adjustment, the areas of overlap in the MLS point cloud were examined to identify any areas with remaining systematic errors by examining vertical profile differences, as the vertical is the weakest component of a GNSS/INS solution. Figure 3 shows a representative profile (10 cm wide by 90 m) along a flat road approximately 10 m from the scanner. Variations in the point cloud profile show an RMSE of the point cloud (including multiple passes) of less than 10 mm. The careful post-processing and analysis of both the 2015 and 2017 datasets allow us to confidently conclude that the relative noise levels of each of the point clouds are below the expected magnitude of the displacement signal due to fault creep.

5.3 Methodology

The proposed change detection is executed in two steps. First, a RANSAC-like scheme is developed to find corresponding planar primitives pre- and post-deformation. Second, a combined least squares displacement estimator is used to calculate fault creep displacements constrained by the geometry of the corresponding planar primitives. Details of each process are elaborated below.

5.3.1 Corr-planar primitives detection

Herein, a planar primitive pre-deformation and its counterpart post-deformation are referred to as the reference and secondary corresponding planar primitives or corr-planar primitives. To find as many corr-planar primitives as possible from repeated MLS observations, we modified the classic RANSAC algorithm [110, 132] that is widely used to extract planar primitives from point clouds. The classic RANSAC detection is improved to run in "parallel" on two or more point clouds collected at the same location with a slightly relaxed consensus threshold for the secondary dataset to compensate for the dislocation induced by motion, in this case, the fault creep. As a result of the creep, a dislocated post-deformation plane is expected to be in a vicinity of the original pre-deformation plane, where the difference between the two is bounded by a relaxed local creep rate estimated from the alinement arrays.

Generally, RANSAC detection of plane features requires four steps: (1) randomly sampling a minimum number of points required to determine the plane, (2) solving for plane parameters given the point samples, (3) calculating the number of inliers for the solved plane with an artificial threshold, and (4) determining if the number of inliers is large enough to justify an update for the plane estimate. To detect corr-planar primitives, the proposed method follows the same steps (1) and (2) performed on the reference point clouds. The improvement lies in the third step where inliers for both the reference and secondary datasets are calculated with a slightly relaxed threshold for the secondary datasets; the plane parameters are only updated when better consensus sets are found in both the reference and secondary sets.

For the modified RANSAC plane detection, both point-to-plane distance and angular deviation to the estimated planes are used as thresholds to calculate the number of inliers. Point-to-plane distances are straightforward to compute, where the normal of each point is estimated by eigendecomposition of its 8-nearest neighbor points as described in the point data abstraction library (PDAL Butler et al. [133]). For the reference set, point-to-plane distances closer than 3 cm with normal deviations smaller than 7° are counted as inliers; for secondary sets, point-to-plane distances closer than 4 cm with normal deviations smaller than 10° are counted as inliers. These thresholds were calculated by considering the beamwidth of the laser footprint [134] and the precision of the plane observations. The

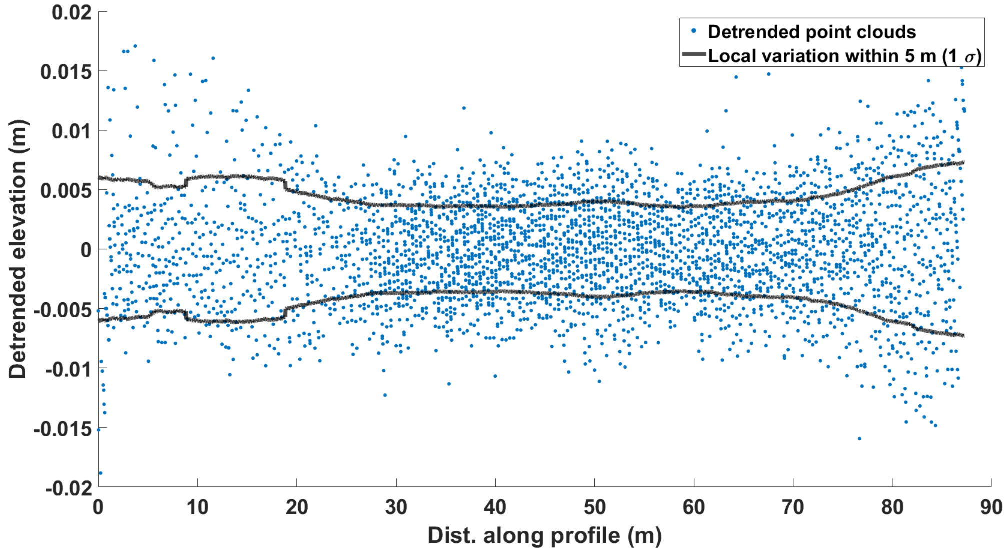

Figure 5.3 Vertical profile of the point cloud (10 cm by 90 m) along a roadway. Elevation variation (1σ) is plotted as a solid line using a 5 m moving window.

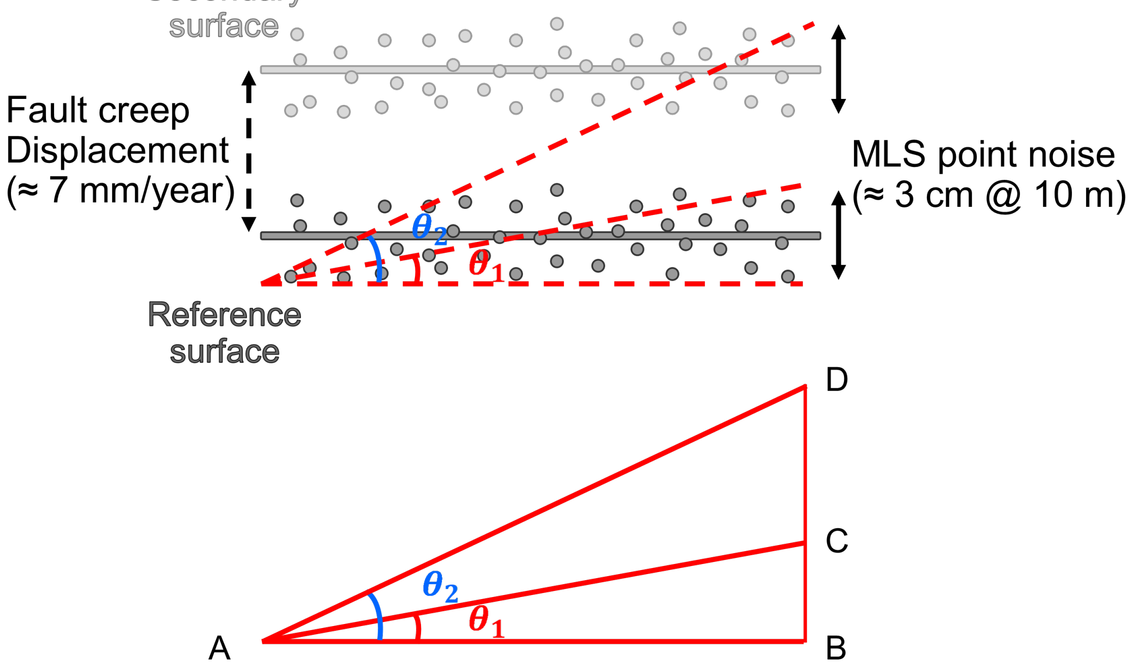

Figure 5.4 Illustration of MLS point cloud noise and selection of RANSAC threshold (displacements are not drawn proportionally in this schematic plot).

VZ-1000 scanner has a beam divergence of 0.3 mrad (i.e. laser footprint has a diameter of 3 cm at 100 m), and the precision of the lidar observed planar surfaces are estimated from the ground profile shown in Figure 5.3. As shown in Figure 5.4, the threshold for a plane $|BC|$ is bounded by the laser point noise estimates of 3 cm for a close range scan (in general < 10 m); distance threshold $|CD|$ is bounded by the creep displacement observed at the alinement array stations, estimated as 1 cm. The normal vector angular threshold (θ_1, θ_2) is bounded by the smallest plane to be considered such that plane size $|AB|$ larger than $(\frac{|BC|}{\tan\theta_1}, \frac{|BD|}{\tan\theta_2})$ can be detected by the RANSAC detector.

In addition to the RANSAC detector, a sequential searching strategy is also implemented such that the detector is embedded in a moving window looping multiple times through the point clouds. This sequential RANSAC is necessary because multiple planes can be present within a search window, and as a result, a single point may be detected as an inlier on multiple planes. This problem is known as multiple models geometric fitting in computer vision [128].

For each round of RANSAC detection, a subsample of reference dataset query points for the search window is selected where the minimal query point spacing is set to be 0.5 m. The window size is chosen to be 20 m (diameter) which is slightly larger than the biggest planar surface detected within the surveyed neighborhood. As the moving window passes over the dataset, at every query position, the largest corr-planar primitives are detected using the corr-planar RANSAC detector while the affiliation of a point (which plane it belongs to), can be reassigned such that the detection is independent of the query sequence. After looping over all query points, point clouds belonging to the largest planes detected at all query locations are removed and a new round of detection is started to identify and remove point clouds for the second-largest corr-planar primitives. The iterations terminate when there are no corr-planar primitives detected.

A flow chart of the modified RANSAC process can be found in Figure 5.5. In this generalized RANSAC detection, the consensus set of a plane consists of all points that are detected as inliers; dually, the preference set of a point consists of all planes that this

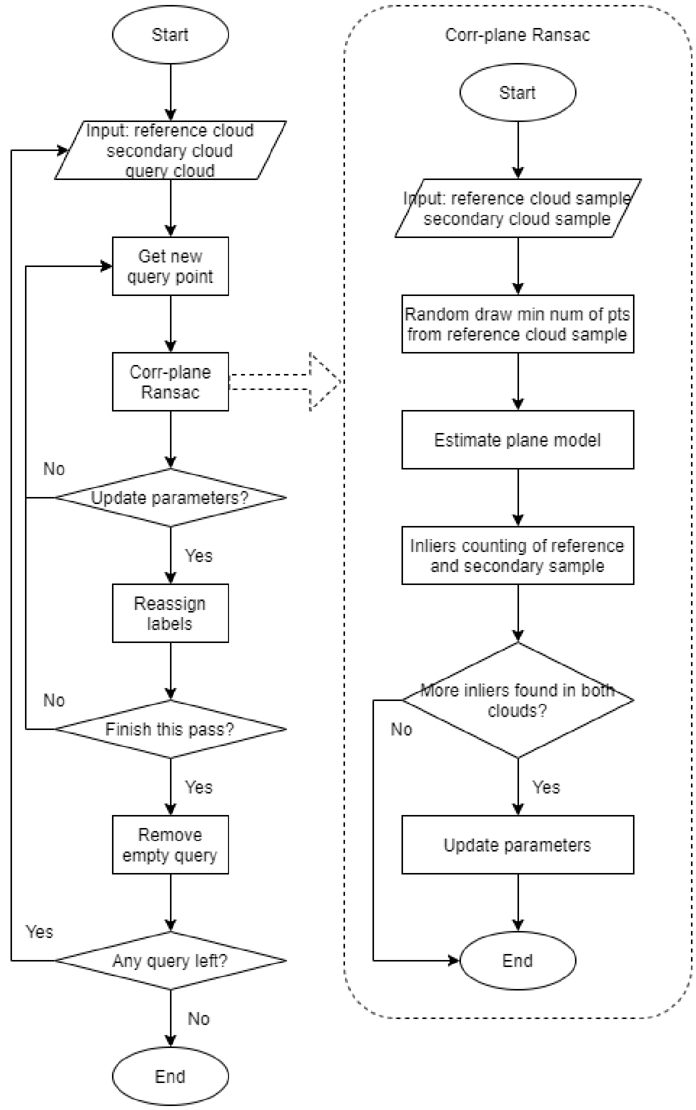

Figure 5.5 Flow chart of the RANSAC corr-plane detection.

point potentially belongs to. The reassignment ensures that the point is assigned to the largest consensus set detected within a single round such that large planar objects like walls and roofs will not be broken into patches due to the moving window search; multiple rounds of detection ensure that multiple corr-planes can be captured as long as they are significant enough to contain a minimum amount of points. For this study the minimum point threshold is set to 150 points. The detector captures approximately 60% of the corr-planar primitives within the first iteration using about 40% of the overall processing time and completes detection in an average of 8 iterations.

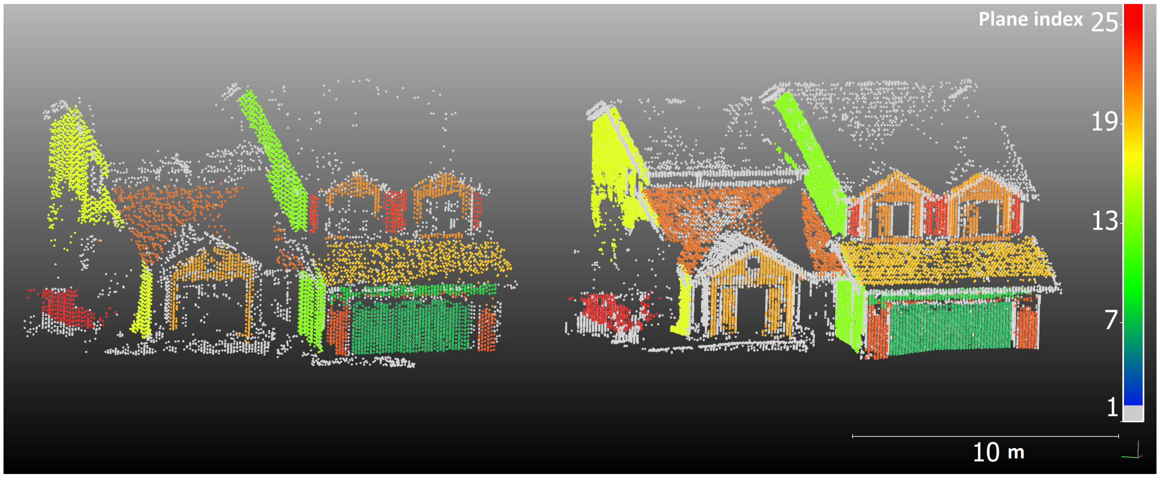

Figure 5.6 A sample corr-planar RANSAC detection showing MLS point clouds of a house captured in 2015 (left) and 2017 (right).

Figure 5.6 demonstrates the detection results of the sequential corr-plane detection. Points are color coded by index of the corr-planar primitives. Grey points indicate unclassified points which represent either inconsistent objects detected due to MLS scan occlusions or planar primitives that are too small (under 150 pts) to be identified. The method robustly detects corr-planar features. The RANSAC scheme overcomes the incomplete representation of planar geometry in point clouds due to scanning occlusions. In addition, planar primitives are only extracted when counterpart planes exist in the paired dataset.

5.3.2 Combined least squares adjustment

Given corr-planar primitives extracted from the MLS data, creep deformation can be estimated by re-aligning the corresponding planes using a least squares framework. For fault creep, the deformation is detected as a relative displacement, i.e. how one side of the fault has moved relative to the other side; therefore, precise absolute georeferencing of the two datasets is unnecessary as long as a relative post-registration is performed.

The temporal displacements are estimated based on a least squares adjustment of rigid body transformations conditioned on the planar shape of the corresponding primitives, which is similar to the boresight self-calibration model presented in [129]. This least squares adjustment estimates the rigid transformation parameters and the plane parameters simultaneously, which is why it is referred to as a combined least squares adjustment. A description of the methods is given below.

For any detected corr-planes, given reference point clouds and transformed secondary point clouds, the geometry of the corr-planes are estimated as

$$f(\boldsymbol{l},\boldsymbol{n},\boldsymbol{x}) = < \begin{bmatrix} n_x \\ n_y \\ n_z \end{bmatrix} \cdot \begin{bmatrix} X \\ Y \\ Z \end{bmatrix} >= 0, \tag{5.1}$$

where $< \cdot >$ represents the dot product of two vectors, and $[X,Y,Z]$ are the coordinates of either the reference or transformed secondary point cloud. Note that both datasets are pre-processed with a constant translation such that the reference point cloud centroid is at the origin.

For secondary point clouds, the rigid transformation assuming small angles ($< 1°$) is defined as

$$\begin{bmatrix} X \\ Y \\ Z \end{bmatrix} = \begin{bmatrix} 1 & -\alpha & \beta \\ \alpha & 1 & -\gamma \\ -\beta & \gamma & 1 \end{bmatrix} \begin{bmatrix} X_s + t_x \\ Y_s + t_y \\ Z_s + t_z \end{bmatrix}. \tag{5.2}$$

Corr-planes are constrained by geometry

$$g(\boldsymbol{n}) = {n_x}^2 + {n_y}^2 + {n_z}^2 - 1 = 0. \tag{5.3}$$

In the above equations

- The observations are $\boldsymbol{l} = [\boldsymbol{l_r};\boldsymbol{l_s}]$
  - reference point clouds $\boldsymbol{l_r} = [X_r, Y_r, Z_r]^T_{obs.}$

- secondary point clouds $\boldsymbol{l_s} = [X_s, Y_s, Z_s]^T_{obs.}$

- The unknowns are **n** and **x**
  - normal directions of corr-planes $\boldsymbol{n} = (n_x, n_y, n_z)$
  - secondary points rigid transformation parameters (3 translations and 3 rotations) $\boldsymbol{x} = (t_x, t_y, t_z, \alpha, \beta, \gamma)$

Given only a single observed plane, the adjustment defined above will be ill-posed because a planar surface is only sensitive to displacement along its normal. To regularize the regression, a group of planes ($\boldsymbol{l_i}$ where i represents plane indices) with varying normal vectors are selected within a query window so that they share a single rigid transformation $\boldsymbol{x}$ in the least squares adjustment. One can visualize this process as the adjustment being implemented on not a single pair of corr-planes but an ensemble consisting of several pairs such that a shared transformation can be estimated and constrained by the geometry of each corr-planar primitive. As long as the augmented planes are not parallel, the geometry of the ensemble is unique enough to ensure a robust regression. By choosing planes randomly within a search radius, the solution's geometry is unique enough to reliably estimate displacement in any direction. The number of planes used for each rigid transformation and the search radius of the query window are empirical parameters that must be chosen based on the density of planar surfaces and their variations in geometry; both of these will be dataset specific. Metrics for selecting the search radius and the number of ensemble planes are discussed in Section 5.3.3.

A combined adjustment (Gauss-Helmert) model [135] is used to estimate the solutions. Linearization of Equation 5.1 and constraint 5.3 takes the form

$$A_1\hat{\delta}_1 + A_2\hat{\delta}_2 + B\hat{v} + w = 0 \tag{5.4}$$

$$\text{and}\, G\hat{\delta}_2 + w_c = v_c, \tag{5.5}$$

where $A_1 = \frac{\partial f}{\partial \boldsymbol{x}}$ and $A_2 = \frac{\partial f}{\partial \boldsymbol{n}}$ are the partial derivative of function f with respect to the unknown transformation and plane parameters, $B = \frac{\partial f}{\partial \boldsymbol{l}}$ is the partial derivative of function f with respect to the observations (laser points), v are the residuals, and w is the misclosure vector, i.e. the value of function f estimated with the estimated parameters and observations. $G = \frac{\partial g}{\partial \boldsymbol{n}}$ is the partial derivative of the constraint g with respect to the unknowns, v_c is the constraint residual vector and w_c is the misclosure vector of the constraints. The adjustment iteratively improves the estimated parameters by the corrections represented by each $\hat{\delta}$, which are the correction vectors for the transformation (1) and plane parameters (2).

Using Lagrange multipliers (λ and μ), Equation 5.4 can be solved with the constraints provided by Equation 5.5. The Lagrange function takes the form

$$\begin{aligned}\phi &= \hat{v}^t P \hat{v} + \hat{v_c}^t P_c \hat{v}_c \\ &\quad + 2\lambda^t (A_1 \hat{\delta}_1 + A_2 \hat{\delta}_2 + B\hat{v} + w) \\ &\quad + 2\mu^t (G\hat{\delta}_2 + w_c - v_c).\end{aligned} \tag{5.6}$$

Here, $P\, and\, P_c$ are the corresponding weight matrices, where the diagonal terms are the inverse variance of the observations and constraints, respectively.

Setting the derivatives of the Lagrange function (Equation 5.6) equal to zero yields the normal equations given as

$$\begin{aligned}&\begin{bmatrix} A_1^T (BP^{-1}B^T)^{-1} A_1 & A_1^T (BP^{-1}B^T)^{-1} A_2 \\ A_2^T (BP^{-1}B^T)^{-1} A_1 & A_2^T (BP^{-1}B^T)^{-1} A_2 + G^T P_c G \end{bmatrix} \begin{bmatrix} \hat{\delta}_1 \\ \hat{\delta}_2 \end{bmatrix} \\ &+ \begin{bmatrix} A_1^T (BP^{-1}B^T)^{-1} w \\ A_2^T (BP^{-1}B^T)^{-1} w + G^T P_c w_c \end{bmatrix} = \begin{bmatrix} 0 \\ 0 \end{bmatrix}.\end{aligned} \tag{5.7}$$

The regression results using Equation 5.7 lead to simultaneous estimates of displacement (creep) together with corr-planar geometry (planar normals).

5.3.3 Distribution of corr-planar primitives and strength of least squares solution

Given that displacement is estimated based on the combination of a group of corr-planes within a defined search window, it is meaningful to explore the impact of the ensemble geometry on the regression results. As mentioned previously, a single pair of corr-planes can only be used to detect a displacement in the direction of the plane normal; to capture displacements in all directions a number of closely located corr-planes must be aggregated such that various normal directions are combined. For this aggregation process, the two hyper-parameters to consider, namely the number of corr-planes and the search radius, are actually correlated as they both reflect a general distribution of corr-planes found within the MLS data. An ideal aggregation should take in as many corr-planes as possible to ensure robust solution geometry but within an area as small as possible to have optimal detection resolution. To optimize aggregation geometry while obtaining the highest resolution, an independent measure of the strength of the least squares solution could be considered. Herein we use an examination of the covariance matrix, similar to the positional dilution of precision (PDOP) metric used in satellite navigation and geomatics engineering [136, 137] to examine the relative geometric strength of the estimated translation.

To calculate the geometric strength of the translation (GSTR), the trace of the unscaled covariance matrix $C_{\boldsymbol{n}}$ of the translation parameters is used given as

$$C_{\boldsymbol{n}} = (A^T A)^{-1} \tag{5.8}$$

$$\text{and}\, GSTR = \operatorname{tr}(C_{\boldsymbol{n}}), \tag{5.9}$$

where A is the Jacobian matrix of Equation 5.1 with respect to estimated translation $[t_x, t_y, t_z]^T$.

GSTR represents the relative strength of the aggregated corr-planes' geometry and is equivalent to PDOP from GNSS processing that evaluates receiver-satellite geometric strength. A larger GSTR corresponds to larger regression uncertainties due to poor geometry (i.e. not a good distribution of planar normals). For example, closely spaced parallel walls and/or roofs could result in large GSTR values indicating weak regression geometry.

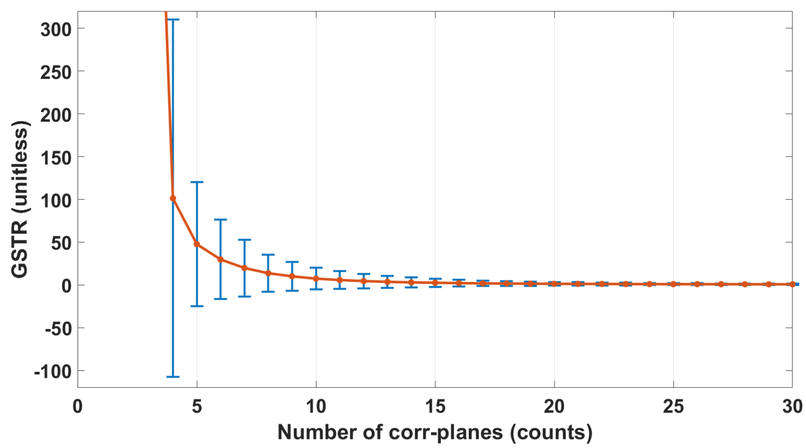

Figure 5.7 Geometric strength of the translation (GSTR) versus the number of corr-planes. Error bars show the variation of the distribution calculated over the entire MLS surveyed area.

Figure 5.7 illustrates the distribution of GSTR versus the number of corr-planes for a selection of the Hayward fault MLS data. In this figure, the curve flattens beyond 10 planes as GSTR falls under 10. A conservative minimum of 12 planes is chosen for the proposed combined least squares adjustment. The associated GSTR value (GSTR ≈ 2) is used to filter out regression results with weak geometry.

5.4 Results and interpretations

5.4.1 Detected fault creep displacement fields

Figure 5.8 shows the fault creep displacement field calculated from MLS point clouds acquired in 2015 and 2017. The head of the pin-shaped vector represents where the displacement is detected, and the length and orientation of the pin represent the offset and direction of displacement. Away from the fault, dextral motions are oriented parallel to

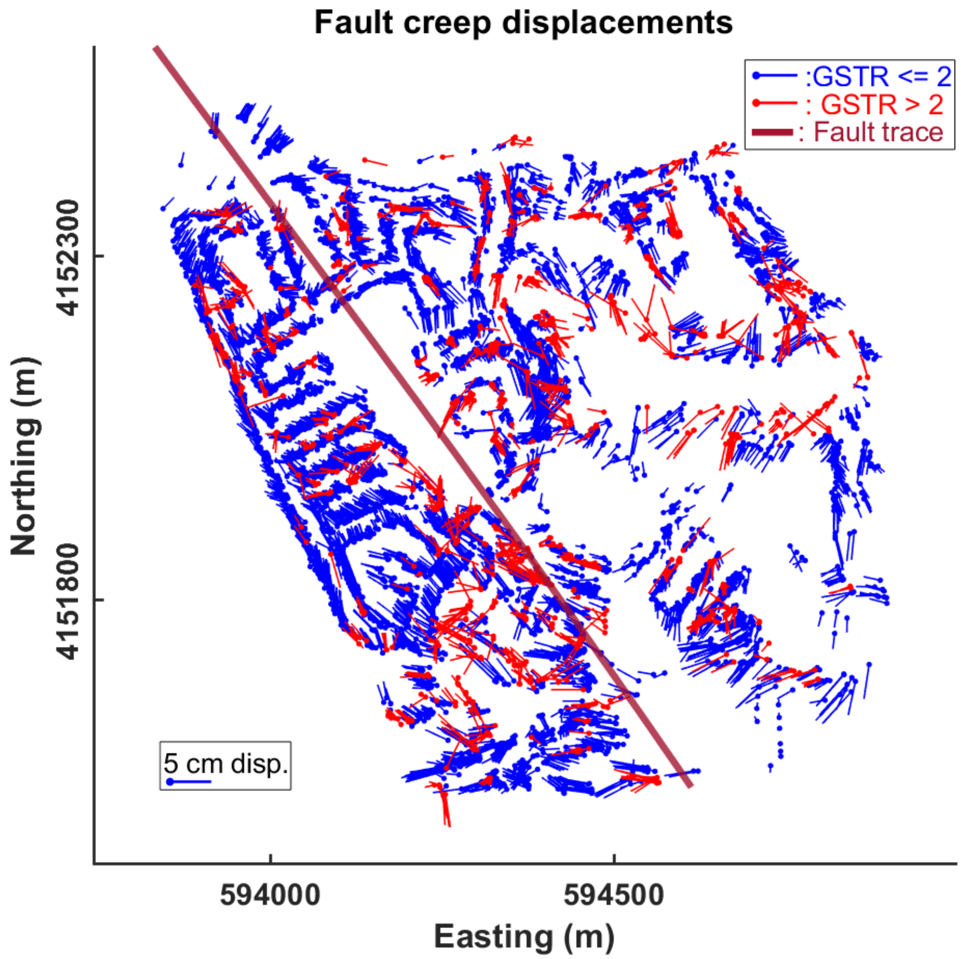

Figure 5.8 Detected fault creep displacement field. The field identified fault trace is plotted as the dark red line. Red and blue vectors indicate displacement regression segmented by GSTR (see Section 5.3.3).

the fault trace. The average displacement is 1.78 ± 0.8 cm which reflects an average creep magnitude, regardless of orientation, over the entire survey area. However, the amount and direction of the creep displacements vary and show spatial correlation with distance to the fault trace. Note that in the figure we have highlighted those solutions with a GSTR > 2 in red. It is quite clear that the solutions with higher GSTR values contain some outliers as evidenced by their anomalous orientations.

The fault trace presented in Figure 5.8 and in subsequent plots is interpolated based on the survey of alinement arrays as documented by McFarland et al. [124] and Galehouse et al. [10]. According to the alinement array surveys, road and curb cracks are used as evidence of the fault location. A connection of these documented cracks over the region is then used as an estimate of the local fault trace. In this study, local crack measurements at alinement array stations HPIN, HCAM, HPMD, HSGR and HONO are considered as they span the MLS survey area, and the fault trace is estimated as a non-parametric linear local regression [138] of the alinement array estimated fault locations. Compared with other records, e.g. Quaternary faults [139], this fault trace estimate has better spatial resolution and therefore enhances examination of off-fault creep displacement distributions.

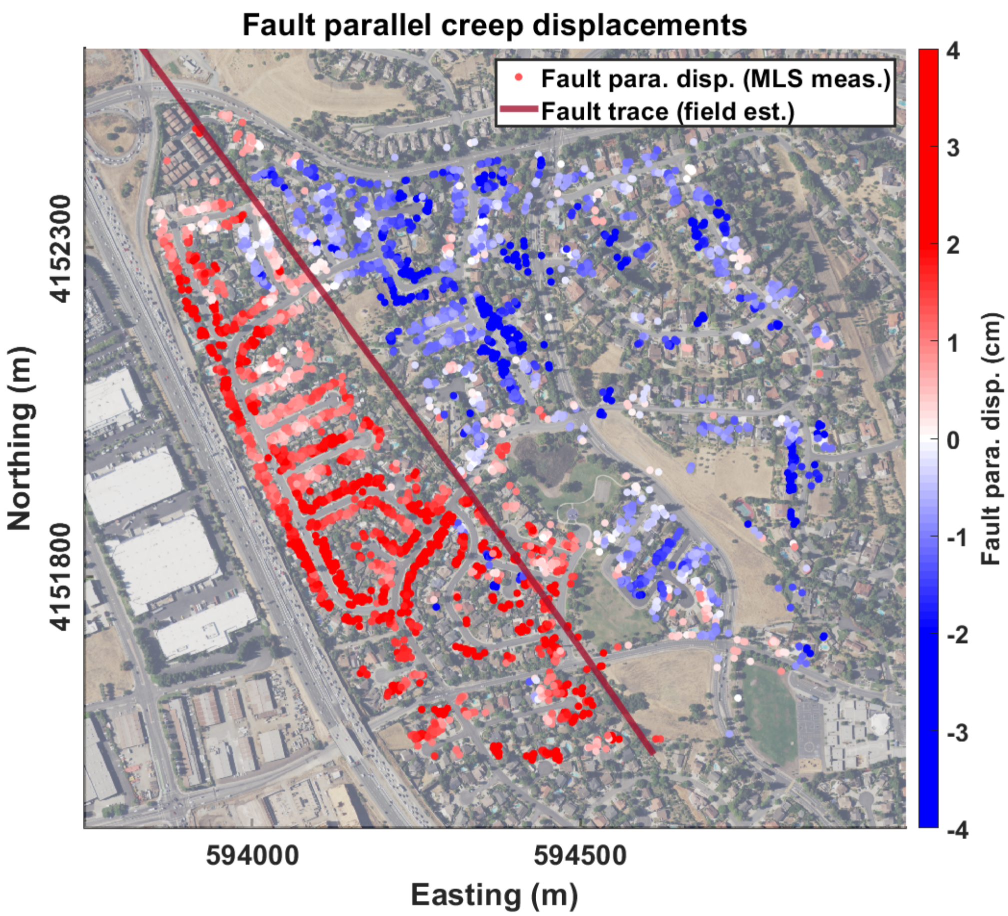

Figure 5.9 Fault parallel creep displacement field. Basemap from NAIP Digital Georectified Image courtesy of the U.S. Geological Survey [20].

5.4.2 Distributions of off-fault creep displacements

Using the displacement field and the fault trace estimate, displacements parallel and perpendicular to the fault can be calculated by projecting the displacement vectors along and across the nearest fault trace direction. Figure 5.9 shows the spatial distribution of the fault parallel creep displacement. Dots show centroids of search window locations for creep colored by the amount of fault parallel displacement. The dark red line indicates the fault trace estimated from the alinement array survey. The amount of displacement varies gradually even near the fault trace. This is consistent with the gradual and steady fault creep displacement characteristics reported by field measurements such as McFarland et al. [124].

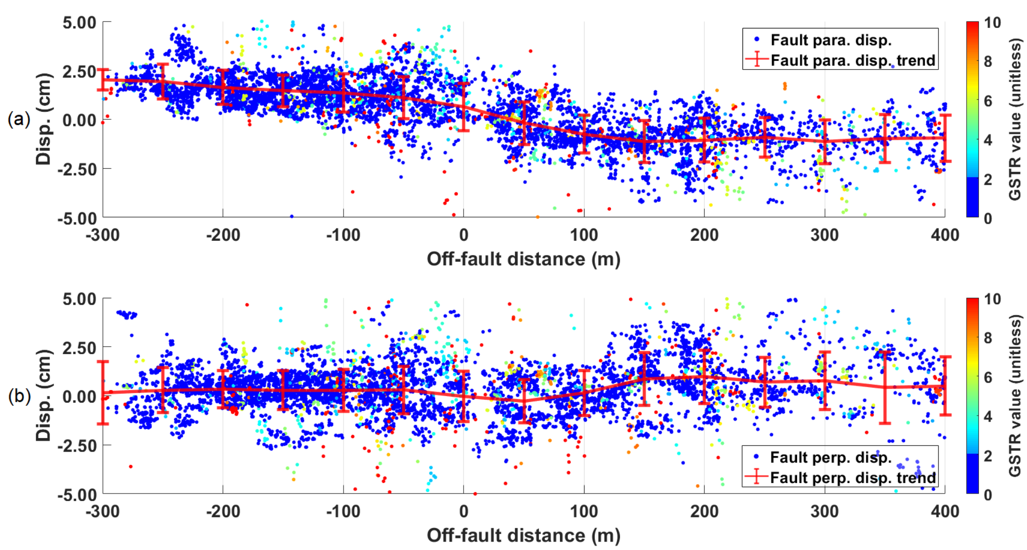

Figure 5.10 Distribution of fault parallel (a) and fault perpendicular (b) creep components versus off-fault distance. Points are color coded by GSTR values to indicate robustness of regression geometry.

Given that the centimeter-level creep displacements along the fault show little variation, it is beneficial to examine displacement profiles across the fault to highlight any off-fault displacement patterns such as fault asymmetry and nonlinear displacements. Figure 5.10 shows stacked displacement profiles over the entire MLS surveyed area. Trend lines represent a local average of displacements with error bars indicating 50 m binned mean and variance of displacement. These profiles highlight the off-fault variation of fault creep displacements and curvature of the displacement profile that can potentially assist with inferring fault slip at depth [6]. In Figure 5.10 (a), the fault parallel displacement profile shows curvature within 150 m off-fault and reflects the nonlinear variations of displacement detected in the near field. In the far field, beyond 150 m off-fault, displacements are more uniform, and the overall off-fault dextral displacement is calculated as 2.5 ± 1.5 cm (1σ). In Figure 5.10 (b) minor fault perpendicular creep is present in the far field with a magnitude of -0.5 ± 1.3 cm (1σ). The scattered displacement records are color coded by GSTR, with inliers colored in blue. The blue dots are clustered around the trend with the remaining colored dots spread out with a larger variance within the change detection results. This clustering suggests that GSTR is a good indicator of the strength of the least squares solution and can be used as a filter for robust creep displacement estimates. Only the filtered data (blue dots) contribute to the displacement trend line and error bars shown in both figures; they are computed by binning displacement estimates in 50 m wide bins.

One has to be cautious when interpreting the results in Figure 5.9 and Figure 5.10 because projection accuracy is highly correlated to the definition of the fault trace, which is interpolated based on the field survey of alinement arrays. Although consistent cracks on roads and curbs should be treated as promising evidence of the fault trace, there are limited observations of the ground rupture. Fault slip at depth does not necessarily migrate to the ground surface and deterioration and thermal changes may also lead to scattered cracks that are not necessarily along the strike. Therefore, the fault trace in between surface observations can only be estimated by interpolation and regression. As shown by the distribution in Figure 5.9 and the trend in Figure 5.10, the 'offset' and the 'plateau' are not perfectly centered on the assumed fault trace (where off-fault distance equals zero). This is also confirmed by some sections of the displacement field in Figure 5.8 where the transition zones for the displacement arrows are not centered at the fault trace. Given the discrepancies between these displacement fields and the interpolated fault trace, a more accurate fault trace definition would most likely result in a better estimation of true off-fault creep deformation.

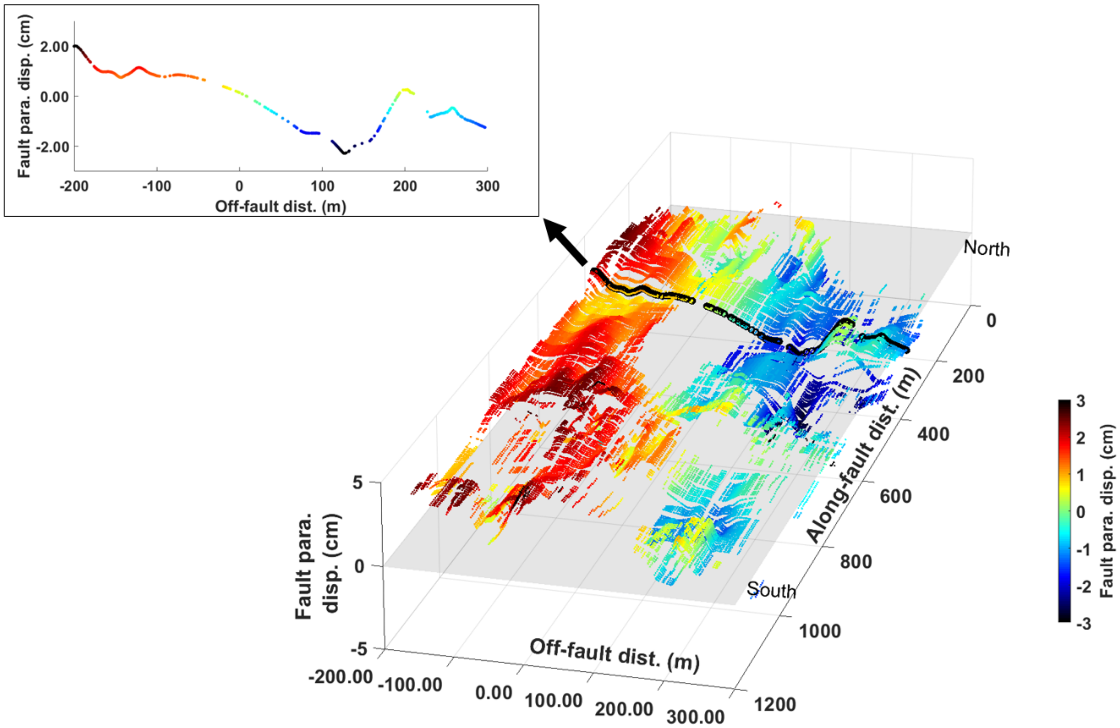

Figure 5.11 Off-fault fault parallel displacement profiles stacked along the fault strike. Each profile represents a 50 m binned average of the displacements at various off-fault distances.

The profiles in Figure 5.10 enable investigations of fault displacement in the off-fault principle direction; however, the along fault variation of displacements are not evident because the profiles are stacked. Off-fault profiles can be generated at different locations along the fault such that along-fault variations in creep rates can be revealed. Referring to the north end of the MLS survey area as the starting point of the fault trace, along-fault distances are measured and a cascade of off-fault displacement profiles are calculated by sliding a 100 m search window along the fault trace. Figure 5.11 shows each profile as a local regression [138] of the detected displacements within a window 100 m along and 400 m across the fault. The span of the regression is set at 10% which is equivalent to a 50 m moving average along the displacement profile. The cascade of profiles are generated by sliding a 100 m search window along the fault trace with an increment of 5 m, and displacements profiles are colored by the amount of fault parallel creep. In this figure, a minor reduction of fault parallel displacements can be found from North to South; this is consistent with the regional trend detected by the alinement arrays (Figure 5.3) that spans the area surrounding the MLS survey.

5.4.3 Validation of the MLS estimates of creep

The Hayward fault is well known for the comprehensive alinement array stations maintained by McFarland et al. [124]. Details of how the alinement array data are collected and processed can be found at the Galehouse et al. [10]. The alinement arrays are surveyed with a theodolite such that any fault parallel movement greater than 1-2 mm can be confidently detected. Here, we use the theodolite surveys of the alinement station HCAM to validate our creep estimates. The location of HCAM can be found in Figure 5.1. Although the fault trace is determined by multiple alinement array stations, stations other than HCAM are not compared because they are not covered by persistent MLS observations.

As shown in Figure 5.12, the fault crossing at HCAM is marked as a circle and the associated survey monuments IS and ES are marked as triangles. The alinement array surveys measure the angular changes of permanent survey monuments located at an alinement station. Dextral fault-parallel creep displacements are then derived from the angular changes. At station HCAM, relative fault parallel displacements are reported at survey monuments IS and ES located 44 m off-fault, and the fault trace is interpolated from adjacent alinement array stations, shown as the dark red line. The equivalent MLS measurement is the relative fault parallel displacements detected around the survey monuments. Displacement vectors detected within 20 m of the survey monuments IS and ES are outlined and colored (red-east, yellow-west). Figure 5.12 displays 20 m wide displacement fields along the line

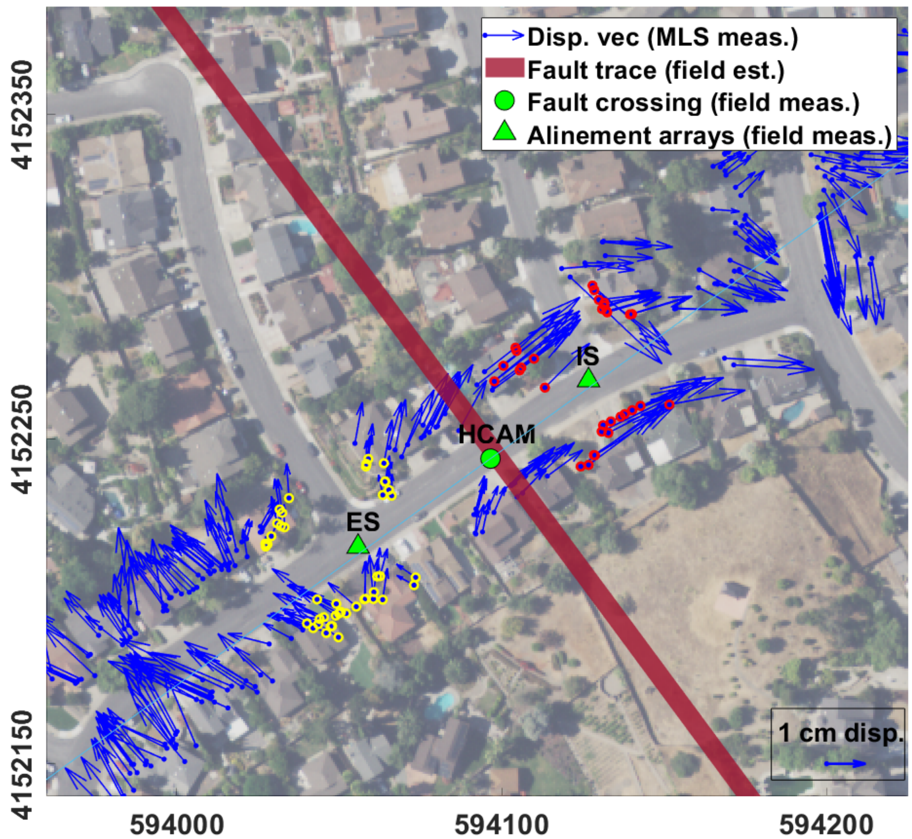

Figure 5.12 Displacement field across the fault at alinement station HCAM. Basemap from NAIP Digital Georectified Image courtesy of the U.S. Geological Survey [20].

between survey monuments. The corresponding displacement estimates are highlighted with circles and average displacements along the fault are calculated and compared with the theodolite estimates.

The validation results are shown in Figure 5.13. In (a), the displacement vectors and the locations of alinement stations are re-plotted with the fault trace centered at the origin and y-axis along the fault trace, i.e. centered at the fault trace and rotated by the strike direction. Corresponding displacement vectors for survey monuments IS and ES are circled. Labels for HCAM, IS and ES are the same as Figure 5.12. The off-fault distributions of fault parallel and fault perpendicular displacements are shown in (b) and (c) and the

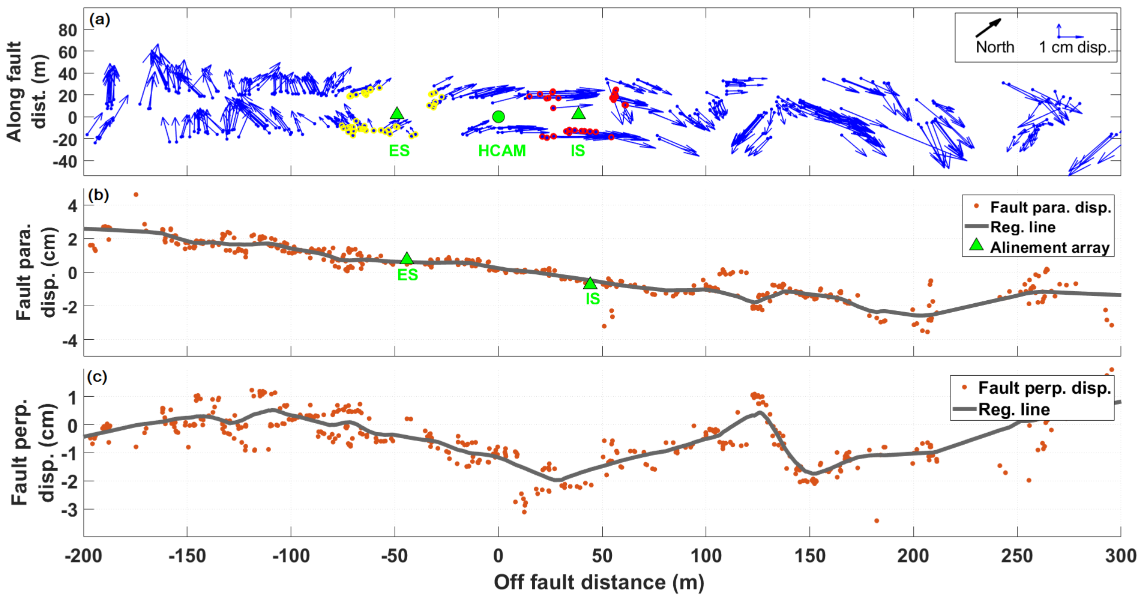

Figure 5.13 (a) Detected displacement fields viewed from an off-fault perspective. (b) Profiles of the fault parallel displacement overlaid with coincident alinement array measurements. (c) Profile of the fault perpendicular displacement.

coincident alignment array measurements are overlaid on (b) where the Y-offset of survey monuments represents the dextral displacements detected by the alinement array over the same approximate time period. Displacement trends are estimated using a robust local linear regression [138]. Relative dextral displacement is estimated from displacement fields detected 20 m from the survey monuments IS and ES where averaged displacement projections along the fault trace are calculated. At station HCAM, the MLS estimate is 1.1 ± 0.7 cm (1σ) relative dextral displacement from survey monuments IS to ES from July 2015 to June 2017 while the alinement array survey reports 1.5 ± 0.7 cm displacement from Oct. 2015 to Oct. 2017. Note that the 4 mm difference between MLS and the alinement array estimates is within the measurement uncertainties of both methods. The difference may be caused by the slightly different observation periods for each. As shown in the long term records for HCAM and adjacent stations (Figure 5.2), the creep rate along the Hayward fault is not constant and can vary by several millimeter per year.

It also appears, based on the profiles in Figure 5.13 that the HCAM alinement array stations are within the fault zone of deformation and therefore may not completely capture the off-fault creep deformation. A localized rotation of the MLS displacement vectors can be found between -10 m and 50 m off-fault. The orientation of the vectors is almost perpendicular to the fault trace. The rotation is also captured in the fault perpendicular displacement profile in Figure 5.13 (c). A second profile minima is observed between 130 m to 170 m off-fault from a similar rotational pattern. This second local minimum suggests that the alinement array monument IS is located within the deformation zone while the ES-IS baseline does not span the entire creeping zone. To confirm that these detected rotational patterns are not a consequence of the smoothing induced by the moving window employed, a synthetic test was conducted, with details presented in Section 5.4.4.

5.4.4 Detection of synthetic creep

To better understand the uncertainties of the proposed change detection strategy, a synthetic test was undertaken with a synthesized fault creep. In the synthetic configuration, reference and secondary datasets were generated by randomly drawing two point clouds from the 2015 MLS data, and adding a 4 cm rigid dextral displacement with dislocation at the fault trace to one of the point clouds. This offset matches the scale of the expected far-field displacement. The displacement configuration also ensures an upper bound of the fault creep as the near-field displacement accommodates all the far-field fault slip instantly at the fault trace.

Figure 5.14 and 5.15, show example profiles near HCAM with the 4 cm synthetic dislocation. The synthetic results show a 0.2 cm variation represented by the thickness of the displacement profile as shown in (b) and (c). A smoothing effect induced by the moving window can be found $\pm$10 m off-fault, shown as the grey rectangle in (b), where the simulated stair-like displacement is detected as a linear transition off-fault. No bias in the direction of the detected displacements are shown in Figure 5.16. Actual displacement directions are plotted as the red line representing the average strike of the fault trace. No

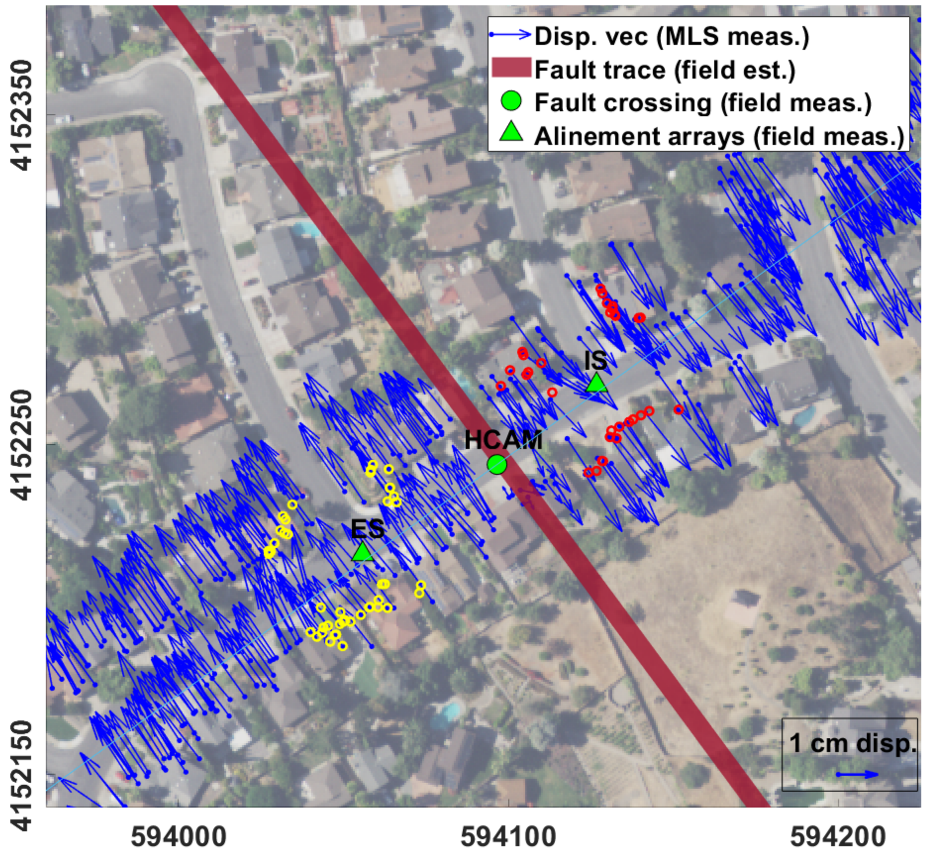

Figure 5.14 Synthetic displacement field at alinement station HCAM. Basemap from NAIP Digital Georectified Image courtesy of the U.S. Geological Survey [20].

bias from these directions as the bins are centered on the red line. The angular variation of the vectors is only 10° (1σ).

The synthetic results show that the selection window for the planes has only a minimal smoothing effect on the estimate of displacement as it crosses the simulated fault location. The window size does not seem to affect the estimated displacement direction significantly. It is, therefore, highly unlikely that the transition width displayed in Figure 5.13, which appears to be at least 50 m wide with a noticeable systematic rotation pattern, is caused by the size of the selection window.

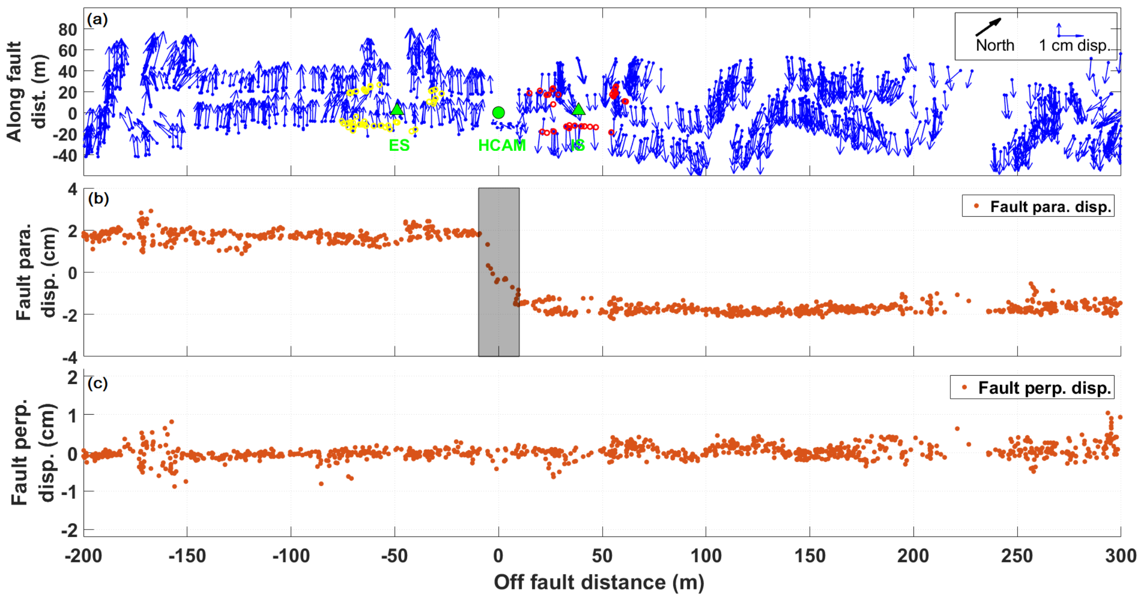

Figure 5.15 (a) Detected displacement vectors viewed from the off-fault perspective (centered at the fault trace and rotated by the strike direction). (b) Profile of fault parallel displacement. (c) Profile of fault perpendicular displacement.

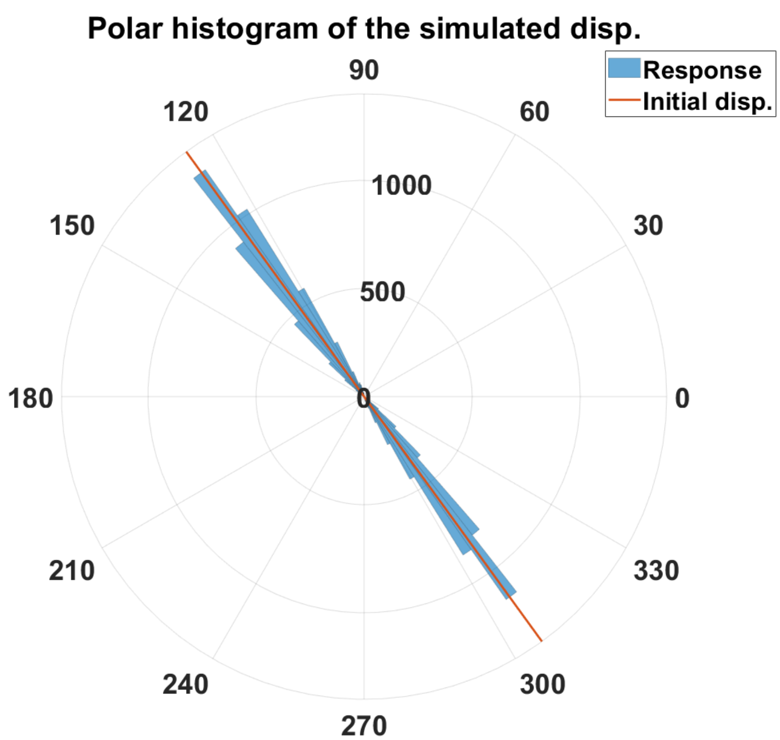

Figure 5.16 Angular histogram of the detected displacement vector orientation.

5.5 Discussion

5.5.1 Generality of the proposed change detection strategy

The structure of the proposed two-step strategy leads to a general framework for change detection not limited by the type of fault, the deformation rate or the primitive geometry. The method detects changes in 3D; vertical changes can also be estimated for a non strike-slip fault. In the first step, implementation of the RANSAC corr-planar detector leverages the slow deformation characteristics of the fault creep where the secondary point clouds are expected to be nearly adjacent to the reference point clouds. The method would still be feasible without the assumption of slow deformation as alternatively, a coarse alignment (like ICP) could first be applied either globally or locally. The RANSAC detector could then be implemented with the consensus threshold adjusted accordingly based on the estimated accuracy of the ICP solution. The selection of geodetic marker type can also be adapted to other geometric primitive besides planar surfaces. The 'parallel' consensus threshold and the sequential RANSAC strategy can be applied to other types of corresponding geometric primitives such as concentric cylinders and spheres.

In the second step, the combined least squares adjustment framework can also be augmented to incorporate different types of primitives. Equation 5.1 can be generalized to combined primitives of various types conditioned by their own geometry as shown in Equation 5.3, and the estimate on the rigid transformation remains as shown in Equation 5.2. By using a wider variety of geometric primitives, the geometry of the geodetic markers will be more distinctive and should improve the regression geometry GSTR and accuracy. The smoothing effect induced by the moving window search would also be suppressed as a smaller search window can be used with a wider selection of candidate primitive types. This type of generalized geometric primitive framework is already planned to augment the approach presented.

The proposed two-module strategy can be extended to estimate change for faulting outside of urban neighborhoods. The detection using corr-planar primitives is practical and feasible as planar surfaces are abundant in urban areas. However, the environment demonstrated in this project is relatively simple as repeated houses in the same neighborhood contribute most of the planar features for change detection. As planar surfaces can be extracted from buildings or other types of constructions at various sizes with different scan uncertainties, static thresholds implemented by this project may not be optimized for different anthropogenic environments. Besides scan uncertainties, construction materials on facades and roofs of a building may also introduce additional roughness or curvature that needs to be considered for the RANSAC corr-planar detection. Further parameter tuning and adjustment is necessary to implement this method in different environments. Generalizing the method to be scene invariant will require the examination of more datasets collected in differing environments.

The dense measurements of fault creep clearly highlight the benefit of MLS high-resolution change detection. The mobile platform provides a side-looking scan that enables better point-cloud definition of vertical features which is ideal for measuring horizontal deformation. Other techniques, such as structure from motion digital imaging could also potentially be used to provide the input point clouds for change detection (e.g. Ekhtari and Glennie [12]). If the images were acquired from airborne platforms (e.g. UAS platform) then they may provide more uniform coverage as their acquisition is not limited to the roadways, although potential occlusions by vegetation may limit their use in some areas. There may also be some issues because the structure from motion/multiview stereo photogrammetry (SfM-SVS) process tends to round sharp edges [140] which may deform the planar surfaces being used for estimating deformation.

5.6 Conclusion and future work

Herein, an MLS-based change detection framework to monitor the slow deformation of aseismic fault creep along a segment of the Hayward fault has been described. The fault deformation was elucidated as displacement vectors with meter-level resolution and sub-centimeter accuracy. The detected displacement vectors show nonlinear deformation patterns in the near field and 2.5 ± 1.5 cm dextral displacement in the far field (> 150 m off-fault). Rotational patterns are detected within the nonlinear deformation zone close to the fault. The magnitude of creep displacement estimated was validated using a collocated alinement array station with millimeter-level agreement. The detected displacement fields can be used to elucidate the complex physics of faulting near the Earth's surface and the nonlinear deformation pattern and the scale of off-fault displacement can be used as a reference to set up future geodetic and geophysical networks for monitoring fault dynamics.

The two-step change detection strategy was shown to be practical and feasible. The RANSAC-based corresponding planes detector seeks corresponding temporally spaced geodetic markers by leveraging the slow deformation characteristics of fault creep, and the combined least squares displacement estimator is used to quantify both the relative fault creep displacement and the regression of the primitive geometry simultaneously.

The change detection method was assessed from the perspective of the reliability of the geodetic markers, the smoothing effect of the moving window detection, and the potential generalization of the framework. GSTR was shown to be a practical metric to quantify the robustness of the regression geometry. A conservative test using a synthetic fault displacement shows approximately 2 mm detection uncertainties for dextral slip, 10° angular uncertainties in displacement orientation, and ± 10 m off-fault smoothing caused by the size of the planar selection window.

For future work, we plan to generalize the choice of geodetic markers such that non-planar primitives can also be used to track deformation. We also plan to use multiple temporally spaced MLS surveys in a simultaneous adjustment network to further improve the accuracy and reliability of the creep estimates.

Chapter 6

Multi-temporal change detection for lidar time series analysis

6.1 Introduction

Change detection is the process of identifying differences in the state of an object by observing it at different times [51]. With new sensors and observation methods available, it is necessary to develop corresponding change detection algorithms that better fit both the data and applications. From site-specific sparse geodetic measurements acquired from, for example, GNSS and theodolite, to distributed photogrammetric and remote sensing mapping like aerial imagery, lidar and radar, the spatial coverage and resolution of geodetic measurements have increased rapidly, and the associated change detection results have evolved from site-specific sparse differencing to the 2D and 3D mapping of deformation fields. Such improvement boosts applications that use distributed geodetic measurements to infer deformation patterns and displacement profiles which reflects the spatial variation of the physical deformation source. Among new high-resolution observations, lidar data provide robust measurements of the ground surface, flexible spatial coverage and detection resolution compared with aerial imagery and InSAR for the task of earthquake fault creep detection (for example Nevitt et al. [5], Brooks et al. [6], Nissen et al. [13], Zhu et al. [141]).

In recent years, light detection and ranging (lidar) has joined the family of sensors used for deformation detection where improved spatial resolution and more accurate range measurements are available. The increased resolution and accuracy come with an irregular and complex format within the lidar point cloud which promotes the development of new methods for processing the data. Compared with the regular grid format used for image change detection, new methods for combining and regularizing point clouds are needed. Meanwhile, as lidar gains in popularity, data collection methodology is more mature and standardized where revisited and repeated lidar surveys are feasible for deformation monitoring. As repeated surveys accumulate, there is a lack of point cloud time series change detection methods where consistent change can be estimated over time.

Strategies for time series analysis are commonly found in satellite optical imagery and radar data processing where stable features observed from repeated orbits such as cross-correlated pixels in the optical imagery [142–145] and persistent scatters in persistent scatter interferometry [126, 127, 146] are tracked for change detection over time. Similar to these methods, the idea of lidar time-series analysis should also leverage corresponding features represented in temporally spaced point clouds. Some of the initial applications in the literature employed a hybrid method using lidar and imagery data where a single epoch of lidar observations is used to enhance the extraction of the persistent features from an imagery time series. Applications are commonly found in change detection of forest canopy where lidar data is leveraged for detecting canopy height and supporting the satellite imagery analysis of canopy coverage change (e.g. Ahmed et al. [147], Bolton et al. [148]). A few applications directly work on lidar point clouds for coastal change detection where cohesive elevation change over time is tracked to detect the elevation difference between lidar DEM epochs (e.g. Anders et al. [149, 150]). These applications have achieved better change detection results with the help of lidar and they have inspired us to explore methods of lidar time series analysis with a more generic formulation where primary persistent point cloud features can be tracked for 3D change detection.

In our previous work [141], we have used corresponding planar surfaces as persistent geodetic markers for urban change detection. In this work, we will show an extension of that framework and expand the change detection to multi-temporal lidar observations. The proposed method leverages persistent planar surfaces that are commonly found in lidar point clouds and uses multi-temporal corresponding planar surfaces to estimate the deformation time series with additional constraints on the internal temporal consistency. We provide a case study for fault creep ground displacements and provide validations with redundant independent geodetic measurements. The precision of the detection is estimated from synthetic displacements on real MLS point clouds and compared with state-of-the-art change detection algorithms. The proposed methodogy provides a generic change detection framework for lidar time series analysis that leverages both geometric and temporal constraints simultaneously in a single optimized least squares adjustment.

6.2 Data

Mobile laser scanning (MLS) data were collected in July of 2015, June of 2017, and August of 2018 along a 2 km segment of the Hayward fault near Fremont, California. The MLS surveys were conducted at a local neighborhood crossed by the Hayward fault trace. The point clouds are acquired in a typical urban neighborhood with single-family houses are scanned from the local roadway. The MLS survey area is shown in Figure 6.1, and the collocated alinement array and creepmeter measurements are shown in the subplot and used as validation for the MLS measurements. Discussion of the Hayward fault tectonics can be found in Savage and Lisowski [151] and Lienkaemper et al. [152].

6.2.1 Historical geodetic observations

Monitoring of aseismic fault slip on the central San Andreas fault system can be traced back to 1956 [153]. As one of the main faults of the system, the Hayward fault was identified in 1960 [154] and fault creep was documented by geodetic observations using alinement arrays, trilateration networks, and creepmeters [155–158]. The segment of the Hayward fault in Fremont, California, used in this study, has been monitored by creepmeters since 1993 [158, 159] and alinement arrays as early as 1979 with extended site observations after the 1989 Loma Prieta earthquake [10, 160]. As part of an earthquake cycle, temporal anomalies of creep rate observed from alinement arrays are used to infer potential precursory seismic activity [161–163], and spatial variations of surface creep can be used to infer the depth of shallow faults [5, 6, 59, 151, 164]. Starting in 2013, mobile lidar data

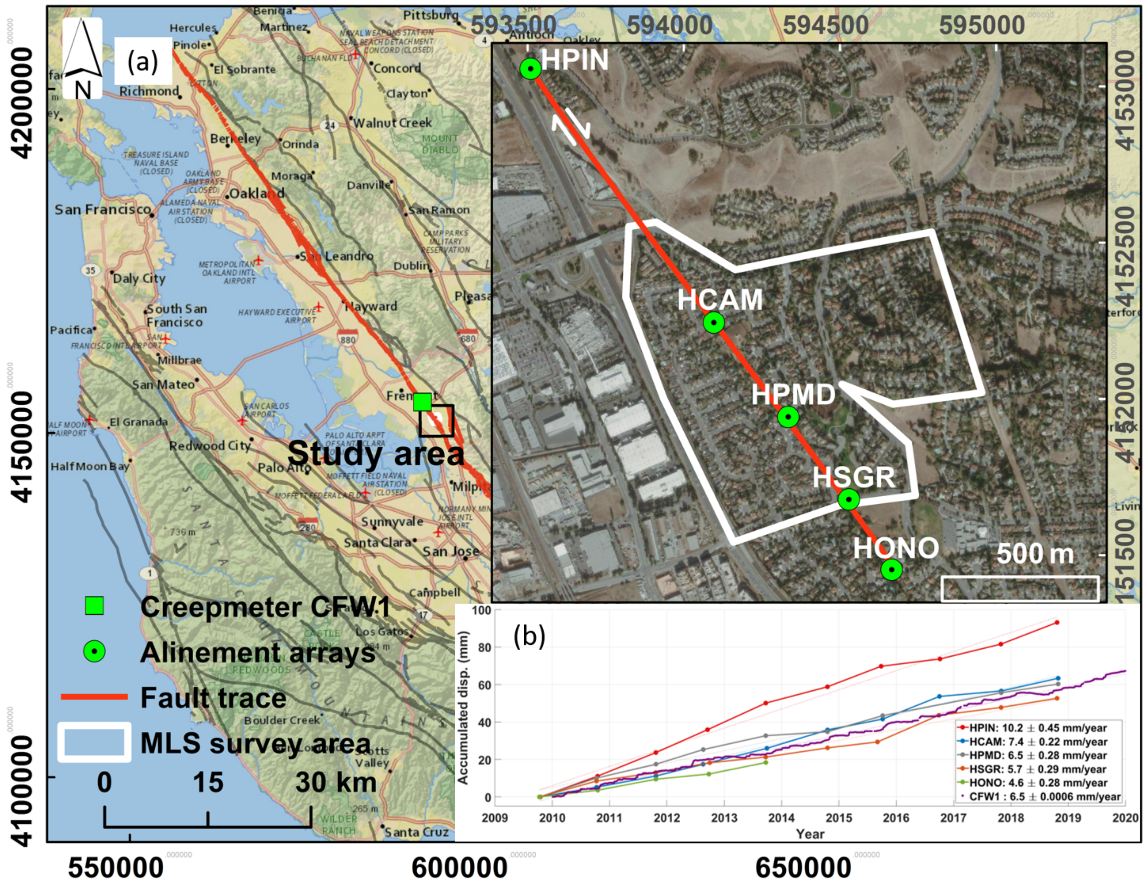

Figure 6.1 MLS survey area. (a) Study area and locations of collocated alinement array and creepmeter. (b) Ten years of alinement array and creepmeter measurements of fault parallel ground displacements.

were collected straddling the fault trace. To better understand shallow fault behavior and examine shallow fault processes, repeated multi-temporal lidar surveys were conducted to monitor the evolution of nonlinear ground displacement in the near field of the fault creep. This work examines three years (2015, 2017, and 2018) of MLS observations collected from this survey which were chosen for their consistent spatial coverage.

Spatially distributed geodetic observations are preferable to resolve high resolution, non-linear ground displacement in the near field. Displacement fields play an important role in shallow slip modeling as dense measurements of ground displacement can be used to infer the depth of the fault. Temporally distributed repeated high-resolution scan can be used to monitor accumulated ground deformation and anomalies within the displacement pattern to assess potential seismic hazards [32].

6.2.2 Data preprocessing

Before change detection, point clouds require preprocessing including pre-alignment and point feature generation. To isolate nonlinear deformation in the near field, corresponding point clouds need to be aligned in the far field where uniform displacement is expected. Our previous works [130, 141] suggest that ,for the Hayward fault, far-field displacement more than 150 m from the fault trace is stable and uniform. Therefore, we have run the proposed change detection method at these locations, and the estimated displacement is used to pre-align the point clouds. This pre-alignment removes any possible datum or reference frame offsets, and because fault creep results in a relative displacement, the pre-alignment does not affect the overall estimates of creep. The precision of such an alignment is validated by a synthetic test as shown in Section 6.5.1.

Preprocessing also includes calculation of point normal and local curvature at a point using its closest neighbors. These point features are computed using the Point Data Abstraction Library [133] where the normal and curvature are calculated using eigenvalue decomposition of the 8-closest neighbors. The ground surface is removed from the raw MLS point cloud to isolate houses and other anthropogenic features for further analysis. Because Hayward fault is a right-lateral strike-slip fault, we expect the motion to be predominately horizontal. Therefore, the ground plane, which mainly constrains vertical movement, is removed after the pre-alignment. If significant vertical motion was expected, the ground points could be included in the subsequent processing.

6.3 Methods

Generally, change detection for a lidar time series requires tracking the locations of stable point cloud features that persist over repeated MLS surveys. Given a steadily changing environment, i.e. the survey area evolves slowly over time, or survey frequency is very high, it is reasonable to assume closely located objects are moving at a constant rate. Therefore, a rigid body transformation is expected from successive observations acquired at the same location. Given this assumption, the goal of change detection can be broken into: (1) tracking the rigid body transformation of common features that are extracted from a pair of MLS surveys, (2) adding additional constraints on the spatial and temporal consistency of the bi-temporal change given multi-temporal observations (i.e. more than two surveys).

Zhu et al. [141] proposed a framework for bi-temporal change detection where two years of MLS data are processed for ground displacement of fault creep that deforms at a rate of several mm per year. The method resolves distributed ground displacement as rigid body transformations estimated at corresponding features extracted from MLS point clouds. To expand this bi-temporal framework into a multi-temporal change detection for lidar time-series analyses, additional constraints are appended to the original framework to ensure the temporal and spatial consistency of the detected change. In the following sections, we will first introduce methodology to extract corresponding features across the lidar time series, then elaborate how these features are used for multi-temporal time series change detection at a single query location. The final formulation presented expands the detection algorithm using flexible query locations with an adaptive search window size.

6.3.1 Corresponding planar primitive detection

Planar surfaces are commonly found in an urban environment. As a primary element of architecture, planar surfaces can be easily captured by a lidar scan and extracted from point clouds. Well-constructed planar surfaces such as building walls and roofs preserve their shape during mild geological deformation like fault creep or land subsidence, therefore, they are ideal geodetic markers to track ground displacement. Planar surfaces extracted and modeled from point clouds are called planar primitives given their primary planar geometry; consistent planar primitives observed at different epochs can be used to resolve temporal change.

In a lidar time series, persistent planar surfaces can be captured multiple times to produce a series of corresponding planar primitives. Here, a RANSAC-schemed plane detector is used with point-to-plane distances and normal deviations as the consensus threshold for search. Corresponding planar primitives are extracted using the detector with a relaxed threshold adapted for the entire time series. As a starting point, the absolute value of the threshold can be estimated by referring to historical measurements of the creep rate from collocated geodetic observations as shown in Figure 6.1. For lidar observation collected in 2015, 2017, and 2018 the point-to-plane distance and normal deviation thresholds are set to be 30 cm and 10° respectively for the initial rough search for corresponding planar surfaces.

As the observations extend to multiple epochs in the lidar time series, temporal deformation and occlusions can exist within the corresponding planar primitives. Temporal deformation reflects the accumulated displacement over time such that a more relaxed consensus threshold has to be used. As a result, outliers and false-positive point samples could be captured. Occlusions happen when temporary obstacles shadow the laser scanner, for example cars, humans, etc, causing inconsistency of the detected planar surfaces. Occlusions can leave voids in the point clouds, and their patterns are unique because they are determined by both the laser field of view and the obstacle location. To compensate for temporal deformation and occlusions, a secondary RANSAC detector is introduced to refine the detection of planar surfaces. Pseudocode for detecting a corresponding planar primitive is shown in Algorithm 1.

While the first RANSAC detector runs on the combined multi-temporal point clouds, the second RANSAC detector detaches from the time series and runs on individual epochs. With the detector only running on one epoch at a time, the consensus threshold is independent of temporal dislocation in the time series and is designed to refine the search for individual planes. The consensus point-to-plane distance and angular thresholds are set as

Algorithm 1 Corresponding planar primitive detector

Input:

- Point clouds $P = \{pc_1, pc_2, \ldots, pc_n\}$ as point cloud acquired from epoch i
  - i is index of epoch, $i = 1, 2, \ldots, n$
  - n is the index of the last acquisition
  - pc_i = {points : attribute as [X, Y, Z, normal direction, curvature]}
- Query location $Q = \{q_1, q_2, ...\}$
- RANSAC threshold:
  - $th1$ = (point to plane distance 1, angular deviation 1)
- Secondary RANSAC threshold:
  - $th2$ = (point to plane distance 2, angular deviation 2)

Initialize:

- Nearest neighbor points: $\rightarrow K = \{k_1, k_2, \ldots, k_n\}$
- Consensus set: $\rightarrow C = \{c_1, c_2, \ldots, c_n\}$
- Plane point cloud: $\rightarrow Plane = \{pl_1, pl_2, \ldots, pl_n\}$

for every query location q **do**
    find K in P at the location q for all epochs
    RANSAC on K with $th1$, consensus sets $\rightarrow C$ for all epochs
    for every epoch i **do**
        retrieve nearby points k_i at the centroid of c_i for this epoch
        Secondary RANSAC on k_i with $th2$, consensus sets $\rightarrow plane_i$ for this epoch
    end for
end for

5 cm and 8° for the fine search of planar surfaces. In addition, the second detector window is re-centered at the centroid of the detected plane patch to mitigate the effect of occlusions. Given the relocation of the search, the second RANSAC allows planar points outside the initial search window to be retrieved such that the detection of a plane is independent of its counterparts observed from other epochs.

The aforementioned two-step RANSAC detection is executed multiple times at a single query location. As each set of corresponding planar points is extracted and removed, the detection is iterated to retrieve other sets until no sets of planes with the minimal amount of 100 points remain. The implementation of the second RANSAC detection in each iteration increases the confidence of removing points with a refined consensus threshold such that more robust results can be achieved to detect multiple planes at a single query location. Figure 6.2 shows detected corresponding planar primitives where the point clouds are colored by the number of total points associated with the primitive. A majority of planar primitives are detected from building walls, roofs, and garage doors as shown in (b).

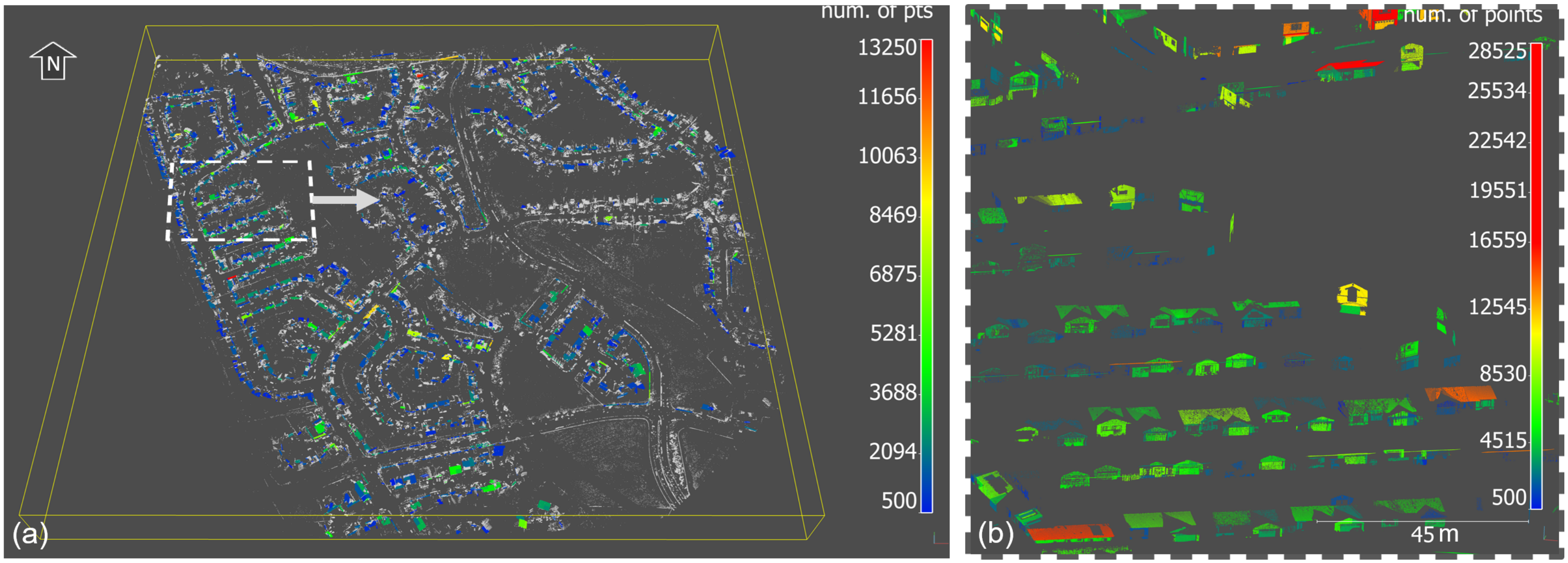

Figure 6.2 Corresponding plane detection shown at one of the observation epochs. (a) Corresponding planes detected in the entire MLS survey area shown from a perspective view. (b) Orthographic view of a zoomed in area. Figure prepared with CloudCompare [21].

6.3.2 Multi-temporal change detection

Given a group of coincident corresponding planar primitives, the displacement from one epoch to another can be estimated from a bi-temporal rigid body change detection as shown in [130, 141]. The detection is estimated using closely located planar primitives such that all planar surfaces extracted from a defined local neighborhood move with a shared displacement. The augmented least squares adjustment jointly estimates the displacement vector simultaneously with the geometry of each planar primitive. This combined least square adjustment leverages the redundant representation of a planar surface from point clouds and the redundant representation of the ground displacement estimated from a collection of closely located planes. Therefore, the change detection can achieve better accuracy than using individual laser point measurements (e.g. initial method used in ICP Besl and McKay [90], Arun et al. [165]) which enable a sensitive yet robust detection.

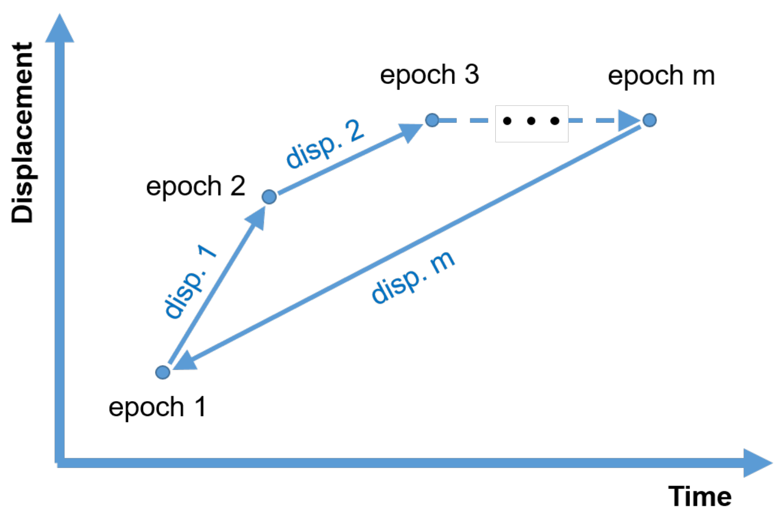

Figure 6.3 Lidar time series represented as a bi-temporal change detection loop. For this project, epoch 1-3 corresponds to MLS data collected in 2015, 2017 and 2018.

The extension of bi-temporal change detection requires reformulating the least squares adjustment for multiple epochs or multi-temporal change detection. Given a lidar time series, a closed-loop of detections can be formed where adjacent temporal point clouds are connected by individual bi-temporal change detections, and the first and last epoch are connected with a detection estimating the overall temporal displacement as shown in Figure 6.3. Similar to the detected unwrapping error used in InSAR time-series analyses (e.g. Shanker and Zebker [166], Doin et al. [167]), the lidar time-series displacement error is the Euclidean norm of the misclosure of the displacement series, and the angular error is the angular deviation of the plane norms estimated at each corresponding plane. These displacement and angular misclosures provide additional constraints to the least squares adjustment which enhances the temporal and spatial consistency within the detection series.

Let i represent the epoch index and $i = 1, 2, .., m$ corresponds to the first to last temporal observation, and let j represent the index of the planar primitive and $j = 1, 2, ..., k$ corresponds to the planar surface index, then the least squares regression for epoch i can be formed as

$$epoch_i \begin{cases} f_{pre} = (\boldsymbol{X_{i,j}} - \overline{\boldsymbol{X_{i,j}}}) \cdot \boldsymbol{n_{i,j}} = 0 \\ f_{post} = (\boldsymbol{R_i}(\boldsymbol{X_{i+1,j}} - \overline{\boldsymbol{X_{i,j}}}) + \boldsymbol{T_i}) \cdot \boldsymbol{n_{i,j}} = 0 \end{cases}, \tag{6.1}$$

where $\boldsymbol{X_{i,j}}$ are the point clouds $[X, Y, Z]^T$ collected at epoch i for primitive j that has a plane normal $\boldsymbol{n_{i,j}} = [n_x, n_y, n_z]^T_{i,j}$. $\boldsymbol{R_i}\, and\, \boldsymbol{T_i}$ represent the rigid body rotation and translation components that are the detected displacements from epoch i to epoch $i+1$. Note that for the last epoch, $m+1$ is designed to wrap back to the first measurement such that $m+1$ is set as epoch 1. For the time series, the observation equation 6.1 is subject to constraints

$$\forall(i,j) \begin{cases} g = \|\boldsymbol{n_{i,j}}\| - 1 + \sum_{i=1}^{m-2} \det(\boldsymbol{n_{i,j}}, \boldsymbol{n_{i+1,j}}, \boldsymbol{n_{i+2,j}}) = 0 \\ h = \|\sum_{i=1}^{m} \boldsymbol{T_i}\| = 0 \end{cases}, \tag{6.2}$$

where g is the geometric constraints on the estimated planar surfaces. The regression estimates plane normals as a unit vector such that $\|\boldsymbol{n_{i,j}}\| = 1$. The angular error is represented by the volume of a pyramid with the plane normal observed from different epochs located on its edges. Given slow-changing displacement, a planar normal shouldn't change significantly over time, such that the pyramid volume $\sum_{i=1}^{m-2}\det\left(\boldsymbol{n_{i,j}},\boldsymbol{n_{i+1,j}},\boldsymbol{n_{i+2,j}}\right)$ should be minimized. Finally, h is the displacement error where the misclosure of the sum of the displacement should be zero, as constrained by its Euclidean norm $\|\sum_{i=1}^{m}\boldsymbol{T_i}\| = 0$.

The complete solution to the system can be found using a Gauss-Helmert model [135]. A step-by-step solution of a similar bi-temporal framework can be found in Zhu et al. [141]. The overall normal equation described by Equations 6.1 and 6.2 for the combined least squares adjustment can be found in Appendix A.

6.3.3 Change detection with flexible query point and adaptive search window

Multi-temporal change detection requires j closely located corresponding planar primitives to estimate a displacement vectors at any query location. Rather than estimate the regression at the location of any plane, we generalize the detection to an arbitrary query grid that spans the entire MLS survey area. Although searching on a regular grid is an arbitrary design, the regularized detection results are beneficial for further geological and geomechanical interpretations.

At any query location, the quality of the regression used in the change detection is determined by the geometrical distribution of the planar normals. Because a single plane is only sensitive to displacement along its normal direction, a collection of planes with diverse normal directions has better regression geometry and results in more robust displacement estimates. To quantify the robustness of the regression geometry, an independent measurement of the geometric strength of the translation (GSTR) is proposed by Zhu et al. [141]. The rule of thumb is to choose a number of closely located planes that result in a GSTR under 2 for robust regression geometry in a bi-temporal detection.

Given the regularized query grid and the criteria for choosing a robust selection of planes, an adaptive search window size is selected as the smallest window at any query location that satisfies the GSTR constraint. A maximum search window size is predefined as 50 m to provide a lower bound on change detection resolution. To ensure that the selected planes are evenly distributed within each window, three out of four grid quadrants are required to be occupied as the detection is estimated roughly at the centroid of every set of planar primitives.

6.4 Results

The change detection results from the lidar time series are a series of ground displacement fields calculated from connected epochs of MLS observations (Figure 6.3). In this case, three displacement vectors are estimated to resolve ground displacement from 2015-2017, 2017-2018 and 2018-2015. The displacement field can be represented as a quiver plot, where vectors of the displacement are plotted at the corresponding query grid. The displacement field can be further interpreted by decomposing the displacement vector into fault parallel and fault perpendicular displacement with respect to the nearest observed fault trace. This off-fault displacement format is used by other geodetic observations like alinement arrays and creepmeters, and the off-fault displacement profile can be used to infer further properties of fault mechanics, therefore, a transformation to this format is necessary for data validation and further analyses.

6.4.1 Detected ground displacement fields

Fault creep is detected as the displacement fields shown in Figure 6.4. The dextral displacement pattern can be more easily identified if the accumulated displacement between two epochs is large (i.e. if the temporal spacing is larger). Each displacement vector represents the local change observed by a set of close-by planar primitives extracted from lidar point clouds, and the estimated change results from predominantly physical ground motion plus errors, which are examined in the following section.

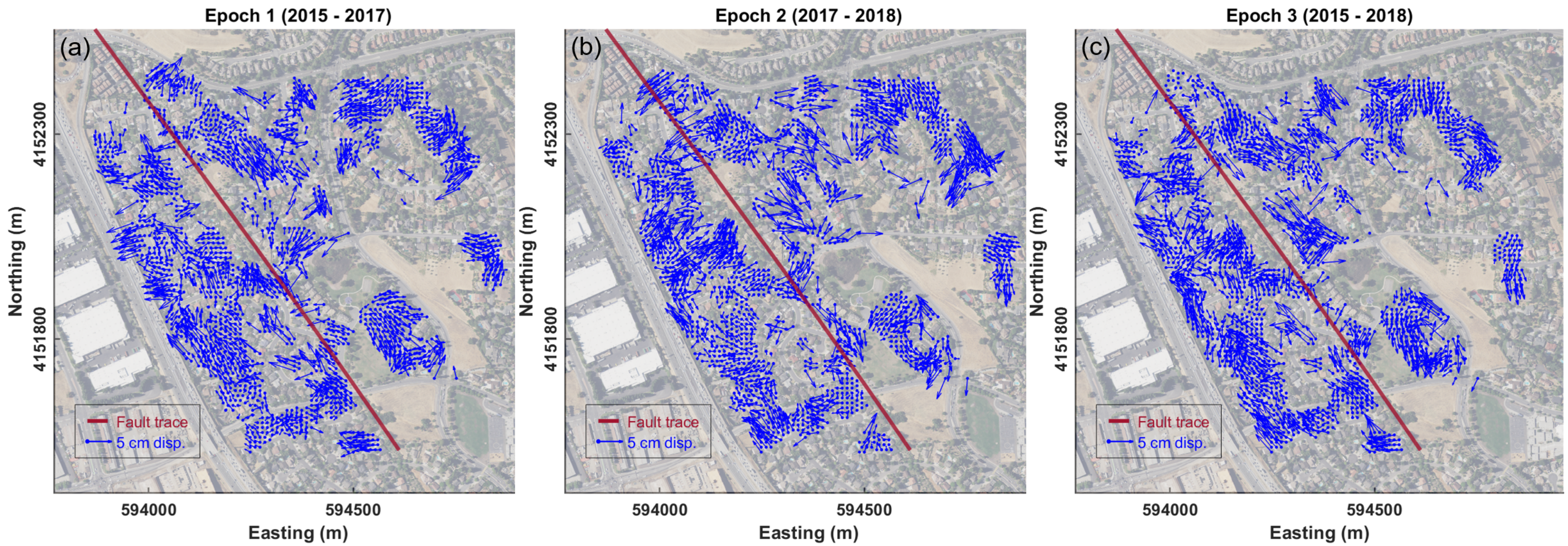

Figure 6.4 Displacement fields from the lidar time series. Each epoch represents a bi-temporal change cycle, and the displacement in epoch 3 is reversed showing changes from 2015 to 2018. Blue arrows indicate the locations and magnitudes of the displacement vectors. The red line indicates the local fault trace interpolated from field observation.

6.4.2 Detected off-fault displacement

The off-fault displacement distribution displaced in Figure 6.5 represents the variation in the two orthogonal components of the displacement vectors projected onto the local fault trace for the entire study area. The trace is interpolated by field observations [10] and manually confirmed via a RTK survey. The off-fault displacement profiles in (a) show the variation of ground displacement versus off-fault distance, and shading indicates standard deviation of the change within 50 m. Relative displacement profiles since 2015 (epoch 1 and 3) are shown in (b). Collocated and nearby alinement array stations (HPIN, HCAM. HPMD and HSGR) and creepmeters (CFW1) observations, with locations shown in Figure 6.1, are plotted as squares for epoch 1 and triangles for epoch 3 at the fault right. Observations are normalized by off-fault displacements observed at -100 ± 50 m on the left fault plane for a relative comparison.

6.4.3 Dependencies of the estimates

The quality of the least squares adjustment can be assessed by checking the correlation between the estimated unknowns. Decorrelation between the two groups of unknowns, namely the deformation unknowns and the planar unknowns, is a good indication of robust regression. For fault creep, it may be unnecessary to regress for angular change in the rigid body transformation. This is because minor local rotation is not expected at the scale of a plane, or in other words, ground surface fault creep is unlikely to generate a high strain to induce local rotation of a single house. Figure 6.6 shows that high correlation exists between the regressed angular change and the plane normal estimates when both displacement and rotation are estimated. The unknown $def.$ in (a) consists of three-axis translation and three small angle rotations. Circled area highlights a high correlation between the rotation angles and planar normals where darker color indicates higher correlation. Therefore, we chose to not estimate the angular change and focus on estimating translation only.

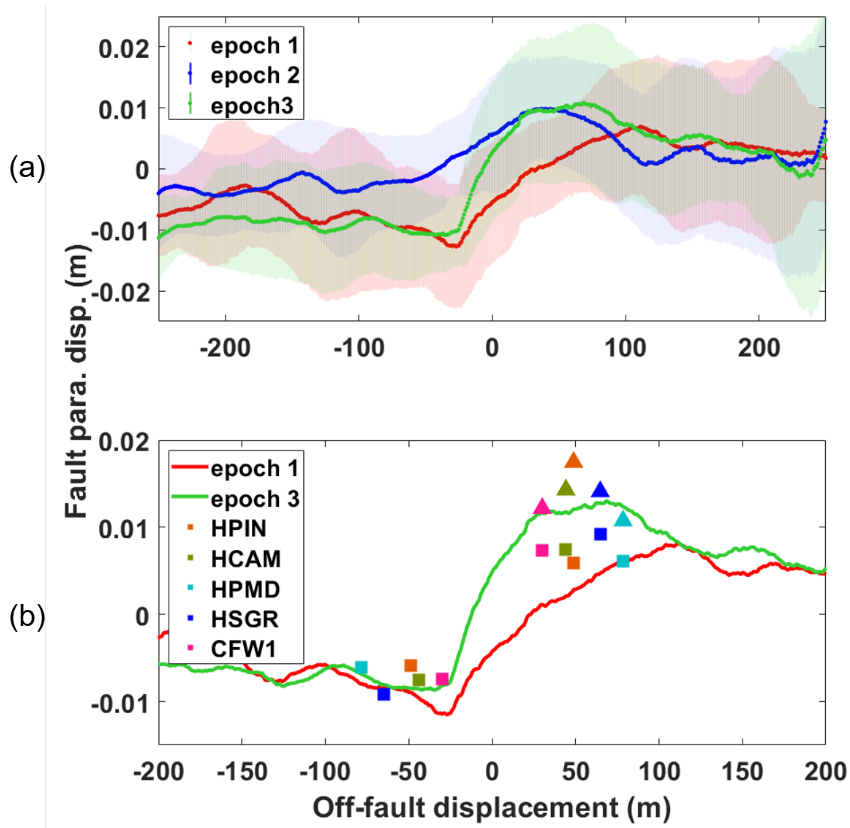

Figure 6.5 Off-fault displacement profile for the lidar time series. Change detected in the third epoch (2018-2015) is reversed for consistency. (a) Fault parallel displacement versus off-fault distance. (b) Relative displacement profiles since 2015.

Without the estimation of angular change, the correlation matrix is block-diagonal and dominated by minor correlation between the displacement unknowns and the plane normal unknowns subject to the constraints given in Equation 6.2.

6.5 Validation of the change detection results

6.5.1 Precision of the change detection

To quantify the precision of our method, we use synthesized displaced point clouds with the change detection framework. The test data are segmented from an area of 600 by 300 meters. Synthesized displacements were applied to randomly selected subsets of the test dataset to represent post-deformed point clouds. The random subset mimics the

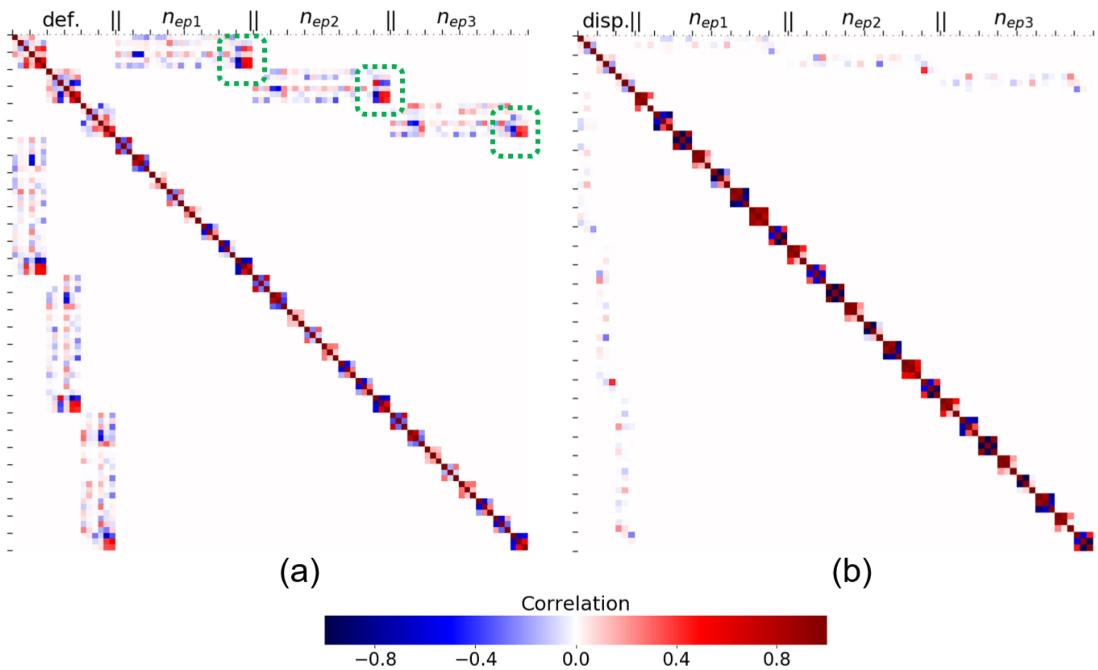

Figure 6.6 Significance of estimating angular change by comparing the correlation between the estimated unknowns. (a) Correlation of unknowns with angular change. (b) Correlation of unknowns without angular change, only translation is estimated.

irregular format of a point cloud with fuzzy correspondence between the reference and secondary points. The test showcases a theoretical estimate of precision given that occlusions and variations between independent scans are not simulated.

Thirty random displacements series were synthesized from normal distributions of 1.5 ± 1 cm and 0.75 ± 1 cm respectively, representing a comparable amount of displacements to the first and second epochs of fault creep as observed by creepmeter measurements. The third/last epoch compensates for the accumulated displacements of the entire time series. The direction of the displacement is randomly generated with a uniform distribution from $0°$ to $360°$. Vertical displacements were generated from a normal distributions of 0 ± 1 cm. The validation uses residuals of the recovered displacement as its metric, and the results are compared with the state-of-the-art Iterative Closest Point (ICP) point-to-point and point-to-plane registration algorithms [90, 93, 165, 168] which has been shown to give only cm-dm level accuracy in fault displacement detection [12].

Table 6.1 Comparison of three change detection methods: ICP-point to point, ICP-point to plane, and our method.

Method	Average over all epochs (standard deviation in brackets)		
Unit(mm)	$\overline{dX}$	$\overline{dY}$	$\overline{dZ}$
ICP-p2p	-3.74 (107.74)	3.73 (95.85)	2.89 (29.39)
ICP-p2pl	-0.24 (107.06)	0.57 (97.24)	0.93 (49.77)
Ours	-0.01 (0.65)	-0.00 (0.69)	-0.00 (1.06)

Table 6.1 displays the precision results. The table shows no bias in the planar change detection estimates as the mean of the residuals of the recovered displacement is close to zero. Our method performs better than both ICP methods with smaller bias and variation in the recovered residuals. The benefit of modeling point clouds as geometric primitives is validated here as the modeling process generates more stable correspondence between coincident features within a bi-temporal change detection; this is even true in the presence of occlusions.

The consistency of the time series detection can be quantified by calculating the misclosure of the displacement loop as shown in Figure 6.3. The misclosure quantifies the consistency of the change detection such that the change detected from every epoch converges and is equal to the overall displacement detected using the first and last observation, i.e. $\sum_{i=1}^{m} \boldsymbol{disp_i} = 0$. As shown in Table 6.2, our method clearly performs better than ICP, and clearly shows the benefit of the additional geometric and temporal constraints described by equation 6.2. Our method not only gives a consistent estimate of the displacement time series, but the variation of the estimates over time is significantly smaller than the two ICP results.

The above evaluation provides an estimate of the precision of the change detection under theoretical conditions because the data is 'perfect' without any occlusions. In reality, repeated MLS scans are full of mismatches due to variations within the scan. As

Table 6.2 Misclosure of the displacement time series.

Method	Displacement misclosure (standard deviation in brackets)		
Unit(mm)	$\overline{dX}$	$\overline{dY}$	$\overline{dZ}$
ICP-p2p	-11.36 (14.21)	10.93 (12.72)	7.47 (21.52)
ICP-p2pl	-0.81 (2.28)	1.64 (2.38)	-4.19 (70.71)
Ours	-0.02 (0.06)	-0.00 (0.12)	0.01 (0.21)

more stable feature correspondence can be associated by modeling point clouds as primitives, our method provides even better results compared with ICP with the presence of scan occlusions.

6.5.2 Accuracy assessment - validation with other geodetic measurements and the effect of data pre-alignment

The accuracy of change detection is dependent upon the quality of the data pre-alignment during pre-processing. Misaligned data can impose a constant displacement bias on the final results which is at the scale of the uncertainties in the pre-alignment registration. Displacements smaller than this bias could therefore be masked. An example of such a scenario is shown in the second epoch of the detected displacement series in Figure 6.4 (b). Despite using either ICP or primitive-based pre-alignment methods, the dextral pattern in the second epoch is not clear, the results are dominated by a trend of misalignment that has a size comparable to the real displacement. In reality, according to creepmeter measurements (Figure 6.1), the real dextral displacement is about 0.75 cm at 30 m off-fault for this epoch; this is impossible to resolve given that the pre-alignment error is also at the cm level.

The existence of pre-alignment errors makes it hard to resolve absolute changes at levels better than the uncertainties of registration. However, it is still possible to observe relative off-fault displacement by examing the aligned displacement profile. Figure 6.5 (b) shows the off-fault displacement profile and measurements of collocated alinement array stations and a nearby creepmeter where the off-fault displacement is calculated relative to a stable location -100 ± 50 m on the left side of the fault. This location is manually chosen such that alinement array stations and creepmeter observations are centered at zero for displacements observed in the first epoch (2015-2017). The profile validates the MLS measurements because the nearby geodetic observations agree with measurements from the displacement profile at the level of uncertainty of the alinement array observations.

Table 6.3 Validations of off-fault displacements detected from MLS versus alinement array observations at station HCAM (measurement uncertainty (1σ) is reported in brackets).

	Obs. time	Displacement (mm)
HCAM	10/05/15-10/29/17	15.0 (0.7)
	10/29/17-10/28/18	6.8 (0.5)
	10/05/15-10/28/18	21.8 (0.9)
MLS	07/01/15-06/01/17	15.0 (5.2)
	06/01/17-08/01/18	7.7 (8.7)
	07/01/15-08/01/18	21.1 (9.7)

To validate the detected off-fault displacement, observations at alinement array station HCAM is compared against MLS estimates. The alinement array has a baseline of 88.35 m. Collocated MLS observations within a search window of $20 m^2$ are compared with alinement array observations collected from 2015 to 2018. The comparison shown in Table 6.3 indicates a good agreement between the two observations.

The rest of the alinement array stations (HPIN, HPMD and HSGR) are either not located within the MLS survey area or do not have full MLS data coverage. To compare with them, the search window has to be extended along the fault such that all MLS measurements along the fault within a 25 m search window are compared. Alinement array stations HPIN, HPMD and HSGR have a baseline length of 97.65, 156.91 and 129.54 m respectively. Despite the larger detection variance due to the extended search window, the comparison results indicate a positive correlation between alinement array measurements and MLS observations, as shown in Table 6.4.

Table 6.4 Validations of off-fault displacements detected from MLS versus alinement array observations at station HPIN, HPMD and HSGR (measurement uncertainty (1σ) is reported in brackets).

	Obs. time	Displacement (mm)
HPIN	09/26/15-10/28/17	11.8 (0.6)
	10/28/17-10/21/18	11.6 (0.7)
	09/26/15-10/21/18	23.4 (0.9)
MLS	07/01/15-06/01/17	10.9 (12.2)
	06/01/17-08/01/18	11.3 (11.5)
	07/01/15-08/01/18	20.3 (13.6)
HPMD	10/05/15-10/29/17	12.2 (0.4)
	10/29/17-10/28/18	4.7 (0.4)
	10/05/15-10/28/18	16.9 (0.6)
MLS	07/01/15-06/01/17	14.4 (13.8)
	06/01/17-08/01/18	9.3 (12.7)
	07/01/15-08/01/18	19.4 (16.2)
HSGR	10/05/15-10/29/17	18.4 (0.7)
	10/29/17-10/21/18	4.9 (0.5)
	10/05/15-10/21/18	23.3 (0.9)
MLS	07/01/15-06/01/17	13.7 (11.6)
	06/01/17-08/01/18	10.5 (11.6)
	07/01/15-08/01/18	21.2 (15.2)

6.6 Conclusions

As lidar gains in popularity and repeated lidar collections becomes more feasible, the framework we have proposed fills the void for change detection for lidar time series. The proposed framework leverages persistent planar primitives extracted from multi-temporal point clouds using our corresponding primitive detector. Beyond a chain of bi-temporal least squares regressions for change detection, the proposed multi-temporal framework is constrained with additional displacement and geometric constraints to ensure temporal and spatial consistency within the lidar time series. Compared with state-of-the-art ICP change detection, the proposed method outperforms both point-to-point and point-to-plane ICP in the synthetic tests of bi-temporal change by an order of magnitude. In addition, our method shows consistent detection results as displacement misclosure minimizes to zero for the processed time series. The proposed method can also be used to finely register multiple point clouds at the same time. The correlation between the adjusted parameters was discussed to choose the proper solution set for the unknowns by examining parameter correlation. The method was tested using synthetic displacements on real datasets, and the performance is validated in a case study of fault creep time-series detection for a 2 km segment of the Hayward fault. Compared with collocated alinement array measurements, the detection results agree with alinement array time series at the sub-centimeter level. Results show $15 \pm 5.2mm$, $7.7 \pm 8.7mm$ and $21.1 \pm 9.7mm$ fault parallel displacements detected at 44 m from the fault trace for periods from 2015-2017, 2017-2018 and 2015-2018 respectively. For future work, we plan to extend the type of primitives modeled beyond planes such that other stable features can be extracted and tracked for change, and incorporate estimates of unknowns beyond ground displacement.

Chapter 7

Conclusions and recommended future research directions

This dissertation described a change detection framework using MLS observations to resolve distributed ground displacement in the near field with high accuracy. Using the geometric primitives modeled from MLS point clouds, change detection revealed non-linear ground displacement in the near field at an unprecedented resolution. To summarize, we conclude our findings and recommend future research directions from three perspectives: (1) MLS point cloud manipulation and geometric primitives modeling, (2) regression analysis of the change detection, and (3) applications of displacement detection in the near field for earthquake fault.

7.1 Point cloud manipulation and geometric primitives modeling

Change detection requires tracking the location of corresponding features from repeated MLS observations. Therefore, an essential step is to process the point cloud and convert its irregular representation into features that can be temporally tracked. We have shown that geometric primitives provide a robust representation of locations for tracking temporally spaced primitives. We have implemented a deep learning method for cylindrical point cloud segmentation using PointNet (Chapter 4). Over 1300 vine rows and 2600 anchor posts were extracted from MLS scans of a Napa vineyard for change detection of co- and post-seismic displacements. We have built methods for a customized random sample consensus (RANSAC) for planar points extraction. The proposed sequential corr-planar RANSAC is capable of detecting multiple primitives at a single query location (Chapter 5), and a two-step variant is capable of compensating for temporal variations of MLS observations collected from multiple epochs (Chapter 6). Around 2000 coincide planar surfaces are extracted from MLS scan of a $1km^2$ urban neighborhood for change detection of fault creep. Future research is recommended to examine using other types of primitives and a better assessment of primitive correspondence via approaches like deep learning and other non-primitive point cloud descriptors.

7.2 Regression framework used in the change detection

To quantify displacements, the regression framework is the core of change detection. We have described an intrinsic least squares solution for single cylindrical primitives (Chapter 4), a combined least squares solution for augmented planar primitives (Chapter 5), and a multi-temporal combined least squares solution for a time series of augmented planar primitives (Chapter 6). These regression frameworks are hierarchical, as the regression for a single primitive lays the foundation for primitive modeling, the combined regression enables simultaneous modeling and change detection, and finally, the multi-temporal regression combines multiple regressions with additional constraints on both temporal and spatial consistency. The evolution of the regression framework denotes the geometry of MLS point clouds being represented at various feature levels such that the change can be resolved in its non-linear form and estimated for its variation over time. The nonlinear least squares framework leaves a general formula for change detection applications with geometric point cloud constraints. We have proposed an independent measurement of the strength of the least squares solution called geometric strength of the translation (GSTR) to optimize aggregation geometry while obtaining the highest spatial resolution for change detection. The experiment shows that $GSTR \approx 2$ for a twelve-plane solution best fits the change detection for MLS data collected for the Hayward fault (Chapter 5 and 6). Future work is recommended to investigate using other types of conditions and constraints that better suit the physical process of the change. The general formula for regression constrained by point cloud geometry can be used for applications beyond change detection, for example updating hi-resolution lidar maps and the localization and calibration of lidar sensors in a dynamic surveying environment.

7.3 Applications of displacement detection in the near field

We have provided three case studies for fault displacement estimation in the near field using the proposed change detection framework. Previous geodetic observations and associated change detection methods that have been used to observe ground displacements are compared in a literature review (Chapter 1- 3). It has been shown that lidar has the benefit of providing high-resolution and robust estimation of ground displacements compared with other geodetic measurements. We have shown the motivation for creating a change detection framework to processing lidar point clouds collected in the near field of a fault. Our case studies cover full fault cycles during the co-seismic, post-seismic, and inter-seismic periods. The proposed method has the flexibility to detect change at various spatial ranges. The change detection results revealed decimeter-level co-seismic and centimeter-level post-seismic fault displacement for the 2014 Mw 6.0 South Napa Earthquake (Chapter 4). The fault trace was detected from dextral co-seismic displacement and off-fault displacement profiles were detected which highlight nonlinear displacement in the near field. Centimeter-level fault creep displacements were detected along a 2 km segment of the Hayward fault (Chapter 5). A series of off-fault displacement profiles were detected along the fault trace direction and throughout the entire survey area. Multi-temporal MLS time series were studied for the Hayward fault creep from MLS data collected in 2015, 2017 and 2018 (Chapter 6). The high definition change detection results reveal fields of displacement and recover nonlinear deformation patterns in the near field; these have not been observed to date by other geodetic measurements.

We have evaluated the performance of MLS observations for change detection using synthetic displacement tests and validation datasets collected by other geodetic measurements. With validation and synthetic tests, we have shown the precision of the detection and analyzed the potential of smoothing effects due to moving window detection (Chapter 5). We have also provided a strategy to detect change on an arbitrary query grid with an adaptive search window (Chapter 6) which benefits later analyses of fault dynamics. The improved framework enables multiple coincident MLS observations to be processed as a time series of displacements. Using synthetic (Chapter 3) and real (Chapter 6) MLS datasets, we have compared our change detection framework with the state-of-the-art Iterative Closest Point (ICP) methods using simulated displacements. The results show that our method performs better than ICP point-to-point and point-to-plane variants and provides better change detection precision in experiments of recovering simulated displacements by an order of magnitude. The proposed change detection framework also provides temporal consistency in the multi-temporal change detection experiment which is not found in ICP bi-temporal results.

Results from the change detection revealed 25 cm accumulated co-seismic and early post-seismic offsets from MLS observation collected 7 days after the 2014 Mw 6.0 South Napa earthquake. Results shows 3-4 cm post-seismic displacement observed between 7 and 34 days after the earthquake and indicates that the off fault displacement reaches its maximum at approximately 25 m from the estimated fault trace. At the Hayward fault, 1.1 ± 0.7 cm (1σ) dextral displacement was detected using MLS data collected from July 2015 to June 2017 while the collocated alinement array reports 1.5 ± 0.7 cm displacement from Oct. 2015 to Oct. 2017. The baseline of the alinement array at station HCAM is shown to be not long enough to span the entire nonlinear creeping zone by examining displacement profiles detected from MLS data. This deficiency of the alinement array baseline indicates an underestimation of the creep displacements monitored at this location and possibly at other locations using alinement array observations. A time series of ground displacements was estimated using repeated MLS observation for the Hayward fault. Results show $15 \pm 5.2\,mm$, $7.7 \pm 8.7\,mm$ and $21.1 \pm 9.7\,mm$ fault parallel displacements detected at 44 m from the fault trace detected for periods from 2015-2017, 2017-2018 and 2015-2018 respectively, and the results agree with collocated alinement array observations at the sub-centimeter level.

Future interpretation of the change detection results may contribute to the study of the fault slip reduction and the relationship of ground displacement with fault slip at depth. Cross validations can be conducted in the far field using measurements from InSAR and other geodetic measurements. A fusion of observations from multiple geodetic measurements (e.g. InSAR, lidar, GNSS, etc.) is recommended for change detection of fault displacement in general to optimize the resolution of detection in the near field and the coverage of detection in the far field.

References

[1] Johanna Nevitt. Workshop: Rupture and fault zone observatory (rufzo). `https://www.scec.org/workshops/2021/rufzo`. [Online; accessed 19-August-2021].

[2] Harry Fielding Reid. The mechanics of the earthquake. *The California Earthquake of April 18, 1906, Report of the State Investigation Commission*, 2:16–28, 1910.

[3] Rémi Michel and Jean-Philippe Avouac. Coseismic surface deformation from air photos: The kickapoo step over in the 1992 landers rupture. *Journal of Geophysical Research: Solid Earth*, 111(B3), 2006.

[4] D Roten, KB Olsen, and SM Day. Off-fault deformations and shallow slip deficit from dynamic rupture simulations with fault zone plasticity. *Geophysical Research Letters*, 44(15):7733–7742, 2017.

[5] Johanna M Nevitt, Benjamin A Brooks, Rufus D Catchings, Mark R Goldman, Todd L Ericksen, and Craig L Glennie. Mechanics of near-field deformation during co-and post-seismic shallow fault slip. *Scientific Reports*, 10(1):1–13, 2020.

[6] Benjamin A Brooks, Sarah E Minson, Craig L Glennie, Johanna M Nevitt, Tim Dawson, Ron Rubin, Todd L Ericksen, David Lockner, Kenneth Hudnut, Victoria Langenheim, Andrew Lutzmaxime, Maxime Mareschal, Jessica Murray, David Schwartz, and Dana Zaccone. Buried shallow fault slip from the south napa earthquake revealed by near-field geodesy. *Science advances*, 3(7):e1700525, 2017.

[7] Adrian Borsa and Jean-Bernard Minster. Rapid determination of near-fault earthquake deformation using differential lidar. *Bulletin of the Seismological Society of America*, 102(4):1335–1347, 2012.

[8] Xiao Zhang. *LiDAR-Based Change Detection for Earthquake Surface Ruptures*. PhD thesis, 2016.

[9] Chuck DeMets. Earthquakes and the seismic cycle. `http://geoscience.wisc.edu/~chuck/Classes/Mtn_and_Plates/eq_cycle.html`. [Online; accessed 19-August-2021].

[10] Jon Galehouse, John Caskey, and students from San Francisco State University. SFSU creep project homepage. http://funnel.sfsu.edu/creep/, accessed: 10/15/2021.

[11] Forrest S McFarland, James J Lienkaemper, and S John Caskey. *Data from theodolite measurements of creep rates on San Francisco Bay region faults, California, 1979-2009*. US Geological Survey Reston, VA, 2009.

[12] Nima Ekhtari and Craig Glennie. High-resolution mapping of near-field deformation with airborne earth observation data, a comparison study. *IEEE Transactions on Geoscience and Remote Sensing*, 56(3):1598–1614, 2017.

[13] Edwin Nissen, Tadashi Maruyama, J Ramon Arrowsmith, John R Elliott, Aravindhan K Krishnan, Michael E Oskin, and Srikanth Saripalli. Coseismic fault zone deformation revealed with differential lidar: Examples from japanese mw 7 intraplate earthquakes. *Earth and Planetary Science Letters*, 405:244–256, 2014.

[14] Juan Carlos Fernandez-Diaz, William E Carter, Ramesh L Shrestha, and Craig L Glennie. Now you see it… now you don't: Understanding airborne mapping lidar collection and data product generation for archaeological research in mesoamerica. *Remote Sensing*, 6(10):9951–10001, 2014.

[15] Frank Crow. The origins of the teapot. *IEEE Computer Graphics and Applications*, 7(1):8–19, 1987.

[16] David R Streutker, Nancy F Glenn, and Rupesh Shrestha. A slope-based method for matching elevation surfaces. *Photogrammetric Engineering & Remote Sensing*, 77 (7):743–750, 2011.

[17] Thomas K Rockwell, Scott Lindvall, Tim Dawson, Rob Langridge, William Lettis, and Yann Klinger. Lateral offsets on surveyed cultural features resulting from the 1999 izmit and duzce earthquakes, turkey. *Bulletin of the Seismological Society of America*, 92(1):79–94, 2002.

[18] Charles R Qi, Hao Su, Kaichun Mo, and Leonidas J Guibas. Pointnet: Deep learning on point sets for 3d classification and segmentation. In *Proceedings of the IEEE conference on computer vision and pattern recognition*, pages 652–660, 2017.

[19] Kenneth Watkins Hudnut, Thomas M Brocher, Carol S Prentice, John Boatwright, Benjamin A Brooks, Brad T Aagaard, James Luke Blair, J Fletcher, Jemile E Erdem, Charles W Wicks, Jessica R Murray, Fred F Pollitz, John Langbein, Jerry Svarc, David P Schwartz, Daniel J Ponti, Suzanne Hecker, Stephen DeLong, Carla Rosa, Brenda Jones, Rynn Lamb, Anne M Rosinski, Timothy P McCrink, Timothy E Dawson, Gordon Seitz, Ron S Rubin, Craig L Glennie, Darren Hauser, Todd Ericksen, Dan Mardock, Don F Hoirup, and Jonathan D Bray. *Key recovery factors for the August 24, 2014, South Napa earthquake*. US Department of the Interior, US Geological Survey, 2014.

[20] Aerial Photography Field USDA-FSA-APFO. Naip digital georectified image. 2019.

[21] CloudCompare. CloudCompare (version 2.8). https://www.cloudcompare.org/, accessed: 04/02/2022.

[22] William HK Lee, FT Wu, and Carl Jacobsen. A catalog of historical earthquakes in china compiled from recent chinese publications. *Bulletin of the Seismological Society of America*, 66(6):2003–2016, 1976.

[23] Lisa Wald. The science of earthquakes. `https://www.usgs.gov/natural-hazards/earthquake-hazards/science/science-earthquakes?`

qt-science_center_objects=0#qt-science_center_objects. [Online; accessed 19-August-2021].

[24] L Prawirodirdjo, Y Bock, JF Genrich, SSO Puntodewo, J Rais, C Subarya, and S Sutisna. One century of tectonic deformation along the sumatran fault from triangulation and gps surveys. 2000.

[25] Grove Karl Gilbert. A theory of the earthquakes of the great basin, with a practical application. *American Journal of Science*, 3(157):49–53, 1884.

[26] Paul Segall. *Earthquake and volcano deformation*. Princeton University Press, 2010.

[27] Shimon Wdowinski, Yehuda Bock, Jie Zhang, Peng Fang, and Joachim Genrich. Southern california permanent gps geodetic array: Spatial filtering of daily positions for estimating coseismic and postseismic displacements induced by the 1992 landers earthquake. *Journal of Geophysical Research: Solid Earth*, 102(B8):18057–18070, 1997.

[28] Hiromichi Tsuji, Yuki Hatanaka, Takeshi Sagiya, and Manabu Hashimoto. Coseismic crustal deformation from the 1994 hokkaido-toho-oki earthquake monitored by a nationwide continuous gps array in japan. *Geophysical Research Letters*, 22(13): 1669–1672, 1995.

[29] RE Reilinger, S Ergintav, R Bürgmann, S McClusky, O Lenk, A Barka, O Gurkan, L Hearn, KL Feigl, R Cakmak, B Aktug, H Ozener, and M N Töksoz. Coseismic and postseismic fault slip for the 17 august 1999, m= 7.5, izmit, turkey earthquake. *Science*, 289(5484):1519–1524, 2000.

[30] Roland Bürgmann, Dominic Schmidt, RM Nadeau, M d'Alessio, E Fielding, D Manaker, TV McEvilly, and MH Murray. Earthquake potential along the northern hayward fault, california. *Science*, 289(5482):1178–1182, 2000.

[31] Stéphane Mazzotti, Xavier Le Pichon, Pierre Henry, and Shin-Ichi Miyazaki. Full interseismic locking of the nankai and japan-west kurile subduction zones: An analysis of uniform elastic strain accumulation in japan constrained by permanent gps. *Journal of Geophysical Research: Solid Earth*, 105(B6):13159–13177, 2000.

[32] Edward H Field, Ramon J Arrowsmith, Glenn P Biasi, Peter Bird, Timothy E Dawson, Karen R Felzer, David D Jackson, Kaj M Johnson, Thomas H Jordan, Christopher Madden, Andrew J others Michael, Kevin R Milner, Morgan T Page, Tom Parsons, Peter M Powers, Bruce E Shaw, Wayne R Thatcher, Ray J Weldon II, Yuehua Zeng, and Working Group on California Earthquake Probabilities. Uniform california earthquake rupture forecast, version 3 (ucerf3)—the time-independent model. *Bulletin of the Seismological Society of America*, 104(3):1122–1180, 2014.

[33] Ryan D Gold, Nadine G Reitman, Richard W Briggs, William D Barnhart, Gavin P Hayes, and Earl Wilson. On-and off-fault deformation associated with the september 2013 mw 7.7 balochistan earthquake: Implications for geologic slip rate measurements. *Tectonophysics*, 660:65–78, 2015.

[34] François Ayoub, Sébastien Leprince, and Jean-Philippe Avouac. Co-registration and correlation of aerial photographs for ground deformation measurements. *ISPRS Journal of Photogrammetry and Remote Sensing*, 64(6):551–560, 2009.

[35] Y Kaneko and Y Fialko. Shallow slip deficit due to large strike-slip earthquakes in dynamic rupture simulations with elasto-plastic off-fault response. *Geophysical Journal International*, 186(3):1389–1403, 2011.

[36] JC Savage and RO Burford. Geodetic determination of relative plate motion in central california. *Journal of Geophysical Research*, 78(5):832–845, 1973.

[37] Zhenyu Zou, Zaisen Jiang, Yueju Cui, Long Zhang, Peng Wang, and Tai Liu. Study

on the layout of gnss sites for strike-slip faults. *Geophysical Journal International*, 219(2):1131–1137, 2019.

[38] Yoshimitsu Okada. Internal deformation due to shear and tensile faults in a half-space. *Bulletin of the seismological society of America*, 82(2):1018–1040, 1992.

[39] Christopher WD Milliner, James F Dolan, James Hollingsworth, Sebastien Leprince, Francois Ayoub, and Charles G Sammis. Quantifying near-field and off-fault deformation patterns of the 1992 mw 7.3 landers earthquake. *Geochemistry, Geophysics, Geosystems*, 16(5):1577–1598, 2015.

[40] Ping He, Yangmao Wen, Caijun Xu, and Yunguo Chen. Complete three-dimensional near-field surface displacements from imaging geodesy techniques applied to the 2016 kumamoto earthquake. *Remote Sensing of Environment*, 232:111321, 2019.

[41] Ziyadin Cakir, Jean-Bernard de Chabalier, Rolando Armijo, Bertrand Meyer, Aykut Barka, and Gilles Peltzer. Coseismic and early post-seismic slip associated with the 1999 izmit earthquake (turkey), from sar interferometry and tectonic field observations. *Geophysical Journal International*, 155(1):93–110, 2003.

[42] Rémi Michel, Jean-Philippe Avouac, and Jean Taboury. Measuring ground displacements from sar amplitude images: Application to the landers earthquake. *Geophysical Research Letters*, 26(7):875–878, 1999.

[43] Chelsea P. Scott, J Ramon Arrowsmith, Edwin Nissen, Lia Lajoie, Tadashi Maruyama, and Tatsuro Chiba. The m7 2016 kumamoto, japan, earthquake: 3-d deformation along the fault and within the damage zone constrained from differential lidar topography. *Journal of Geophysical Research: Solid Earth*, 123 (7):6138–6155, 2018. doi: https://doi.org/10.1029/2018JB015581. URL `https://agupubs.onlinelibrary.wiley.com/doi/abs/10.1029/2018JB015581`.

[44] Rémi Michel, Jean-Philippe Avouac, and Jean Taboury. Measuring near field coseismic displacements from sar images: Application to the landers earthquake. *Geophysical Research Letters*, 26(19):3017–3020, 1999.

[45] Stephen B DeLong, Andrea Donnellan, Daniel J Ponti, Ron S Rubin, James J Lienkaemper, Carol S Prentice, Timothy E Dawson, Gordon Seitz, David P Schwartz, Kenneth W Hudnut, Carla Rosa, Alexandra Pickering, and Jay W Parker. Tearing the terroir: Details and implications of surface rupture and deformation from the 24 august 2014 m6. 0 south napa earthquake, california. *Earth and Space Science*, 3(10):416–430, 2016.

[46] Chelsea Scott, Johann Champenois, Yann Klinger, Edwin Nissen, Tadashi Maruyama, Tatsuro Chiba, and Ramon Arrowsmith. The 2016 m7 kumamoto, japan, earthquake slip field derived from a joint inversion of differential lidar topography, optical correlation, and insar surface displacements. *Geophysical Research Letters*, 46(12):6341–6351, 2019.

[47] Chelsea Phipps Scott, Stephen B DeLong, and J Ramón Arrowsmith. Distribution of aseismic deformation along the central san andreas and calaveras faults from differencing repeat airborne lidar. *Geophysical Research Letters*, 47(22): e2020GL090628, 2020.

[48] Xiao Zhang, Craig Glennie, and Arpan Kusari. Change detection from differential airborne lidar using a weighted anisotropic iterative closest point algorithm. *IEEE Journal of Selected Topics in Applied Earth Observations and Remote Sensing*, 8(7): 3338–3346, 2015.

[49] Arpan Kusari, Craig L Glennie, Benjamin A Brooks, and Todd Ericksen. Precise registration of laser mapping data by planar feature extraction for deformation monitoring. *IEEE Trans. Geosci. Remote. Sens.*, 57(6):3404–3422, 2019.

[50] Craig Glennie. Imaging near-fault earthquake deformation with integrated sar, lidar, and optical measurements.

[51] Ashbindu Singh. Review article digital change detection techniques using remotely-sensed data. *International journal of remote sensing*, 10(6):989–1003, 1989.

[52] Yehuda Ben-Zion, Bob Busby, Kasey Aderhold, Robert Busby, Rebecca Bendick, Frank Vernon, and Tran Huynh. SCEC-IRIS-UNAVCO community workshop: Rupture and fault zone observatory (rufzo). https://www.scec.org/workshops/2021/rufzo, accessed: 04/01/2022.

[53] J Bray, J Cohen-Waeber, T Dawson, T Kishida, and N Sitar. Geotechnical engineering reconnaissance of the august 24, 2014 m6 south napa earthquake. *Geotechnical Extreme Events Reconnaissance (GEER) Association Report Number GEER*, 37, 2014.

[54] Michael E Oskin, J Ramon Arrowsmith, Alejandro Hinojosa Corona, Austin J Elliott, John M Fletcher, Eric J Fielding, Peter O Gold, J Javier Gonzalez Garcia, Ken W Hudnut, Jing Liu-Zeng, and Orlando J Teran. Near-field deformation from the el mayor–cucapah earthquake revealed by differential lidar. *Science*, 335(6069): 702–705, 2012.

[55] Yuri Fialko, David Sandwell, Mark Simons, and Paul Rosen. Three-dimensional deformation caused by the bam, iran, earthquake and the origin of shallow slip deficit. *Nature*, 435(7040):295–299, 2005.

[56] Pierre Bettinelli, Jean-Philippe Avouac, Mireille Flouzat, François Jouanne, Laurent Bollinger, Pascal Willis, and Gyani Raja Chitrakar. Plate motion of india and interseismic strain in the nepal himalaya from gps and doris measurements. *Journal of Geodesy*, 80(8):567–589, 2006.

[57] Corné Kreemer, Geoffrey Blewitt, and Elliot C Klein. A geodetic plate motion and global strain rate model. *Geochemistry, Geophysics, Geosystems*, 15(10):3849–3889, 2014.

[58] Linette Prawirodirdjo and Yehuda Bock. Instantaneous global plate motion model from 12 years of continuous gps observations. *Journal of Geophysical Research: Solid Earth*, 109(B8), 2004.

[59] James J Lienkaemper, Forrest S McFarland, Robert W Simpson, and S John Caskey. Using surface creep rate to infer fraction locked for sections of the san andreas fault system in northern california from alignment array and gps data. *Bulletin of the Seismological Society of America*, 104(6):3094–3114, 2014.

[60] Mark Simons, Yuri Fialko, and Luis Rivera. Coseismic deformation from the 1999 m w 7.1 hector mine, california, earthquake as inferred from insar and gps observations. *Bulletin of the Seismological Society of America*, 92(4):1390–1402, 2002.

[61] James J Lienkaemper, Stephen B DeLong, Carolyn J Domrose, and Carla M Rosa. Afterslip behavior following the 2014 m 6.0 south napa earthquake with implications for afterslip forecasting on other seismogenic faults. *Seismological Research Letters*, 87(3):609–619, 2016.

[62] Ronald Newbold Bracewell and Ronald N Bracewell. *The Fourier transform and its applications*, volume 31999. McGraw-Hill New York, 1986.

[63] Paul E Anuta. Spatial registration of multispectral and multitemporal digital imagery using fast fourier transform techniques. *IEEE transactions on Geoscience Electronics*, 8(4):353–368, 1970.

[64] Bing Pan. Recent progress in digital image correlation. *Experimental mechanics*, 51 (7):1223–1235, 2011.

[65] Manuel Guizar-Sicairos, Samuel T Thurman, and James R Fienup. Efficient subpixel image registration algorithms. *Optics letters*, 33(2):156–158, 2008.

[66] Robert E Crippen. Measurement of subresolution terrain displacements using spot panchromatic imagery. *Episodes Journal of International Geoscience*, 15(1):56–61, 1992.

[67] J Yang and K Bhattacharya. Augmented lagrangian digital image correlation. *Experimental Mechanics*, 59(2):187–205, 2019.

[68] Sébastien Leprince, François Ayoub, Yann Klinger, and Jean-Philippe Avouac. Co-registration of optically sensed images and correlation (cosi-corr): An operational methodology for ground deformation measurements. In *2007 IEEE International Geoscience and Remote Sensing Symposium*, pages 1943–1946. IEEE, 2007.

[69] Stéphane Dominguez, Jean-Philippe Avouac, and Rémi Michel. Horizontal coseismic deformation of the 1999 chi-chi earthquake measured from spot satellite images: Implications for the seismic cycle along the western foothills of central taiwan. *Journal of Geophysical Research: Solid Earth*, 108(B2), 2003.

[70] Carlo Marin, Francesca Bovolo, and Lorenzo Bruzzone. Building change detection in multitemporal very high resolution sar images. *IEEE transactions on geoscience and remote sensing*, 53(5):2664–2682, 2014.

[71] Tobias Ullmann, Christian Büdel, Roland Baumhauer, and Majid Padashi. Sentinel-1 sar data revealing fluvial morphodynamics in damghan (iran): Amplitude and coherence change detection. *Int. J. Earth Sci. Geophys*, 2(7), 2016.

[72] Uwe Stilla, Uwe Soergel, and Ulrich Thoennessen. Potential and limits of insar data for building reconstruction in built-up areas. *ISPRS Journal of photogrammetry and remote sensing*, 58(1-2):113–123, 2003.

[73] Paolo Gamba, Fabio Dell'Acqua, and B Houshmand. Comparison and fusion of lidar and insar digital elevation models over urban areas. *International Journal of Remote Sensing*, 24(22):4289–4300, 2003.

[74] Noa BD Bechor and Howard A Zebker. Measuring two-dimensional movements using a single insar pair. *Geophysical research letters*, 33(16), 2006.

[75] Pietro Mastro, Carmine Serio, Guido Masiello, and Antonio Pepe. The multiple aperture sar interferometry (mai) technique for the detection of large ground displacement dynamics: an overview. *Remote Sensing*, 12(7):1189, 2020.

[76] Karl Kraus and Norbert Pfeifer. Determination of terrain models in wooded areas with airborne laser scanner data. *ISPRS Journal of Photogrammetry and remote Sensing*, 53(4):193–203, 1998.

[77] Craig L Glennie, William E Carter, Ramesh L Shrestha, and William E Dietrich. Geodetic imaging with airborne lidar: the earth's surface revealed. *Reports on Progress in Physics*, 76(8):086801, 2013.

[78] Olaf Zielke, Yann Klinger, and J Ramon Arrowsmith. Fault slip and earthquake recurrence along strike-slip faults—contributions of high-resolution geomorphic data. *Tectonophysics*, 638:43–62, 2015.

[79] Larry Sugarbaker, Eric W Constance, Hans Karl Heidemann, Allyson L Jason, Vicki Lucas, David Saghy, and Jason M Stoker. *The 3D Elevation Program initiative: a call for action*. US Geological Survey, 2014.

[80] Unal Okyay, Jennifer Telling, Craig L Glennie, and William E Dietrich. Airborne lidar change detection: An overview of earth sciences applications. *Earth-Science Reviews*, 198:102929, 2019.

[81] Anne Bienert, Louis Georgi, Matthias Kunz, Hans-Gerd Maas, and Goddert

Von Oheimb. Comparison and combination of mobile and terrestrial laser scanning for natural forest inventories. *Forests*, 9(7):395, 2018.

[82] Stephen B DeLong, James J Lienkaemper, Alexandra J Pickering, and Nikita N Avdievitch. Rates and patterns of surface deformation from laser scanning following the south napa earthquake, california. *Geosphere*, 11(6):2015–2030, 2015.

[83] Richard Williams. Dems of difference. *Geomorphological Techniques*, 2(3.2), 2012.

[84] Joseph M Wheaton, James Brasington, Stephen E Darby, and David A Sear. Accounting for uncertainty in dems from repeat topographic surveys: improved sediment budgets. *Earth surface processes and landforms: the journal of the British Geomorphological Research Group*, 35(2):136–156, 2010.

[85] Richard D Keane and Ronald J Adrian. Theory of cross-correlation analysis of piv images. *Applied scientific research*, 49(3):191–215, 1992.

[86] Jerry Westerweel, D Dabiri, and Morteza Gharib. The effect of a discrete window offset on the accuracy of cross-correlation analysis of digital piv recordings. *Experiments in fluids*, 23(1):20–28, 1997.

[87] Arjun Aryal, Benjamin A Brooks, Mark E Reid, Gerald W Bawden, and Geno R Pawlak. Displacement fields from point cloud data: Application of particle imaging velocimetry to landslide geodesy. *Journal of Geophysical Research: Earth Surface*, 117(F1), 2012.

[88] Daisuke Ishimura, Shinji Toda, Sakae Mukoyama, Shin'ichi Homma, Kyoko Yamaguchi, and Naoya Takahashi. 3d surface displacement and surface ruptures associated with the 2014 mw 6.2 nagano earthquake using differential lidar3d surface displacement and surface ruptures. *Bulletin of the Seismological Society of America*, 109(2):780–796, 2019.

[89] Jennifer W Telling, Craig Glennie, Andrew G Fountain, and David C Finnegan. Analyzing glacier surface motion using lidar data. *Remote Sensing*, 9(3):283, 2017.

[90] Paul J Besl and Neil D McKay. Method for registration of 3-d shapes. In *Sensor fusion IV: control paradigms and data structures*, volume 1611, pages 586–606. International Society for Optics and Photonics, 1992.

[91] Daniel Girardeau-Montaut, Michel Roux, Raphaël Marc, and Guillaume Thibault. Change detection on points cloud data acquired with a ground laser scanner. *International Archives of Photogrammetry, Remote Sensing and Spatial Information Sciences*, 36(part 3):W19, 2005.

[92] Paolo Cignoni, Claudio Rocchini, and Roberto Scopigno. Metro: measuring error on simplified surfaces. In *Computer graphics forum*, volume 17, pages 167–174. Wiley Online Library, 1998.

[93] Dimitri Lague, Nicolas Brodu, and Jérôme Leroux. Accurate 3d comparison of complex topography with terrestrial laser scanner: Application to the rangitikei canyon (nz). *ISPRS journal of photogrammetry and remote sensing*, 82:10–26, 2013.

[94] Abdel Aziz Taha and Allan Hanbury. An efficient algorithm for calculating the exact hausdorff distance. *IEEE transactions on pattern analysis and machine intelligence*, 37(11):2153–2163, 2015.

[95] Esther Ezra, Micha Sharir, and Alon Efrat. On the performance of the icp algorithm. *Computational Geometry*, 41(1-2):77–93, 2008.

[96] Gerhard Roth and Martin D Levine. Extracting geometric primitives. *CVGIP: image understanding*, 58(1):1–22, 1993.

[97] Shaobo Xia, Dong Chen, Ruisheng Wang, Jonathan Li, and Xinchang Zhang. Geometric primitives in lidar point clouds: A review. *IEEE Journal of Selected Topics*

in Applied Earth Observations and Remote Sensing, 13:685–707, 2020.

[98] Jason M Stoker, John C Brock, Christopher E Soulard, Kernell G Ries, Larry Sugarbaker, Wesley E Newton, Patricia K Haggerty, Kathy E Lee, and John A Young. *USGS Lidar Science Strategy: Mapping the Technology to the Science*. US Department of the Interior, US Geological Survey, 2015.

[99] Paul Segall and James L Davis. Gps applications for geodynamics and earthquake studies. *Annual Review of Earth and Planetary Sciences*, 25(1):301–336, 1997.

[100] Satrio Muhammad Alif, Irwan Meilano, Endra Gunawan, and Joni Efendi. Evidence of postseismic deformation signal of the 2007 m8. 5 bengkulu earthquake and the 2012 m8. 6 indian ocean earthquake in southern sumatra, indonesia, based on gps data. *Journal of Applied Geodesy*, 10(2):103–108, 2016.

[101] Min-Jeong Jo, Hyung-Sup Jung, and Sang-Ho Yun. Retrieving precise three-dimensional deformation on the 2014 m6. 0 south napa earthquake by joint inversion of multi-sensor sar. *Scientific reports*, 7(1):1–10, 2017.

[102] S. Leprince, S. Barbot, F. Ayoub, and J. Avouac. Automatic and precise orthorectification, coregistration, and subpixel correlation of satellite images, application to ground deformation measurements. *IEEE Transactions on Geoscience and Remote Sensing*, 45(6):1529–1558, 2007. doi: 10.1109/TGRS.2006.888937.

[103] William D Barnhart, Jessica R Murray, S-H Yun, Jerry L Svarc, SV Samsonov, EJ Fielding, Benjamin A Brooks, and Pietro Milillo. Geodetic constraints on the 2014 m 6.0 south napa earthquake. *Seismological Research Letters*, 86(2A):335–343, 2015.

[104] William D Barnhart, Ryan D Gold, Hannah N Shea, Katherine E Peterson,

Richard W Briggs, and David J Harbor. Vertical coseismic offsets derived from high-resolution stereogrammetric dsm differencing: The 2013 baluchistan, pakistan earthquake. *Journal of Geophysical Research: Solid Earth*, 124(6):6039–6055, 2019.

[105] Edwin Nissen, Aravindhan K Krishnan, J Ramón Arrowsmith, and Srikanth Saripalli. Three-dimensional surface displacements and rotations from differencing pre- and post-earthquake lidar point clouds. *Geophysical Research Letters*, 39(16), 2012.

[106] Aravindhan K Krishnan, Edwin Nissen, Srikanth Saripalli, Ramon Arrowsmith, and Alejandro Hinojosa Corona. Change detection using airborne lidar: Applications to earthquakes. In *Experimental Robotics*, pages 733–743. Springer, 2013.

[107] A Diederichs, EK Nissen, LJ Lajoie, RM Langridge, SR Malireddi, KJ Clark, IJ Hamling, and A Tagliasacchi. Unusual kinematics of the papatea fault (2016 kaikōura earthquake) suggest anelastic rupture. *Science advances*, 5(10):eaax5703, 2019.

[108] P Glira, N Pfeifer, C Briese, and C Ressl. Rigorous strip adjustment of airborne laserscanning data based on the ICP algorithm. *ISPRS Annals of Photogrammetry, Remote Sensing & Spatial Information Sciences*, 2, 2015.

[109] Arpan Kusari, Craig L Glennie, Benjamin A Brooks, and Todd L Ericksen. *Precise registration of laser mapping data by planar feature extraction for deformation monitoring*. PhD thesis, University of Houston, 2015.

[110] Martin A Fischler and Robert C Bolles. Random sample consensus: a paradigm for model fitting with applications to image analysis and automated cartography. *Communications of the ACM*, 24(6):381–395, 1981.

[111] Alexander E Morelan, Charles C Trexler, and Michael E Oskin. Surface-rupture and

slip observations on the day of the 24 august 2014 south napa earthquake. *Seismological Research Letters*, 86(4):1119–1127, 2015.

[112] Radu Bogdan Rusu, Zoltan Csaba Marton, Nico Blodow, Mihai Dolha, and Michael Beetz. Towards 3d point cloud based object maps for household environments. *Robotics and Autonomous Systems*, 56(11):927–941, 2008.

[113] Charles R Qi, Li Yi, Hao Su, and Leonidas J Guibas. PointNet++: deep hierarchical feature learning on point sets in a metric space. *arXiv preprint arXiv:1706.02413*, 2017.

[114] Mohammed Yousefhussien, David J Kelbe, Emmett J Ientilucci, and Carl Salvaggio. A multi-scale fully convolutional network for semantic labeling of 3D point clouds. *ISPRS journal of photogrammetry and remote sensing*, 143:191–204, 2018.

[115] Takayuki Shinohara, Haoyi Xiu, and Masashi Matsuoka. FWNet: semantic segmentation for full-waveform lidar data using deep learning. *Sensors*, 20(12):3568, 2020.

[116] Congcong Wen, Xiang Li, Xiaojing Yao, Ling Peng, and Tianhe Chi. Airborne lidar point cloud classification with global-local graph attention convolution neural network. *ISPRS Journal of Photogrammetry and Remote Sensing*, 173:181–194, 2021.

[117] Gene H Golub and Charles F Van Loan. *Matrix computations*, volume 3. JHU press, 2012.

[118] Gareth James, Daniela Witten, Trevor Hastie, and Robert Tibshirani. *An introduction to statistical learning*, volume 112. Springer, 2013.

[119] Thomas M Brocher, Annemarie S Baltay, Jeanne L Hardebeck, Fred F Pollitz, Jessica R Murray, Andrea L Llenos, David P Schwartz, James Luke Blair, Daniel J

Ponti, James J Lienkaemper, Victoria E Langenheim, Timothy E Dawson, Kenneth W Hudnut, David R Shelly, Douglas S Dreger, John Boatwright, Brad T Aagaard, David J Wald, Richard M Allen, William D Barnhart, Keith L Knudsen, Benjamin A Brooks, and Katherine M Scharer. The m w 6.0 24 august 2014 south napa earthquake. *Seismological Research Letters*, 86(2A):309–326, 2015.

[120] Daniel J Ponti, Carla M Rosa, and James Luke Blair. The mw 6.0 south napa earthquake of august 24, 2014—observations of surface faulting and ground deformation, with recommendations for improving post-earthquake field investigations. Technical report, US Geological Survey, 2019.

[121] Karin E Budding, John Boatwright, RV Sharp, and JL Saxton. Compilation and analysis of displacement measurements obtained on the superstition hills fault zone and nearby faults in imperial valley, california, following the earthquakes of november 24, 1987. Technical report, US Geological Survey,, 1989.

[122] Robert V Sharp and John L Saxton. Three-dimensional records of surface displacement on the superstition hills fault zone associated with the earthquakes of 24 november 1987. *Bulletin of the Seismological Society of America*, 79(2):376–389, 1989.

[123] John Boatwright, Karin E Budding, and Robert V Sharp. Inverting measurements of surface slip on the superstition hills fault. *Bulletin of the Seismological society of America*, 79(2):411–423, 1989.

[124] Forrest S McFarland, James J Lienkaemper, and S John Caskey. Data from theodolite measurements of creep rates on san francisco bay region faults, california (version 1.2, march 2019). 2019.

[125] Antonio Pepe and Fabiana Calò. A review of interferometric synthetic aperture

radar (insar) multi-track approaches for the retrieval of earth's surface displacements. *Applied Sciences*, 7(12):1264, 2017.

[126] Andrew Hooper, Howard Zebker, Paul Segall, and Bert Kampes. A new method for measuring deformation on volcanoes and other natural terrains using insar persistent scatterers. *Geophysical research letters*, 31(23), 2004.

[127] Michele Crosetto, Oriol Monserrat, María Cuevas-González, Núria Devanthéry, and Bruno Crippa. Persistent scatterer interferometry: A review. *ISPRS Journal of Photogrammetry and Remote Sensing*, 115:78–89, 2016.

[128] Luca Magri and Andrea Fusiello. Multiple model fitting as a set coverage problem. In *Proceedings of the IEEE conference on computer vision and pattern recognition*, pages 3318–3326, 2016.

[129] Jan Skaloud and Derek Lichti. Rigorous approach to bore-sight self-calibration in airborne laser scanning. *ISPRS journal of photogrammetry and remote sensing*, 61 (1):47–59, 2006.

[130] Xinxiang Zhu, Craig L Glennie, and Benjamin A Brooks. Automated near-field deformation detection from mobile laser scanning for the 2014 Mw 6.0 South Napa earthquake. *Journal of Applied Geodesy*, 16(1):65–79, 2022.

[131] MA Chinnery. The deformation of the ground around surface faults. *Bulletin of the Seismological Society of America*, 51(3):355–372, 1961.

[132] Ruwen Schnabel, Roland Wahl, and Reinhard Klein. Efficient ransac for point-cloud shape detection. In *Computer graphics forum*, volume 26, pages 214–226. Wiley Online Library, 2007.

[133] Howard Butler, Bradley Chambers, Preston Hartzell, and Craig Glennie. Pdal: An

open source library for the processing and analysis of point clouds. *Computers & Geosciences*, 148:104680, 2021.

[134] Craig Glennie. Rigorous 3d error analysis of kinematic scanning lidar systems. *Journal of Applied Geodesy*, 1(3):147–157, 2007. doi: doi:10.1515/jag.2007.017. URL `https://doi.org/10.1515/jag.2007.017`.

[135] Roy Mullen. *Manual of photogrammetry*. Asprs Publications, 2004.

[136] Richard B Langley. Dilution of precision. *GPS world*, 10(5):52–59, 1999.

[137] Rock Santerre, Alain Geiger, and Simon Banville. Geometry of gps dilution of precision: revisited. *GPS Solutions*, 21(4):1747–1763, 2017.

[138] William S Cleveland. Robust locally weighted regression and smoothing scatterplots. *Journal of the American statistical association*, 74(368):829–836, 1979.

[139] U.S. Geological Survey and California Geological Survey. Quaternary fault and fold database for the United States. https://www.usgs.gov/natural-hazards/earthquake-hazards/faults, accessed: 10/15/2021.

[140] Richard K Slocum and Christopher E Parrish. Simulated imagery rendering workflow for UAS-based photogrammetric 3D reconstruction accuracy assessments. *Remote Sensing*, 9(4):396, 2017.

[141] Xinxiang Zhu, Craig L Glennie, Benjamin A Brooks, and Todd L Ericksen. Monitoring aseismic fault creep using persistent urban geodetic markers generated from mobile laser scanning. *ISPRS Open Journal of Photogrammetry and Remote Sensing*, 2:100009, 2021.

[142] Chao Ding, Lu Zhang, Mingsheng Liao, Guangcai Feng, Jie Dong, Meng Ao, and Yanghai Yu. Quantifying the spatio-temporal patterns of dune migration near minqin

oasis in northwestern china with time series of landsat-8 and sentinel-2 observations. *Remote Sensing of Environment*, 236:111498, 2020.

[143] T Heid and A Kääb. Evaluation of existing image matching methods for deriving glacier surface displacements globally from optical satellite imagery. *Remote Sensing of Environment*, 118:339–355, 2012.

[144] Julien Travelletti, Christophe Delacourt, Pascal Allemand, J-P Malet, Jean Schmittbuhl, Renaud Toussaint, and Mickael Bastard. Correlation of multi-temporal ground-based optical images for landslide monitoring: Application, potential and limitations. *ISPRS Journal of Photogrammetry and Remote Sensing*, 70:39–55, 2012.

[145] André Stumpf, Jean-Philippe Malet, and Christophe Delacourt. Correlation of satellite image time-series for the detection and monitoring of slow-moving landslides. *Remote sensing of environment*, 189:40–55, 2017.

[146] Ning Cao, Hyongki Lee, and Hahn Chul Jung. A phase-decomposition-based psinsar processing method. *IEEE Transactions on Geoscience and Remote Sensing*, 54(2): 1074–1090, 2015.

[147] Oumer S Ahmed, Steven E Franklin, Michael A Wulder, and Joanne C White. Characterizing stand-level forest canopy cover and height using Landsat time series, samples of airborne lidar, and the Random Forest algorithm. *ISPRS Journal of Photogrammetry and Remote Sensing*, 101:89–101, 2015.

[148] Douglas K Bolton, Nicholas C Coops, and Michael A Wulder. Characterizing residual structure and forest recovery following high-severity fire in the western boreal of Canada using Landsat time-series and airborne lidar data. *Remote Sensing of Environment*, 163:48–60, 2015.

[149] Katharina Anders, Lukas Winiwarter, Roderik Lindenbergh, Jack G Williams, Sander E Vos, and Bernhard Höfle. 4D objects-by-change: spatiotemporal segmentation of geomorphic surface change from lidar time series. *ISPRS Journal of Photogrammetry and Remote Sensing*, 159:352–363, 2020.

[150] Katharina Anders, Lukas Winiwarter, Hubert Mara, Roderik Lindenbergh, Sander E Vos, and Bernhard Höfle. Fully automatic spatiotemporal segmentation of 3D lidar time series for the extraction of natural surface changes. *ISPRS Journal of Photogrammetry and Remote Sensing*, 173:297–308, 2021.

[151] JC Savage and M Lisowski. Inferred depth of creep on the Hayward fault, central California. *Journal of Geophysical Research: Solid Earth*, 98(B1):787–793, 1993.

[152] James J Lienkaemper, Jon S Galehouse, and Robert W Simpson. Creep response of the hayward fault to stress changes caused by the loma prieta earthquake. *Science*, 276(5321):2014–2016, 1997.

[153] Karl V Steinbrugge, Edwin G Zacher, Don Tocher, CA Whitten, and CN Claire. Creep on the San Andreas fault. *Bulletin of the Seismological Society of America*, 50(3):389–415, 1960.

[154] Lloyd S Cluff and Karl V Steinbrugge. Hayward fault slippage in the Irvington-Niles districts of Fremont, California. *Bulletin of the Seismological Society of America*, 56(2):257–279, 1966.

[155] RO Burford and PW Harsh. Slip on the San Andreas fault in central California from alinement array surveys. *Bulletin of the Seismological Society of America*, 70(4):1233–1261, 1980.

[156] Michael Lisowski and WH Prescott. Short-range distance measurements along the

San Andreas fault system in central California, 1975 to 1979. *Bulletin of the Seismological Society of America*, 71(5):1607–1624, 1981.

[157] Sandra S Schulz, Gerald M Mavko, Robert O Burford, and William D Stuart. Long-term fault creep observations in central California. *Journal of Geophysical Research: Solid Earth*, 87(B8):6977–6982, 1982.

[158] Sandra S Schulz. Catalog of creepmeter measurements in California from 1966 through 1988. Technical report, Dept. of the Interior, US Geological Survey,, 1989.

[159] Surface creep on California faults homepage. http://cires1.colorado.edu/ bilham/creepmeter.file/creepmeters.htm, accessed: 03/18/2022.

[160] Jon S Galehouse. Effect of the Loma Prieta earthquake on surface slip along the Calaveras fault in the Hollister area. *Geophysical Research Letters*, 17(8):1219–1222, 1990.

[161] CR Allen and SW Smith. Pre-earthquake and post-earthquake surficial displacements, 1966.

[162] Robert D Brown and JG Vedder. Surface tectonic fractures along the San Andreas fault, the Parkfield-Cholame California earthquakes of June-August 1966. *US Geol. Surv. Prof. Pap*, 579:2–23, 1967.

[163] William H Bakun and Allan G Lindh. The Parkfield, California, earthquake prediction experiment. *Science*, 229(4714):619–624, 1985.

[164] RW Simpson, JJ Lienkaemper, and JS Galehouse. Variations in creep rate along the Hayward Fault, California, interpreted as changes in depth of creep. *Geophysical Research Letters*, 28(11):2269–2272, 2001.

[165] K Somani Arun, Thomas S Huang, and Steven D Blostein. Least-squares fitting of

two 3-d point sets. *IEEE Transactions on pattern analysis and machine intelligence*, (5):698–700, 1987.

[166] A Piyush Shanker and Howard Zebker. Edgelist phase unwrapping algorithm for time series insar analysis. *JOSA A*, 27(3):605–612, 2010.

[167] Marie-Pierre Doin, S Guillaso, R Jolivet, C Lasserre, F Lodge, Gabriel Ducret, and Raphael Grandin. Presentation of the small baseline nsbas processing chain on a case example: The etna deformation monitoring from 2003 to 2010 using envisat data. In *Proceedings of the Fringe symposium*, pages 3434–3437. ESA SP-697, Frascati, Italy, 2011.

[168] Lukas Winiwarter, Katharina Anders, and Bernhard Höfle. M3c2-ep: Pushing the limits of 3d topographic point cloud change detection by error propagation. *ISPRS Journal of Photogrammetry and Remote Sensing*, 178:240–258, 2021.

Appendix A

Normal equations of the combined least squares adjustment for change detection of a lidar time series

The normal equation is formed as:

$$\begin{bmatrix} A_1^T(BP^{-1}B^T)^{-1}A_1 + H^T P_h H & A_1^T(BP^{-1}B^T)^{-1}A_2 \\ A_2^T(BP^{-1}B^T)^{-1}A_1 & A_2^T(BP^{-1}B^T)^{-1}A_2 + G^T P_g G \end{bmatrix} \begin{bmatrix} \hat{\delta}_1 \\ \hat{\delta}_2 \end{bmatrix} + \begin{bmatrix} A_1^T(BP^{-1}B^T)^{-1}w + H^T P_h w_h \\ A_2^T(BP^{-1}B^T)^{-1}w + G^T P_g w_g \end{bmatrix} = \begin{bmatrix} 0 \\ 0 \end{bmatrix} \tag{A.1}$$

where $A_1 = \frac{\partial f}{\partial \boldsymbol{x}}$ and $A_2 = \frac{\partial f}{\partial \boldsymbol{n}}$ are the partial derivative of function f with respect to the unknown transformation (translation and rotation parameters) and plane parameters (the plane normal), $B = \frac{\partial f}{\partial \boldsymbol{l}}$ is the partial derivative of function f with respect to the observations (laser points), v are the residuals, and w is the misclosure vector, i.e. the value of function f estimated with the estimated parameters and observations. $G = \frac{\partial g}{\partial \boldsymbol{n}}$ and $H = \frac{\partial h}{\partial \boldsymbol{T}}$ are the partial derivative of the constraints g and h with respect to the unknowns, v_g and v_h are the constraint residual vectors and w_g and w_h are the misclosure vectors of the constraints. The weights for the observations and constrains are assumed to be diagonal given as $P = diag(\frac{1}{\sigma_X^2}, \frac{1}{\sigma_Y^2}, \frac{1}{\sigma_Z^2})$, $P_g = diag(\frac{1}{\sigma_{g_1}^2}, \frac{1}{\sigma_{g_2}^2}, ..., \frac{1}{\sigma_{g_j}^2})$, and $P_h = (diag(\frac{t_1}{\sigma_{h_1}})^2, (\frac{t_2}{\sigma_{h_2}})^2, ..., (\frac{t_i}{\sigma_{h_i}})^2)$ with i, j being the indexes of the measurement epoch and primitive. All adjustment matrices, including $A_1, A_2, and B$, have a block diagonal shape where the bi-temporal regression reside in every block.